A flow paradigm in heavy-ion collisions*

Li Yan[1)]

Department of Physics, McGill University, 3600 rue University Montréal, H3A 2T8, QC, Canada

Abstract: The success of hydrodynamics in high energy heavy-ion collisions leads to a flow paradigm, to understand the observed features of harmonic flow in terms of the medium collective expansion with respect to initial state geometrical properties. In this review, we present some essential ingredients in the flow paradigm, including the hydrodynamic modeling, the characterization of initial state geometry and the medium response relations. The extension of the flow paradigm to small colliding systems is also discussed.

Keywords: heavy-ion collisions, hydrodynamics, harmonic flow

PACS: 25.75.-q, 21.65.-f, 24.10.Nz **DOI:** 10.1088/1674-1137/42/4/042001

Contents

1 Introduction

In the theoretical modeling of high energy heavy-ion collisions at the Relativistic Heavy-Ion Collider (RHIC) at the Brookhaven National Laboratory and at the Large Hadron Collider (LHC) at CERN, one essential concept often used is the system collectivity, and especially the collectivity of Quark-Gluon Plasma (QGP) [1, 2] – a hot and dense medium consisting of quarks and gluons.

This concept plays a key role in the understanding of heavy-ion collisions, in several respects. First, the dynamical properties of QGP during its collective evolution contain the information of QCD phase structure. With respect to heavy-ion experiments, it is crucial to have an appropriate description of the QGP evolution in the investigation of the phase transition from quarks and gluons to hadrons, and the searching of the QCD critical point in the beam energy scan program [3]. Second, there is mounting evidence from heavy-ion experiments supporting QGP as a perfect fluid in nature, with very small dissipation. Phenomenological analyses have revealed that in QGP the ratio of shear viscosity to entropy density, η/s, is very close to the lower bound predicted from the theory of gauge-gravity duality for a strongly-coupled system [4],

$$\frac{\eta}{s}=O\left(\frac{\hbar}{4\pi k_B}\right). \tag{1}$$

Received 3 January 2018, Published online 20 March 2018

∗ Supported by Natural Sciences and Engineering Research Council of Canada

1) E-mail: li.yan@physics.mcgill.ca

Since the transport properties of a medium are determined by the underlying microscopic dynamics, estimating the η/s of the QGP system in heavy-ion collisions provides an unambiguous probe of the dynamical properties of QCD. Third, QGP collective evolution is responsible for all the observed patterns in the spectrum of soft particles (particles of small transverse momentum, mass, etc.). These soft particles amount to over 99% of the total particle yields in heavy-ion experiments. Additionally, the collective evolution of the QGP also determines the background for hard probes (particles with large transverse momentum, mass, etc.), including the jet-quenching phenomenon [5] and heavy quarkonia dissociation and regeneration [6]. It is also the background for electromagnetic signatures in heavy-ion collisions, such as direct photon production [7, 8], and those related to the chiral magnetic effect [9].

The concept of medium collectivity has been investigated extensively in heavy-ion experiments, in which an unprecedented level of precision in the experimental observables has been achieved. Different types of measurables from the correlations of of soft particles have been devised and explored, in nucleus-nucleus collisions at RHIC and the LHC energies. These include, especially, the so-called harmonic flow. Recently, measurements of particle correlations have been generalized to smaller colliding systems, such as proton-lead, deuteron-gold, and even proton-proton collision events with extremely high multiplicity production. Surprisingly, the observed particle correlation patterns in the small colliding systems are compatible with the picture of medium collective expansion. Regarding all the remarkable experimental progress, theoretical frameworks have been proposed on various grounds. Especially, the success of hydrodynamic modeling has allowed a flow paradigm to emerge. The purpose of this review is to show how the flow paradigm is established based on theoretical calculations via hydrodynamic modelings of heavy-ion collisions, and the corresponding analyses of the experimental results.

The flow paradigm for heavy-ion collisions is inspired by the very idea of the system collective expansion. It assumes the dominant evolution stages of the created system in nucleus-nucleus collisions or in small colliding systems, as a collectively expanding QGP medium or hadron gas, which is close to local thermal equilibrium. As a result, the dynamics of the medium evolution is dominated by long wave-length hydrodynamic modes. In this way, the created partons or hadrons in each collision event evolve coherently as a fluid medium, in response to the system's geometrical structures at earlier times, so that their dynamical behaviors affect the observed correlations of soft particles in experiments.

Accordingly, the flow paradigm commonly employs viscous hydrodynamics for the description of medium evolution. However, note that the flow paradigm does not prevent the use of a kinetic approach with respect to individual partons or hadrons, as long as sytem collective evolution in the kinetic description is well-established. Viscous hydrodynamics is an effective theory for systems close to local thermal equilibrium, where the dominant degrees of freedom are long-wavelength hydrodynamic variables. In the theoretical framework of hydrodynamics, the dissipative effect in a fluid system is described in terms of a gradient expansion order-by-order. Each term in the gradient expansion is specified by a transport coefficient. The first order terms correspond to the shear and the bulk viscosity. Application of viscous hydrodynamics to a system crucially depends on a separation between the microscopic scale and the macroscopic scale which controls the convergence of the gradient expansion. In the present analyses, a truncation at second order viscous corrections is generally applied throughout all the collective evolution stages in heavy-ion collisions. Solving viscous hydrodynamics requires initial conditions. With respect to the hydro modeling of heavy-ion collisions, an effective characterization of the initial stage with fluctuations is employed, accounting for the fact that nucleus-nucleus collisions fluctuate from event to event. After the system collective expansion stages in heavy-ion collisions, the observables should be calculable as hadrons emitted independently towards detectors.

Theoretical calculations always depend on parameters. For instance, in hydrodynamic modeling, effective descriptions of initial state, transport properties, etc, must be specified for different colliding systems. For the purpose of extracting the medium transport properties, these parameterizations bring in substantial uncertainties in analyses. Therefore, it is important in the flow paradigm to capture some common features of the observables in experiments, such as those in correlations and fluctuations of harmonic flow, so as to minimize the uncertainties from effective parameterizations. These common features of flow observables can be understood empirically following some quantitative relations,

which are summarized based on hydrodynamic simulations with respect to all existing observables in heavy-ion experiments. These relations between harmonic flow and the geometrical properties of initial state are expected to be model independent, but contain essential information about the initial state geometry, event-by-event fluctuations, and the medium dissipations.

These are several types of average considered in this review. Unless specified, we shall use double brackets $\langle\langle\ldots\rangle\rangle$ to notate the average of a quantity over events. In each single event, the average over a density profile in the transverse plane is denoted by curly brackets, $\{\ldots\}$. Considering the approximation of Bjorken boost invariance

of the system generated in heavy-ion collisions, the Milne space-time coordinates are often introduced in a theoretical framework, in which the proper time $\tau=\sqrt{t^2-z^2}$ and space-time rapidity $\xi=\tanh^{-1}(z/t)$ are used instead of t and z.

This review is organized as follows. Theoretical ingredients in the flow paradigm are described in Section 2, including a brief description of viscous hydrodynamic modeling of heavy-ion collisions in Section 2.1. Section 2.2 presents discussions on initial state geometrical properties captured in terms of initial eccentricities. Empirically, results from hydro modeling of heavy-ion collisions lead to the medium response relations between harmonic flow and initial state eccentricities, which are introduced in Section 2.3. In Section 3, after an overview of the flow observables compatible with the flow paradigm, we present quantitative characterizations of flow observables based on the medium response relations. Especially, the observed flow fluctuations and correlations are analyzed in Section 3 and Section 3.2, respectively. Section 4 focuses on recent measurements involving flow observables in small colliding systems, and the corresponding theoretical developments that generalize the flow paradigm in small systems. A summary of the review is given in Section 5.

2 Ingredients of the flow paradigm

To understand the observed flow observables in heavy-ion collisions, in the flow paradigm a hydrodynamic model is applied which solves the hydrodynamic equations of motion for the medium collective expansion. The information of the initial state, especially the geometry of the colliding systems, is incorporated accordingly in the initial condition of the coupled equations. In this way, the observed fluctuations and correlations of flow harmonics are recognized as a consequence of the combined effects from the geometrical properties of initial state and transport properties of the medium. In the flow paradigm, the geometry of initial state is decomposed and characterized by a set of eccentricities $\mathcal{E}_n$, while medium dynamical properties are contained in the proposed medium response relations. In this section, we present these three essential ingredients in the flow paradigm: hydrodynamic modeling, characterization of initial state geometry, and medium response relations.

2.1 Hydrodynamic modeling

In a hydrodynamic simulation of the system evolution in heavy-ion collisions, there are three stages: initialization of the fluid, solving the hydrodynamic equations of motion, and particle generation.

The hydrodynamic equations of motion are nothing but a set of conservation laws, in which dissipative properties of the medium are introduced and captured by transport coefficients, such as shear viscosity η and bulk viscosity ζ. These transport coefficients are solely determined by the underlying dynamics of the system, *i.e.*, QCD in heavy-ion collisions, so they should be treated as inputs. However, the complexity of the medium system in heavy-ion collisions makes it difficult for a first-principles calculation of the transport coefficients. For instance, it is expected that the coupling constant varies from weakly-coupled to strongly-coupled as the QGP cools down. As a result, in practical simulations, η/s is often considered as some parameterized form, with or without temperature dependence (cf. the calculations in Ref. [10]). In a similar manner, in practical hydro simulations there are also effective parameterizations for the characterization of initial state of the colliding system, the equation of state, and the freeze-out prescription. Compared to experimentally measured observables, the primary goal of hydro simulations then becomes to constrain these parameterizations, which contain information about initial state geometrical fluctuations [11], medium dissipative properties, and the equation of state of QCD [12, 13].

The conservation of energy and momentum is written in hydrodynamics as

$$\partial_\mu T^{\mu\nu}=0, \tag{2}$$

where the energy-momentum tensor $T^{\mu\nu}$ is defined in terms of hydrodynamic variables: energy density e, pressure $\mathcal{P}$ and flow four-velocity u^μ,

$$T^{\mu\nu}=eu^\mu u^\nu+\mathcal{P}\Delta^{\mu\nu}+\Pi^{\mu\nu}. \tag{3}$$

The operator $\Delta^{\mu\nu}=u^\mu u^\nu+g^{\mu\nu}$ is a projection operator, which with the flow four-velocity u^μ can be used to put the formulation of hydrodynamics in a covariant form. Namely, one may write the spatial gradient and temporal derivative covariantly as $\Delta_{\mu\nu}\partial^\nu=\nabla_\mu$ and $D=u^\mu\partial_\mu$, respectively. Note that in Eq. (3), we have taken the mostly plus matrix convention, $g^{\mu\nu}=(-,+,+,+)$, which leads to the flow velocity normalization as $u^2=-1$. When an equation of state is introduced and coupled to the hydrodynamic equation of motion, these hydro variables are completely determined. In practical simulations with respect to heavy-ion collisions, an equation of state from lattice QCD calculations is generally incorporated [14].

Dissipative corrections to the energy-momentum tensor are reflected in the stress tensor $\Pi^{\mu\nu}$. The scale separation between a microscopic scale related to system mean free path $l_{\rm mfp}$, and a macroscopic scale associated with the system size L, allows one to expand viscous hydrodynamics in a series of gradients. The ratio of these two scales is recognized as a small quantity, the Knudsen number ${\rm Kn}\sim l_{\rm mfp}/L$. To the first order in the gradient expansion (the first order viscous correction), the stress

tensor has the well-known Navier-Stokes form,

$$\Pi^{\mu\nu}=-\eta\sigma^{\mu\nu}-\zeta\Delta^{\mu\nu}\nabla\cdot u=\pi^{\mu\nu}+\Delta^{\mu\nu}\Pi, \tag{4}$$

where $\pi^{\mu\nu}$ and Π are the viscous corrections associated with the shear and the bulk channel. The structure of the first order in the gradient expansion

$$\sigma^{\mu\nu}=\nabla^{\mu}u^{\nu}+\nabla^{\nu}u^{\mu}-\frac{2}{3}\Delta^{\mu\nu}\nabla\cdot u\equiv\nabla^{\langle\mu}u^{\nu\rangle} \tag{5}$$

is a symmetric and traceless tensor, and it is transverse to u^{ν}, $\sigma^{\mu\nu}u_{\mu}=0$. Note that in Eq. (5), and in the following discussion of this section, the single brackets around indices of a tensor denote that the tensor has been made symmetric, traceless and transverse to u^{μ}. In practical hydrodynamic simulations, to avoid acausal mode evolution, second order viscous corrections must be taken into account in the gradient expansion (cf. discussions in Ref. [15]).

There are more terms which stem from more involved gradient structures in higher order viscous corrections, and accordingly more transport coefficients. In a simplified case at the second order, considering a form of relaxing second order terms to their Navier-Stokes correspondence in Eq. (4), one finds the relativistic generalization of the Israel-Stewart hydrodynamics, with new transport coefficients τ_{π} and τ_{Π} associated with the relaxation time of the shear channel and bulk channel, respectively. For instance, the shear channel has

$$(\tau_{\pi}D+1)\pi^{\mu\nu}=-\eta\sigma^{\mu\nu}+\ldots, \tag{6}$$

where the ellipsis implies structures generated from the second order of gradient expansion, e.g., $\sigma^{\langle\mu}_{\ \alpha}\sigma^{\alpha\nu\rangle}$, $\sigma^{\mu\nu}\nabla u$, and $\sigma^{\langle\mu}_{\ \alpha}\Omega^{\alpha\nu\rangle}$ ($\Omega^{\mu\nu}=\frac{1}{2}(\nabla^{\mu}u^{\nu}-\nabla^{\nu}u^{\mu})$ being an anti-symmetric tensor). Variants of definitions of the second order viscous hydrodynamics have been achieved in a conformal fluid [16], and from the moment expansion techniques [17].

Eq. (6) is the most commonly solved hydro equation of motion for hydro modeling of heavy-ion collisions at RHIC and the LHC [18–22]. However, it is *not* a complete theoretical formulation, because thermal fluctuations are ignored. Thermal fluctuations in a fluid system, also known as the hydrodynamic fluctuations, are present in all the evolution stages of the expanding medium in heavy-ion collisions. The strength of hydrodynamic fluctuations is related to dissipative properties of the fluid through the fluctuation-dissipation relations [23]. In the theoretical framework, hydrodynamic fluctuations can be introduced as an extra stochastic tensor $S^{\mu\nu}$ to the energy-momentum tensor [24–26],

$$T^{\mu\nu}=eu^{\mu}u^{\nu}+\mathcal{P}\Delta^{\mu\nu}+\Pi^{\mu\nu}+S^{\mu\nu}, \tag{7}$$

whose two-point auto-correlation is related to the corresponding dissipations. For the Navier-Stokes hydrodynamics [27][1)],

$$\langle\langle S^{\mu\nu}(x)S^{\alpha\beta}(x')\rangle\rangle=2T\Big[\eta(\Delta^{\mu\alpha}\Delta^{\nu\beta}+\Delta^{\mu\beta}\Delta^{\nu\alpha})+\left(\zeta-\frac{2}{3}\eta\right)\Delta^{\mu\nu}\Delta^{\alpha\beta}\Big]\delta^{(4)}(x-x'), \tag{8}$$

with the strength of the thermal fluctuations determined by the shear and bulk viscosity. The Dirac delta function in Eq. (8) is practically recognized in realistic simulations of a finite thermal system as the inverse of space-time volume. Therefore, one naively expects significant contributions from thermal fluctuations in small colliding systems, and systems close to the QCD critical point. In practical simulations, solving the noisy viscous hydrodynamics is more challenging than most of the present hydro modelings.

To solve the hydrodynamic equations of motion, one needs inputs from an effective characterization of the system at the initial stages of heavy-ion collisions. That is to say, all hydro variables, as well as the stress tensor $\pi^{\mu\nu}$, and bulk pressure Π, must be specified at some proper time τ_0, assuming at which the QGP system is sufficiently close to local thermal equilibrium. Approaching local thermalization, or in a more relaxed term, the onset of viscous hydrodynamics, is a crucial challenge to the application of viscous hydrodynamics in heavy-ion collisions, despite all the success of hydro modelling has achieved regarding flow observables. In particular, in recent experiments with small colliding systems, the validity of viscous hydrodynamics needs to be re-examined. The onset of hydrodynamics, although it is a topic beyond the scope of the present review, shall be briefly addressed in the context of applying hydrodynamics and the flow paradigm in small colliding systems in Section 4.2.1. One may find more detailed discussions elsewhere in Ref. [28] and Ref. [29]. A value of $\tau_0\sim O(1)$ fm/c has been found necessary to make reasonable predictions in nucleus-nucleus collisions at RHIC and the LHC energies. For smaller colliding systems, some hydro simulations suggest $\tau_0\sim O(0.1)$ fm/c [30].

In hydrodynamic modeling, several effective models have been developed to generate a density profile of the QGP system at τ_0 [31–35], with fluctuations implemented through Monte Carlo simulations. Inspired by a color-glass picture, in models such as IP-Glasma [31], an initial state energy density profile is obtained by solving the gluon field evolution. On the other hand, in the MC-Glauber model [32], energy is deposited from nucleon-nucleon collisions in an eikonal approximation. All of these models provide an event-by-event basis for

1) The two-point auto-correlation of thermal fluctuations is defined according to the average over thermal ensembles, for which in this review we use the same notation of double brackets $\langle\langle\ldots\rangle\rangle$, despite its subtle difference from average over events in heavy-ion collisions.

hydrodynamic simulations, and especially, a fluctuating initial state. Fig. 1 presents the distribution of energy density $e(x,y)$ in the transverse plane of one typical event in heavy-ion collisions at initial time τ_0, generated from the MC-Glauber, MC-KLN and IP-Glasma models. Bumpy structures seen in these distributions reflect fluctuations originating from energy deposition during nucleus-nucleus collisions. As one can see, the fluctuations are stronger in the IP-Glasma model than in MC-Glauber. Simply speaking, one may recognize gradients of the distribution, due to an overall shape or fluctuations, as the driving force of system expansion in hydrodynamics. Accordingly, the fluctuating geometry of the initial state is converted into asymmetries of the generated particles in the momentum space. This is the intuitive interpretation of medium response to initial state geometry, which we shall detail in the next subsection.

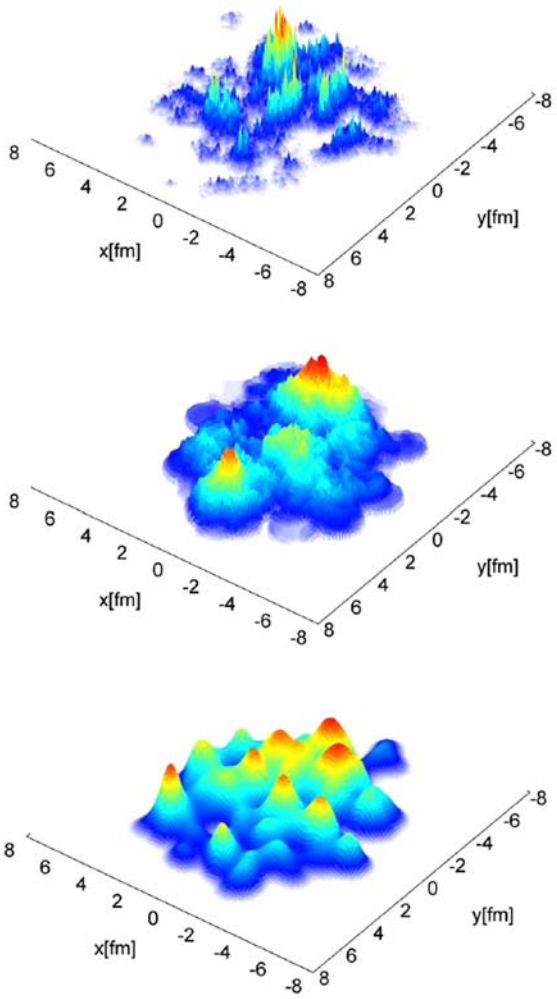

Fig. 1. (color online) Initial state distribution of energy density in the transverse plane from IP-Glasma (top), MC-KLN (middle) and MC-Glauber (bottom) models. Reprinted figure with permission from B. Schenke, P. Tribedy, and R. Venugopalan, Phys. Rev. Lett. 108, 252301, 2012 (DOI: https://doi.org/10.1103/PhysRevLett.108.252301) (Ref. [31]). Copyright 2012 by the American Physical Society.

The medium system created in heavy-ion collisions cools down as it expands. Once the system becomes so locally dilute that the dominant degrees of freedom are excited particles instead of hydro variables, the system starts to freeze out from the fluid description. A common procedure of freeze-out was given by Cooper and Frye [36], in which hadrons are generated from a fluid on a 3D hyper-surface Σ determined by the freeze-out condition,

$$E\frac{\mathrm{d}N}{\mathrm{d}^3\boldsymbol{p}}=\int_\Sigma \mathrm{d}\sigma\cdot p f(u^\mu,T,\mu). \tag{9}$$

The phase-space distribution function $f(u^\mu,T,\mu)$ should be incorporated properly corresponding to viscous hydrodynamics through Landau's matching condition. More precisely, it is

$$f(u^\mu,T,\mu)=n(u^\mu,T,\mu)+\delta f(u^\mu,T,\mu), \tag{10}$$

with the local equilibrium distribution $n(u^\mu,T,\mu)$ corresponding to ideal hydrodynamics and the viscous correction

$$\int\frac{\mathrm{d}^3\boldsymbol{p}}{E}p^\mu p^\nu\delta f(u^\mu,T,\mu)=\Pi^{\mu\nu}. \tag{11}$$

For the shear channel, it is conventionally taken as $\delta f(u^\mu,T,\mu)\propto p^\mu p^\nu\pi_{\mu\nu}$ [37] while the bulk channel has $\delta f(u^\mu,T,\mu)\propto\Pi$ [38, 39]. The canonical form of the viscous correction to the phase-space distribution at second order has more involved dependence in the second order gradients and momentum, but converges to the first order viscous corrections with respect to small dissipations [40]. The chemical potential μ in Eq. (9) is specified with respect to the desired particle species.

For more realistic hydro simulations of heavy-ion collisions, the particle spectrum receives further modifications from subsequent interactions among hadrons, including hadrons collisions in kinetics and resonance decays, which can be described by effective models, such as UrQMD [41].

Eventually, the spectrum of particles from each collision event is determined from numerical simulations, accounting for all the effects mentioned above. The single-particle spectrum represents the hydro prediction of the particles observed in detectors in experiments. It should be emphasized that hydrodynamic predictions of the particle spectrum are characteristic in long-range correlations in rapidity, which are best quantified by the harmonic flow, V_n. Defined according to a Fourier decom-

position of the emitted single-particle spectrum,

$$E\frac{\mathrm{d}N}{\mathrm{d}^3\boldsymbol{p}}=\frac{1}{2\pi}\frac{\mathrm{d}N}{p_{\mathrm{T}}\mathrm{d}p_{\mathrm{T}}\mathrm{d}\eta}\left[1+\sum_{n=1}^{\infty}\left(V_n(p_{\mathrm{T}},\eta)\mathrm{e}^{-\mathrm{i}n\phi_p}+\mathrm{c.c.}\right)\right], \tag{12}$$

the harmonic flow V_n characterizes the momentum anisotropy in azimuth of the particle spectrum, of order n. In Eq. (12), $\eta=\tanh^{-1}(p_z/|\mathbf{p}|)$ is the pseudo-rapidity, which should be distinguished from the notation of shear viscosity. In Eq. (12), *c.c.* indicates a complex conjugate. Harmonic flow V_n's are complex by definition,

$$V_n(p_{\mathrm{T}},\eta)\equiv v_n\mathrm{e}^{\mathrm{i}n\Psi_n}=\langle\mathrm{e}^{\mathrm{i}n\phi_p}\rangle \tag{13}$$

where the magnitude v_n characterizes the magnitude of azimuthal anisotropies of the particle spectrum in the transverse directions, while the phase Ψ_n, also known as the event-plane, determines orientation of the anisotropy. In the last equation of Eq. (13), the single brackets denote an average with respect to the single particle spectrum in one collision event.

Fluctuations in the initial state density profile from event to event result in fluctuations of the generated paricle spectrum, and also flucutating harmonic flow V_n. Therefore, in event-by-event hydrodynamic simulations, as in experiments, harmonic flow V_n should be extracted via multi-particle correlations. In experiments, it has been noticed that anisotropy of the particle spectrum depends on collision centrality, transverse momentum p_{T}, and rapidity y (implying the dependence on particle species), or pseudo-rapidity η, as does the corresponding harmonic flow V_n.

Different orders of the harmonic flow have specified physical interpretations, in terms of the azimuthal symmetry. The most dominant flow signature is $n=2$, the elliptic flow V_2, which characterizes the asymmetric distribution of particles generated in- and out-of the event-plane Ψ_2 in one collision event [42]. For the case of $n=1$, which characterizes asymmetric particle yields from one side of the system to the other, there is a rapidity-even component which is often referred to as the dipolar flow [43, 44], and a rapidity-odd piece. In multi-particle correlations, although both the dipolar flow and the rapidity-odd V_1 receive contributions from momentum conservation in multi-particle correlations [45], the dipolar flow is generated as a result of medium collective expansion, as in the flow paradigm. The rapidity-odd V_1 is rooted in the properties of nucleus scatterings, and has a strong correlation with the reaction plane. Regarding higher order azimuthal anisotropies, there are also trianglar flow V_3 [46], quadranglar flow V_4, etc. It should emphasized that the flow harmonics of order n has a determined rotational symmetry in the azimuth, $\phi_p\to\phi_p+2\pi/n$.

In experiments, it has been found that the elliptic flow is more significant than others. Especially in nucleus-nucleus collisions, such as the Au+Au at RHIC, the signature of ellitptic flow is understood as a medium evolution with respect to an almond-shaped geometry determined by the initial overlap of the colliding system. Relating flow observables to initial state geometry is generalizable to higher order flow harmonics, which motivates the analyses of medium response relations in the flow paradigm.

Although hydrodynamic modeling of heavy-ion collisions gives rise to results with quantitative agreement with the observed flow signatures, these calculations rely on several effective parameterizations. Especially, the effective description of the initial state contributes to the greatest extent to the uncertainties of the analyses. These are the dominant source of uncertainties in the extraction of η/s in hydro modeling. In addition, there are also fundamental issues related to the application of dissipative fluid dynamics to heavy-ion collisions, which are more severe for the recent experiments carried out with small colliding systems. Nevertheless, the success of hydro modeling in heavy-ion collisions allows one to empirically correlate the observed flow signatures to the geometrical properties of the initial state and the dissipative feature of the expanding medium, as in the flow paradigm. By doing so, what really matter in analysis are the common features of the observed flow harmonics in various colliding systems, in a way that not only can one understand the generation of harmonic flow, flow correlation and fluctuation, but also provides quantitative constraints on the exatraction of η/s, with minimized dependence on the effective parameterizations of the model.

2.2 Geometrical properties of the initial state

The quantitative relations established in the flow paradigm to relate the observed flow harmonics to initial state and medium dissipations requires appropriate characterizations of the initial state geometry. This can be achieved by using the so-called initial state eccentricity $\mathcal{E}_n$, which by definition is introduced according to the azimuthal symmetry of the initial state density profile. Fluctuations of the initial state density profile lead to fluctuations of $\mathcal{E}_n$ from event to event. Additionally, on an event-by-event basis, $\mathcal{E}_n$ are correlated owing to the background geometry resulting from the colliding systems. Fluctuations and correlations of $\mathcal{E}_n$ are crucial in understanding the similar behaviors in V_n.

2.2.1 Initial state anisotropy $\mathcal{E}_n$

The idea to relate harmonic flow and initial state geometry is inspired by the fact that the linearised hydrodynamic response does not mix the evolution of modes, once these modes are considered small perturbations. In terms of the expanding medium systems in heavy-ion col-

lisions, these are modes associated with azimuthal asymmetries which are responsible for the generation of flow harmonics (cf. Ref. [47]). Also, as in the original observation of elliptic flow, V_2 [42], in a somewhat crude analysis ignoring fluctuations in the initial state, people realized that the observed elliptic flow is correlated to an almond shape of the initial state density profile.

In high energy heavy-ion collisions, such an almond-shaped distribution is simply expected from the overlap of two colliding nuclei when collisions are non-central, with the shorter dimension of the almond shape aligned with the reaction plane. As a result, elliptic flow can be interpreted as a result of medium expansion driven by the asymmetric density profile. More precisely, gradients, which play the role of force in hydrodynamics, are anisotropic in- and out-of reaction plane, leading correspondingly to an anisotropic expansion. This expansion scenario has been justified by the similar expansion out of an anisotropic medium system realized in the cold atom experiments [48]. The key in this relation is the azimuthal structure of the initial distribution, which is asymmetric between in- and out-of reaction plane, analogous to that of elliptic flow. The extent of asymmetry is characterized by a dimensionless quantity called ellipticity. With respect to the reaction-plane, it can be defined as

$$\varepsilon_2^{RP}=\frac{\{x^2-y^2\}}{\{x^2+y^2\}}, \tag{14}$$

where the curly brackets denote the average with respect to the initial state energy (or entropy) density distribution,

$$\{...\}=\frac{\int \mathrm{d}x\mathrm{d}y e(x,y)...}{\int \mathrm{d}x\mathrm{d}y e(x,y)}. \tag{15}$$

The reaction-plane ellipticity ε_2^{RP} is bounded by unity. It is clear that the elliptic asymmetry vanishes when $\varepsilon_2^{RP}=0$, corresponding to a density profile with absolute azimuthal symmetry. Elliptic asymmetry maximizes when $\varepsilon_2^{RP}=1$. To a good approximation, a linear relation between the ellipticity and v_2 has been found [49].

When event-by-event fluctuations are taken into account, the initial state geometry in heavy-ion collisions depends not only on the background shape, but also deformations induced by the extra fluctuations. A generalization of ellipticity to higher orders can be applied, which provides a mode decomposition with respect to the azimuthal asymmetry of the initial state geometry. If one takes the complex expression $z=x+iy=r\mathrm{e}^{\mathrm{i}\phi}$ for the transverse coordinates, a standard generalization of the n-th order eccentricity is defined in terms of the n-th order moment of the density, as

$$\mathcal{E}_n\equiv\varepsilon_n\mathrm{e}^{\mathrm{i}n\Phi_n}=-\frac{\{z^n\}}{\{|z|^n\}}=-\frac{\{r^n\mathrm{e}^{\mathrm{i}n\phi}\}}{\{r^n\}}, \qquad n>1, \tag{16}$$

where $\{|z|^n\}$ in the denominator plays the role of normalization. The minus sign is conventionally taken so that $\mathcal{E}_n$ is potentially aligned with respect to V_n, although the alignment is often broken due to the complexity induced from the medium response. It can also be understood as a Fourier decomposition of the energy density in terms of azimuthal angle ϕ, with a r^n-weight corresponding to the fluctuation modes along the radial direction. For the case of $n=1$, since $\{z\}$ vanishes by a re-centering of the density profile[1)], the non-trivial leading contribution is

$$\mathcal{E}_1\equiv\varepsilon_1\mathrm{e}^{\mathrm{i}\Phi_1}=-\frac{\{z^2z^*\}}{\{|z|^3\}}=-\frac{\{r^3\mathrm{e}^{\mathrm{i}\phi}\}}{\{r^3\}}, \tag{17}$$

which captures a dipolar structure in the initial energy density. $\mathcal{E}_1$ is the dipolar anisotropy, which is rapidity-even. Note that in Eq. (16), $\mathcal{E}_n$ is complex with its module ε_n characterizing the magnitude of asymmetry, while its phase Φ_n defines the orientation. The phase Φ_n is sometimes referred to as the participant plane of the initial state. Both ε_n and Φ_n fluctuate from event to event in heavy-ion collisions as the density profile fluctuates. Again, by definition in Eq. (16) and Eq. (17), $\mathcal{E}_n$ is bounded by unity, with a vanishing $\mathcal{E}_n$ indicating a vanishing n-th order anisotropy, while a maximized anisotropy is achieved when $|\mathcal{E}_n|=\varepsilon_n=1$.

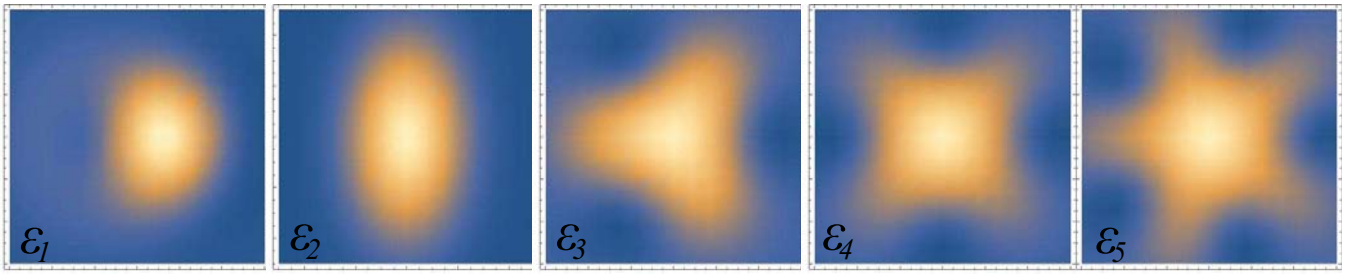

Fig. 2. (color online) Characteristic shapes of the deformed initial state density profile, corresponding to anisotropies of $\mathcal{E}_1$, $\mathcal{E}_2$, $\mathcal{E}_3$, $\mathcal{E}_4$ and $\mathcal{E}_5$ (from left to right).

1) Re-centering of the initial density in a theoretical analysis is always allowed, since the physical observables in heavy-ion collisions are invariant under translations in the transverse plane.

By construction, $\mathcal{E}_n$ is invariant under rotation in azimuthal angle, $\phi \to \phi+2\pi/n$, which implies that the azimuthal angle dependence of the fluctuating density profile is decomposed into modes according to $\mathcal{E}_n$. Each mode corresponds to a characteristic shape, under the rotational symmetry. In addition to the elliptic shape associated with $\mathcal{E}_2$, $\mathcal{E}_3$ defines the triangularity, $\mathcal{E}_4$ defines the quadrangularity, etc. Fig. 2 demonstrates the eccentric shapes corresponding to $n=1$ to $n=5$. The phase Φ_n's in Fig. 2 are aligned with the x-axis.

Mode decomposition of the azimuthal angle dependence in Eq. (16) gives rise to correct definitions of dimensionless quantities, with the desired symmetry dependence with respect to rotation. However, the definition of initial eccentricity is *not* unique. Apparently, various types of weight function of the radial distance $f(r)$ can be applied, accounting for the dependence in the radial direction [46, 50, 51], so that one has in general

$$\mathcal{E}_n[f(r)]=-\frac{\{f(r)\mathrm{e}^{\mathrm{i}n\phi}\}}{\{|f(r)|\}}. \tag{18}$$

For instance, instead of the r^2 weighting in the definition of $\mathcal{E}_2$, r^4-weighted moments, $\{r^4\mathrm{e}^{\mathrm{i}2\phi}\}=\{z^3z^*\}$, also lead to the characterization ellipticity, satisfying the same symmetry condition under rotation. A systematic way of considering the r-dependence of the initial state requires a generalized mode decomposition in r. Analogous to the fact that different harmonic orders relate to different structures in the azimuth of the system, higher modes associated with r in the definition of eccentricities correspond to different (and finer) structures in the radial direction. These higher modes are particularly important regarding fluctuations of the initial state density profile. With respect to the same harmonic order, these different modes along r contribute simultaneously to the corresponding harmonic flow, but they have different dynamical properties responsible for the observed momentum dependence, which motivates the proposed principal component analysis [52, 53].

In addition to the moment of the density profile, one may also consider using cumulants [43]. For instance, for the 4-th order anisotropy, cumulants of the density profile gives

$$\mathcal{E}_4^c=-\frac{1}{\{|z|^4\}}[\{z^4\}-3\{z^2\}^2], \tag{19}$$

where terms proportional to $\{z\}$ are suppressed as a result of re-centering correction. Like $\mathcal{E}_4$, one may check that $\mathcal{E}_4^c$ is also invariant under the rotation $\phi\to\phi+2\pi/4$. However, unlike $\mathcal{E}_4$, $\mathcal{E}_4^c$ is *not* bounded by unity, in particular in very peripheral collisions where the ellipticity of the system is large. A cumulant definition of the eccentricity coincides with the moment definition, when $n\leqslant 3$. When $n\geqslant 4$, there are always subtractions or additions of nonlinear moment couplings in the cumulant definition. For the cumulant definition of the fifth order and the sixth order, one has

$$\begin{aligned}\mathcal{E}_5^c&=-\frac{\{z^5\}-10\{z^2\}\{z^3\}}{\{|z|^5\}},\\ \mathcal{E}_6^c&=-\frac{\{z^6\}-15\{z^4\}\{z^2\}-10\{z^3\}^2+30\{z^2\}^3}{\{|z|^6\}}\end{aligned} \tag{20}$$

Throughout discussions in this review, we shall take the momentum-based definition by default.

2.2.2 Fluctuations and correlations of $\mathcal{E}_n$

In the flow paradigm, fluctuations and correlations of $\mathcal{E}_n$ play an essential role in the understanding of fluctuations and correlations of the harmonic flow V_n. For the discussion of fluctuations, we shall focus on lower harmonic orders ($n\leqslant 3$), to avoid complexities due to the nonlinear mode couplings during the medium evolution. Correlations amongst $\mathcal{E}_n$ will be addressed with respect to the correlations of participant plane Φ_n. In this subsection, we concentrate on some of the analytical results from independent sources, with respect to very fundamental assumptions. Deviations from the present assumptions are expected to be sub-leading.

Fluctuations and correlations of initial state eccentricities are rooted in the event-by-event fluctuations of initial state density profile, and accordingly the induced fluctuating initial state geometry. Although it can be realized through Monte Carlo simulations of effective models, the fluctuating density profiles of various effective models behave differently, which gives rise to different evaluations of the induced anisotropies, the probability distributions of anisotropies and correlations among them. As is clearly shown in Fig. 1, the density profile from IP-Glasma is more spiky, implying stronger fluctuations of anisotropy. Despite ambiguities in different effective models, there are two essential concepts one has to take into account in a theoretical analysis of the initial state geometry: background geometry and fluctuations. The background geometry of a fluctuating system reflects the event-averaged density profile. For instance, in collisions such as Au+Au at RHIC, and Pb+Pb at the LHC energies, the event-averaged density presents a determined almond shape in each centrality class. Given a background density profile which captures the correct shape, fluctuations are treated as extra sources.

Fluctuations of $\mathcal{E}_n$ In the simplest scenario, one considers a fluctuating density profile in terms of N-independent point-like sources, distributed according to a two-dimensional Gaussian background geometry. It has been found that with respect to such a configuration, the probability distribution of initial state eccentricity can be solved analytically [54, 55], leading to the so-called elliptic-power distribution. The two-dimensional

elliptic-power distribution for ellipticity $\mathcal{E}_n=\varepsilon_x+i\varepsilon_y$ is

$$P(\varepsilon_x,\varepsilon_y)=\frac{\alpha}{\pi}(1-\varepsilon_0^2)^{1+\frac{1}{2}}\frac{(1-\varepsilon_x^2-\varepsilon_y^2)^{\alpha-1}}{(1-\varepsilon_0\varepsilon_x)^{2\alpha+1}}, \tag{21}$$

where ε_0 and α are parameters associated with the background shape and number of independent sources, respectively. Regarding the Gaussian background, ε_0 characterizes ellipticity in the reaction plane. Note, however, that although ε_0 is expected to be close to ε_2^{RP}, it should be distinguished from the real ellipticity in the reaction plane defined for a fluctuating system, owing to the effects of fluctuations. The parameter $\alpha=\frac{N-1}{2}$ is related to the fluctuation strength, which is roughly proportional to $1/\sqrt{N}$. One remarkable property of the elliptic-power distribution is its consistency with the condition that eccentricity is bounded by unity. This is implied in the normalization

$$\int \mathrm{d}\varepsilon_x \mathrm{d}\varepsilon_y P(\varepsilon_x,\varepsilon_y)=1, \tag{22}$$

where integration runs over a unit disk, $|\mathcal{E}_n|\leqslant 1$. The upper bound of the eccentricity is not generally satisfied in other distribution functions. For instance, considering a simplification of the elliptic-power distribution in the limit $\alpha\gg 1$, corresponding to a system with small fluctuations, the distribution Eq. (21) reduces to a two-dimensional elliptic Gaussian,

$$P(\varepsilon_x,\varepsilon_y)=\frac{1}{2\pi\sigma_x\sigma_y}\exp\left(-\frac{(\varepsilon_x-\varepsilon_0)^2}{2\sigma_x^2}-\frac{\varepsilon_y^2}{2\sigma_y^2}\right), \tag{23}$$

which is normalized in the entire plane of $(\varepsilon_x,\varepsilon_y)$.

In deriving the elliptic-power distribution, ε_0 is introduced to characterize the intrinsic anisotropy induced from the background geometry. There are circumstances when $\varepsilon_0=0$, so that the initial state eccentricity is entirely generated by fluctuations. For instance, in proton+Pb collisions, the created medium is rotationally symmetric if the shape of the proton is isotropic. Also, as in collisions like Pb+Pb, all odd-order anisotropies vanish from the background geometry. In such cases, the elliptic-power reduces to the power distribution,

$$P(\varepsilon_x,\varepsilon_y)=\frac{\alpha}{\pi}(1-\varepsilon_x^2-\varepsilon_y^2)^{\alpha-1}. \tag{24}$$

One may check that the power distribution is also normalized on a unit disk.

The probability distribution of the magnitude can be found by integrating out the dependence of angle $\varphi_n=\arg(\mathcal{E}_n)$. The elliptic-power distribution gives,

$$\begin{aligned}P(\varepsilon_n) =\ & 2\varepsilon_n\alpha(1-\varepsilon_n^2)^{\alpha-1}(1-\varepsilon_n\varepsilon_0)^{-1-2\alpha}(1-\varepsilon_0^2)^{\alpha+\frac{1}{2}}\\ & \times{}_2F_1\left(\frac{1}{2},1+2\alpha;1;\frac{2\varepsilon_n\varepsilon_0}{\varepsilon_n\varepsilon_0-1}\right),\end{aligned} \tag{25}$$

where ${}_2F_1$ is the hypergeometric function. The power distribution gives,

$$P(\varepsilon_n)=2\alpha\varepsilon_n(1-\varepsilon_n^2)^{\alpha-1}. \tag{26}$$

Figure 3 displays the probability ditribution of ε_2, ε_3 and ε_4, generated from MC-Glauber simulations, with respect to Pb+Pb collision events in the 75%-80% centrality class at the LHC energy $\sqrt{s_{\rm NN}}=2.76$ TeV. This very peripheral centrality class is purposely chosen since the effects of fluctuations are sufficiently strong, so is the influence from the bound of ε_n by unity.

The fit using an elliptic-power distribution describes ε_2 and ε_4 (red solid lines in Fig. 3 (a) and (c)) well, while since ε_3 in Pb+Pb collisions is solely fluctuation-driven, its fluctuating feature is compatible with a power distribution, as shown in Fig. 3 (b). When $\sigma_x=\sigma_y$ in the two-dimensional elliptic Gaussian Eq. (23), integration over angle φ is applicable, which leads to the Bessel-Gaussion function [56],

$$P(\varepsilon_n)=\frac{\varepsilon_n}{\sigma^2}\exp\left(-\frac{\varepsilon_n^2+\varepsilon_0^2}{2\sigma^2}\right)I_0\left(\frac{\varepsilon_0\varepsilon_n}{\sigma^2}\right) \tag{27}$$

As a comparison, the fit using the Bessel-Gaussian function is shown in Fig. 3 as the green dashed lines. The Bessel-Gaussian results in a worse description of the eccentricity distribution. Especially, one notices the non-zero tails of the Bessel-Gaussian at $\varepsilon_n=1$ in Fig. 3, as anticipated, since in the Bessel-Gaussian distribution the upper bound of eccentricities is infinity.

As a simple summary, we notice that the probability distributions of initial state eccentricities are apparently non-Gaussian, as one sees in Fig. 3 that the elliptic-power and power distributions give rise to much better fits than the Bessel-Gaussian function. Considering the derivation of elliptic-power and power distribution functions, assuming only N-independent point-like sources on top of a Gaussian background, the non-Gaussianity comes dominantly from the fact that $\mathcal{E}_n$ is bounded by unity.

Elliptic-power and power distributions have been successfully applied to parameterize a general class of the generated initial state eccentricity from effective models, where differences of these effective models are quantitatively captured by the parameters ε_0 and α [55]. Note that in these models, there are many other sources that contribute to the non-Gaussianity of the initial eccentricity fluctuations. For instance, there are higher order corrections concerning a more sophisticated configuration of the initial state density profile rather than a two-dimensional Gaussian, and extra correlations among sources, etc. [57–59], which have been taken into account in theoretical analyses.

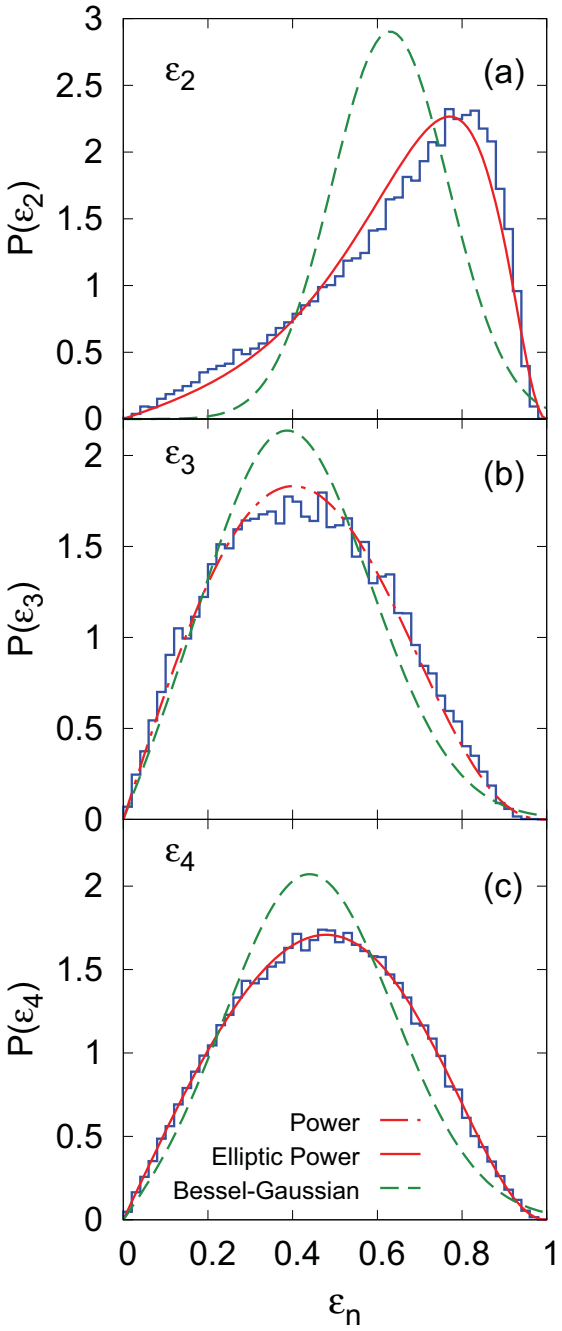

Fig. 3. (color online) Histogram of the initial state eccentricity (a) ε_2, (b) ε_3 and (c) ε_4 distributions, obtained from Monte-Carlo simulations of the MC-Glauber model, with respect to the Pb+Pb collisions in the 75%–80% centrality class, at $\sqrt{s_{\rm NN}} = 2.76$ TeV. Lines of different styles and color are fit using elliptic-power (red solid), power (red dash-dot) and Bessel-Gaussian (green dashed) functions. Reprinted figure with permission from L. Yan, J.-Y. Ollitrault, and A. M. Poskanzer, Phys. Rev. C 90, 024903, 2014 (DOI: https://doi.org/10.1103/PhysRevC.90.024903) (Ref. [55]). Copyright 2014 by the American Physical Society.

Correlations of $\mathcal{E}_n$ Event-by-event fluctuations of the density profile also generate correlations among initial state eccentricities [43, 60]. These correlations are consequences of pure geometrical effects due to the averaged background geometry and fluctuations of energy deposition from event to event [61]. The similar idea of treating the density profile as independent sources can be applied to the mixed correlations among $\mathcal{E}_n$ [62]. In this way, one may consider introducing the event-by-event fluctuation of a function g as $\delta_g \equiv \{g\} - \langle\langle g\rangle\rangle$. Note that $\{g\}$ is obtained with respect to the density profile of one single event, while $\langle\langle g\rangle\rangle$ is the averaged value over events. From the independent sources, one has the two-point correlation of fluctuations inversely proportional to the number of independent sources [63],

$$\langle\langle \delta_f \delta_g \rangle\rangle = \frac{\langle\langle fg\rangle\rangle - \langle\langle f\rangle\rangle\langle\langle g\rangle\rangle}{N}. \tag{28}$$

Three-point and four-point correlations are found at the next leading-order, in terms of $1/N^2$. Therefore, by taking account of the recentering corrections, fluctuating initial eccentricities $\mathcal{E}_2$ and $\mathcal{E}_3$ are written as

$$\begin{aligned}
\mathcal{E}_2 &= -\frac{\{(z-\delta_z)^2\}}{\{r^2\}} \approx -\frac{\langle\langle z^2\rangle\rangle + \mathcal{E}_0 \delta_{r^2} + \delta_{z^2}}{\langle\langle r^2\rangle\rangle} + O(\delta^2) \\
\mathcal{E}_3 &= -\frac{\{(z-\delta_z)^3\}}{\{r^3\}} \approx -\frac{\delta_{z^3} - 3\langle\langle z^2\rangle\rangle \delta_z}{\langle\langle r^3\rangle\rangle} + O(\delta^2)
\end{aligned} \tag{29}$$

Note that we have assumed a non-zero averaged background ellipticity, $\mathcal{E}_0 = -\langle\langle z^2\rangle\rangle / \langle\langle r^2\rangle\rangle$ in the above equations, which corresponds to the case of non-central nucleus-nucleus collisions. As a result, Eq. (29) implies the fact that $\varepsilon_2\{2\} \sim \varepsilon_0$, while $\varepsilon_3\{2\} \sim 1/\sqrt{N}$. One should be aware that in colliding systems such as He^3+Au, the ultra-central collisions are expected to have an averaged triangular shape, so that a non-zero background triangularity should be assumed instead, $\mathcal{E}_0 = -\langle\langle z^3\rangle\rangle / \langle\langle r^3\rangle\rangle$.

Eq. (29) can be generalized to other eccentricities, which allows one to analytically derive the mixed correlations among $\mathcal{E}_n$, order by order with respect to $1/N$. For instance, at the leading-order, the correlation between $\mathcal{E}_2$ and $\mathcal{E}_3$ has the following contribution,

$$\langle\langle \mathcal{E}_2^3 \mathcal{E}_3^{*2} \rangle\rangle = -\frac{9|\mathcal{E}_0|^6}{N} \frac{\langle\langle r^2\rangle\rangle^3}{\langle\langle r^3\rangle\rangle^2}. \tag{30}$$

Although the above estimate is only valid with respect to independent sources, it generically captures the feature of negative correlation. Besides, one also expects from Eq. (30) that the strength of correlation grows when N decreases, corresponding to an increase of centrality percentile in heavy-ion collisions. Both of these features are confirmed in model simulations, as shown in Fig. 4. Fig. 4 displays the mixed correlators involving $\mathcal{E}_1$, $\mathcal{E}_2$ and $\mathcal{E}_3$, from Monte-Carlo simulations of a CGC-typed model

and the Glauber model. Analytic solutions from independent sources are obtained in terms of the expansion in inverse to the number of sources. One notices that the correlations are well-described by analytical results from independent sources. The correlations of initial state eccentricities are observed quite generally in various effective models, which inspire the measurement of the mixed correlations in harmonic flow [64].

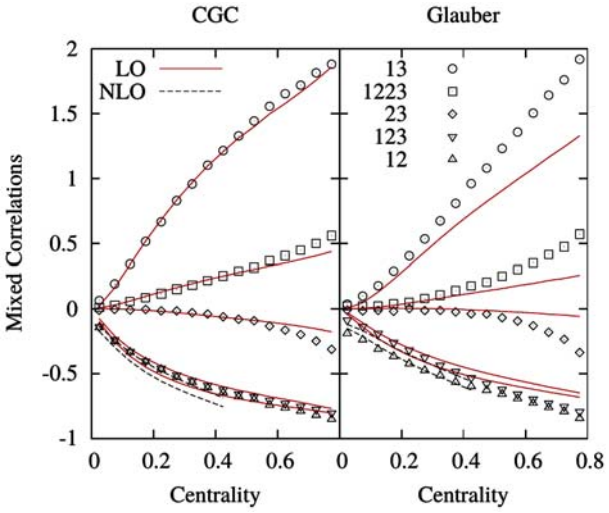

Fig. 4. (color online) Mixed correlations among initial state eccentricities $\mathcal{E}_n$. Red solid and black dashed lines are estimates from independent sources, to the leading-order in $1/N$ and next leading-order, respectively. Symbols are Monte-Carlo simulations from the CGC model (left panel) and the Glauber model (right panel). The notations indicate to the mixed correlations of the corresponding harmonic orders, with a proper normalization of the magnitude of eccentricities. Reprinted figure with permission from R. S. Bhalerao, M. Luzum, and J.-Y. Ollitrault, Phys. Rev. C 84, 054901, 2011 (DOI: https://doi.org/10.1103/PhysRevC.84.054901) (Ref. [62]). Copyright 2011 by the American Physical Society.

2.3 Medium response to $\mathcal{E}_n$

Solutions to the hydrodynamic equations of motion are completely determined once an initial condition is specified. With respect to the fluctuating initial state characterized in terms of initial state eccentricities, the hydrodynamic predictions of harmonic flow are expected as a function of these eccentricities,

$$V_n = V_n(\mathcal{E}, \alpha). \tag{31}$$

In Eq. (31), $\mathcal{E}$ denotes a set of initial state eccentricities that are responsible to V_n, while α contains parameters related to the medium dynamical properties, such as the transport coefficient η/s. Although the explicit form of Eq. (31) is not known *a priori* from first-principle calculations, there is mounting evidence from numerical hydrodynamic simulations suggesting that one may expand $V_n(\mathcal{E},\alpha)$ in terms of $\mathcal{E}$,

$$V_n = \kappa(\alpha)\mathcal{E} + O(\mathcal{E}^2) + \delta_n, \tag{32}$$

with respect to the fact that $|\mathcal{E}| < 1$. The quantity δ_n is the residual introduced accounting for deviations due to additional fluctuations. By assumption, δ_n is uncorrelated with initial state eccentricities, which we shall address later. Note that δ_n is complex, since Eq. (32) relates complex quantities on both sides of the equation. More precisely, the magnitudes and the phases of both sides in the equation are identical respectively.

In practice one would like to truncate the expansion at a finite order, so that harmonic flow can be well approximated. These terms in the expansion correspond to the medium response to the initial geometry $\mathcal{E}$, from the linear order, to nonlinear mixing of higher orders. Comments are in order with respect to the expansion Eq. (32).

1. The expansion relies on the fact that $\mathcal{E}_n$'s are small quantities. In collisions of large systems such as Pb+Pb and Au+Au, this criterion is generally satisfied for harmonic orders $n \neq 2$, because initial state eccentricities of order $n \neq 2$ are generated entirely from fluctuations. One estimates the magnitude of eccentricity $\varepsilon_n \sim 1/\sqrt{N} \ll 1$. Whereas when $n = 2$, ellipticity comes dominantly from the background geometry in non-central collisions. Therefore, $\mathcal{E}_2$ is more significant than other eccentricities in the expansion. Effective model simulations have shown that towards peripheral collisions, ε_2 can grow above 0.5, which implies the role of nonlinear order terms involving $\mathcal{E}_2$ in the expansion.

2. By expanding in $\mathcal{E}_n$'s, the dependence on medium dynamical properties is absorbed separately in the expansion coefficients, $\kappa(\alpha)$, etc. We shall refer to the coefficient of the linear order $\kappa(\alpha)$ as the linear response coefficient. Coefficients of higher orders as nonlinear response coefficients. These coefficients are remarkable in probing the medium dynamical properties, as their dependence on the initial state is minimized. Although Eq. (32) is written on an event-by-event basis, one would expect the medium response coefficients not to fluctuate in one centrality class. These coefficients are calculable in hydrodynamic simulations, and as will be discussed, some of them are accessible in experiments under fairly general assumptions.

3. In each single event, with respect to the rotational symmetry of V_n, each term on the right-

hand side of Eq. (32) is invariant under the rotation $\phi\to\phi+2\pi/n$. Since response coefficients are real quantities according to parity conditions, at each order the allowed combinations of $\mathcal{E}_n$'s can be determined by symmetry conditions. For the response of linear order, it is apparent that V_n^L (the linear part of flow V_n) is proportional to $\mathcal{E}_n$. It should be emphasized that there exist ambiguities in the definition of $\mathcal{E}_n$. Symmetry constraints on the nonlinear order part of the flow V_n^{NL} are more useful. For instance, for the fourth order flow harmonics, in addition to a linear response to $\mathcal{E}_4$, the nonlinear contributions at quadratic order include the coupling of $\mathcal{E}_2$, i.e., $V_4^{NL}\propto\mathcal{E}_2^2$. For V_5, rotational symmetry requires the nonlinear part to be generated by quadratic coupling between $\mathcal{E}_2$ and $\mathcal{E}_3$, $V_5^{NL}\propto\mathcal{E}_2\mathcal{E}_3$.

With respect to all these aspects, the following forms have been found successful in practical applications of the expansion Eq. (32). From the elliptic flow V_2 to harmonic order n=6 [20, 65],

$$V_2=\kappa_2\mathcal{E}_2+\kappa_2'\varepsilon_2^2\mathcal{E}_2+\delta_2, \tag{33a}$$
$$V_3=\kappa_3\mathcal{E}_3+\kappa_{23}'\varepsilon_2^2\mathcal{E}_3+\delta_3, \tag{33b}$$
$$V_4=\kappa_4\mathcal{E}_4+\kappa_{422}\mathcal{E}_2^2+\delta_4, \tag{33c}$$
$$V_5=\kappa_5\mathcal{E}_5+\kappa_{523}\mathcal{E}_2\mathcal{E}_3+\delta_5, \tag{33d}$$
$$V_6=\kappa_6\mathcal{E}_6+\kappa_{633}\mathcal{E}_3^2+\kappa_{624}\mathcal{E}_2\mathcal{E}_4+\kappa_{6222}\mathcal{E}_2^3+\delta_6. \tag{33e}$$

One notices that higher order flow becomes more complicated since more terms from the nonlinear mode mixings are required to achieve a good approximation. There have also been some attempts in the similar analysis for the flow V_7 and V_8,

$$\begin{aligned} V_7 &= \kappa_7\mathcal{E}_7+\kappa_{7223}\mathcal{E}_2^2\mathcal{E}_3+\ldots+\delta_7 \\ V_8 &= \kappa_8\mathcal{E}_8+\kappa_{82222}\mathcal{E}_2^4+\ldots+\delta_8, \end{aligned} \tag{34}$$

where even more involved terms up to the quartic order nonlinear couplings contribute. Although Eqs. (33) are kind of idealistic, in the sense that they require explicit information of the $\mathcal{E}_n$'s, these relations are of great significance in the flow paradigm. These response relations can be applied to quantitatively describe the final state flow observables in terms of the dynamical properties of the medium, and the initial state eccentricities $\mathcal{E}_n$. In the following subsections, we shall summarize some important details in Eqs. (33) based on solutions of viscous hydrodynamics.

2.3.1 Viscous effects on the medium response

The effect of fluid response to the initial state perturbations is suppressed by viscous corrections in hydrodynamics. When the solution of the system evolution is decomposed into modes, it is further expected that the higher order modes get stronger viscous corrections.

In theory, the argument that the response of higher order mode is more damped by viscous corrections can be verified in several cases with analytic solutions of viscous hydrodynamics. In the linear response analysis with respect to a static fluid background, considering any types of initial perturbations of hydrodynamic fields which are decomposed into modes k (wave-number), it is known that the evolution of these modes undergoes viscous corrections proportional to $-k^2\eta/s$, as a result of the diffusion feature of the Navier-Stokes equations (cf. Ref. [66]).

Similar behaviors of the fluid dynamics are also present in the analytic solutions of expanding systems: the 0+1 dimensional Bjorken flow [68] and 1+1 dimensional Gubser flow [47]. Gubser flow is an analytical solution of a conformal fluid system, with system expansion realized both in the longitudinal direction along spacetime rapidity, and in the radial direction along r. The analytical solution of the Gubser flow assumes a background which is rotationally symmetric. Deformation of the symmetric background results in mode decomposition in terms of spherical harmonics $\mathcal{E}_n^{(l)}\sim Y_n^l$. The index l captures the fluctuations along the radial direction, while n is associated with the azimuthal angle. It should be noted that the mode decomposition in terms of n is consistent with the Fourier decomposition used in the usual definition of initial state eccentricities. Corresponding to the initial state geometrical fluctuations in heavy-ion collisions, one may approximate the mode $\mathcal{E}_n^{(l)}$ in the Gubser flow, as the ordinarily defined eccentricity $\mathcal{E}_n$ from moment $\{r^l\mathrm{e}^{\mathrm{i}n\phi}\}$. For instance, in the Gubser flow the mode $\mathcal{E}_2^{(2)}$ can be recognized as the ellipticity $\mathcal{E}_2$. For each n-th order initial eccentricity, the dominant one in the decomposition comes from the lowest order l, satisfying n=l, which is suppressed in the Navier-Stokes hydrodynamics according to the factor

$$\exp(-l^2\eta/s)\sim\exp(-n^2\eta/s). \tag{35}$$

Eq. (35) also reflects the diffusion feature of the mode evolution in hydrodynamics, in analogous to the k^2 suppression in a static fluid.

In realistic systems in heavy-ion collisions, which are not conformal, nor rotationally symmetric, there is no analytical relation solved between harmonic order n and viscous corrections. However, as inspired in these analytic solutions, especially Eq. (35), one still expects a n^2-scaling of the viscous corrections [47, 69, 70]. Indeed, numerical solutions in the single-shot viscous hydrodynamics have found very similar trends in the linear response to the moment (and cumulant) based initial eccentricities, as viscosity increases [71]. Owing to the complexity in exacting linear response coefficients, however, the n^2-scaling has not been validated in event-by-event hydrodynamic simulations.

The n^2 dependence of the viscous suppression in the

fluids has strong indications in the flow paradigm. In particular, in addition to the simple fact that the linear response of higher order flow harmonics is more suppressed than the lower order ones, nonlinear response coefficients are always less suppressed than the corresponding linear response, for the same harmonic order[1)]. As a consequence, in higher order harmonic flow, with $n \geqslant 4$, the dominant contributions are from the nonlinear mode mixings from $\mathcal{E}_2$ and $\mathcal{E}_3$, etc., in the expansion equation Eq. (33), when viscous effects are sufficiently strong.

2.3.2 Medium response in V_2 and V_3

Linear order response We start with the two lower order flow harmonics, elliptic flow V_2 and triangular flow V_3. These two types of flow harmonics are different from the higher order ones in the flow paradigm, as they are dominated by a linear medium response. Nonlinear mode mixings appearing in Eq. (33a) and Eq. (33b) are of cubic order, whose effects are minor expect in some particular situations. Ignoring nonlinear terms, the linear relations

$$V_2 = \kappa_2 \mathcal{E}_2, \qquad V_3 = \kappa_3 \mathcal{E}_3, \tag{36}$$

simplify the theoretical analysis significantly. From Eq. (36), one expects the magnitudes of V_2 and V_3 to be linearly proportional to those of $\mathcal{E}_2$ and $\mathcal{E}_3$, respectively. Besides, the initial state participant planes Φ_2 and Φ_3 are aligned respectively to the event-plane Ψ_2 and Ψ_3, which are determined from the observed particle spectrum. As a result, fluctuations and correlations seen in flow harmonics are to a large extent understandable in terms of those in $\mathcal{E}_2$ and $\mathcal{E}_3$. For instance, the probability distribution of v_2 is then a rescaled distribution of ε_2. In turn, features of the cumulants of initial ε_2 are detectable once the v_2 cumulants are measured in experiments.

The linear relation can be examined simply in hydrodynamic simulations [67, 73]. Scatter plots in Fig. 5, for example, present the linear relation between the magnitude v_2 and magnitude ε_2, and between v_3 and ε_3, based on simulations of viscous hydrodynamics with respect to Au+Au collision events of $\sqrt{s_{\rm NN}} = 200$ MeV, in the centrality class 20%-30% [67]. The linearity is obvious in the figures, with the slope corresponding to the linear response coefficient κ. However, it should be emphasized that the slope is *not* identical to the linear response coefficient κ. One notices a larger slope in the scatter plot of v_2 than v_3 in the same centrality class, signifying a stronger medium linear response to the ellipticity than triangularity. A stronger correlation between v_2 and ε_2 is observed, as the dispersion in the scatter plot of triangularity is more pronounced.

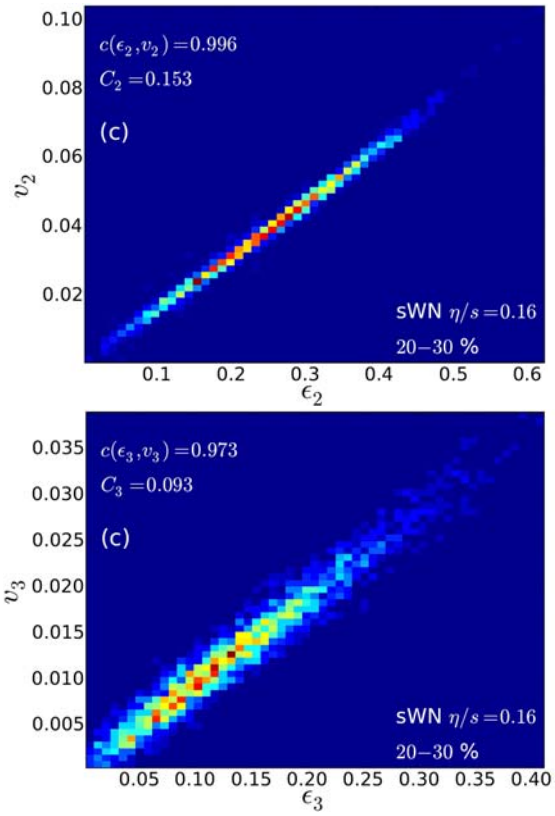

Fig. 5. (color online) Response of the flow magnitudes v_2 and v_3 to the magnitudes of initial ellipticity ε_2 and triangularity ε_3, obtained from event-by-event hydro simulations of the Au+Au collisions in one centrality class, $20\% - 30\%$.. Reprinted figure with permission from H. Niemi et al, Phys. Rev. C 87, 054901, 2013 (DOI: https://doi.org/10.1103/PhysRevC.87.054901) (Ref. [67]). Copyright 2013 by the American Physical Society.

To validate the linear response relations in a more quantitative way, one defines the Pearson correlation coefficient [62]. For V_2, it is written as

$$\mathcal{P}_2 = \frac{{\rm Re}\langle\langle V_2 \mathcal{E}_2^* \rangle\rangle}{\sqrt{\langle\langle v_2^2 \rangle\rangle}\sqrt{\langle\langle \varepsilon_2^2 \rangle\rangle}}, \tag{37}$$

in terms of event-averaged quantities. The Pearson coefficient $\mathcal{P}_2$ measures the linear correlation between V_2 and $\mathcal{E}_2$. It should be emphasized that $\mathcal{P}_2$ measures the linear relation simultaneously between both magnitudes and phases. By construction, $\mathcal{P}_2$ vanishes when V_2 is uncorrelated with $\mathcal{E}_2$, while $\mathcal{P}_2 = \pm 1$ indicates an absolute correlation or anti-correlation. Similarly, for V_3 one has

$$\mathcal{P}_3 = \frac{{\rm Re}\langle\langle V_3 \mathcal{E}_3^* \rangle\rangle}{\sqrt{\langle\langle v_3^2 \rangle\rangle}\sqrt{\langle\langle \varepsilon_3^2 \rangle\rangle}}, \tag{38}$$

1) This statement is true when the viscous correction of harmonic order n is proportional to n^α, as long as $\alpha > 1$, i.e., not necessarily $\alpha = 2$.

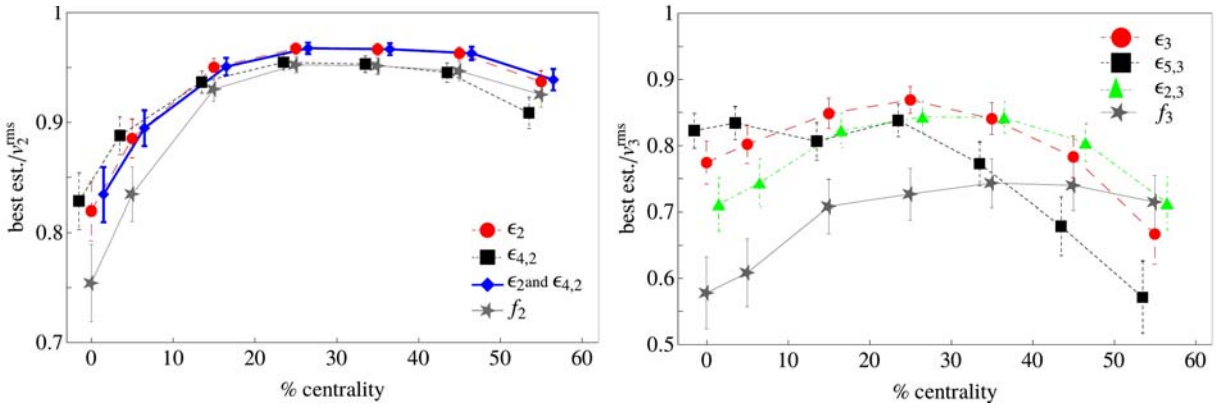

Fig. 6. (color online) Correlations of the elliptic flow v_2 (left panel) and triangular flow v_3 (right panel) for different definitions of initial eccentricities, characterized in terms of Pearson correlation coefficients as a function of centrality percentile. Reprinted figures with permission from F. G. Gardim et al, Phys. Rev. C 85, 024908, 2012 (DOI: https://doi.org/10.1103/PhysRevC.85.024908) (Ref. [72]). Copyright 2012 by the American Physical Society.

which measures the linear correlation between V_3 and $\mathcal{E}_3$. It is worth mentioning that the linear response coefficient κ can be calculated analogously via these event-averaged quantities, i.e.,

$$\kappa_2 = \frac{\mathrm{Re}\langle\langle V_2\mathcal{E}_2^*\rangle\rangle}{\langle\langle\varepsilon_2^2\rangle\rangle}, \qquad \kappa_3 = \frac{\mathrm{Re}\langle\langle V_3\mathcal{E}_3^*\rangle\rangle}{\langle\langle\varepsilon_3^2\rangle\rangle}, \tag{39}$$

The linear response coefficients deviate from the slope of the scatter plot in Fig. 5, which is given as $\langle\langle v_n\varepsilon_n\rangle\rangle/\langle\langle|\varepsilon_n|^2\rangle\rangle$.

In Fig. 6, the Pearson correlation coefficients are calculated in viscous hydrodynamics, with various types of characterizations of the initial state ellipticity (left panel) and triangularity (right panel) examined. On a general ground, the ellipticity defined in Eq. (16) with a r^2 weight (blue points) is most responsible in the linear relation to V_2, leading to $\mathcal{P}_2$ above 0.95 for most of the centrality bins. The correlation gets stronger towards non-central collisions, as one observes an increasing trend of $\mathcal{P}_2$. Ellipticity defined with a r^4 weighting can be found in the cumulant expansion of the initial density profile, whose linear correlation with V_2 is also found to be strong in Fig. 6 (black points). Actually the r^4-weighted ellipticity is more responsible for V_2 in central collisions, which signifies the role of outer layer in the density profile in the generation of elliptic flow in central collisions. The quantity f_2 in Fig. 6 is adopted from the mode decomposition with respect to the Gubser flow [47], whose correlations with V_2 are weaker in all centrality classes.

Similar analyses for the triangular flow are shown in the right-hand panel of Fig. 6. The correlation of the linear relation is generally weaker in V_3 than V_2, consistent with the observation in Fig. 5. The linear correlation with the triangularity defined in Eq. (16) with a r^3 weighting is reasonably good, though a r^2 weighting is more favorable in peripheral bins, which implies the significance of inner layer in the generation of V_3 in systems of smaller sizes. But in larger systems, the outer layer is more sensitive, as one notices the stronger linear correlation with the r^5-weighted definition. The r^5-weighted triangularity is again derived from the cumulant expansion of initial state density profile. Similarly, in the mode decomposition developed from the Gubser flow, f_3 provides weaker correlations to V_3.

Viscous effects on the linear medium response are expected to suppress the response coefficient κ, as has been discussed in the previous section. Besides, event-by-event hydro simulations have also shown that viscosity tends to enhance the linear correlation between initial state eccentricity and flow [67].

Cubic order response The increasing trend of the Pearson correlation coefficients $\mathcal{P}_2$ and $\mathcal{P}_3$ seen in Fig. 6 from central to non-central bins can be understood as owing to the growth of ellipticity and triangularity, against residual fluctuations, etc. When going towards very peripheral collisions, however, one notices a weak but clear drop of the correlation with respect to linearity, indicating the role of nonlinear terms in Eq. (33a) and Eq. (33b).

Deviation from the linear relation in the peripheral collision bins for V_2 is visible in hydrodynamic simulations [10]. Shown in Fig. 7(a) is a scatter plot of the correlation between the magnitudes v_2 and ε_2, obtained in the centrality class 45%-50% of Pb+Pb collisions at $\sqrt{s_{\rm NN}} = 2.76$ TeV [21]. Each point in the plot corresponds to an event with a randomly specified initial geometry from the Monte Carlo Glauber model. A nonlinear trend in the plot is obvious for the events with large values of ε_2. In the same centrality class, deviation from the linear correlation between the magnitude v_3 and the magnitude ε_3 is seen to be negligible in Fig. 7(b). Black dashed lines correspond to the linear response relation, with the slope calculated according to Eqs. (39). Red

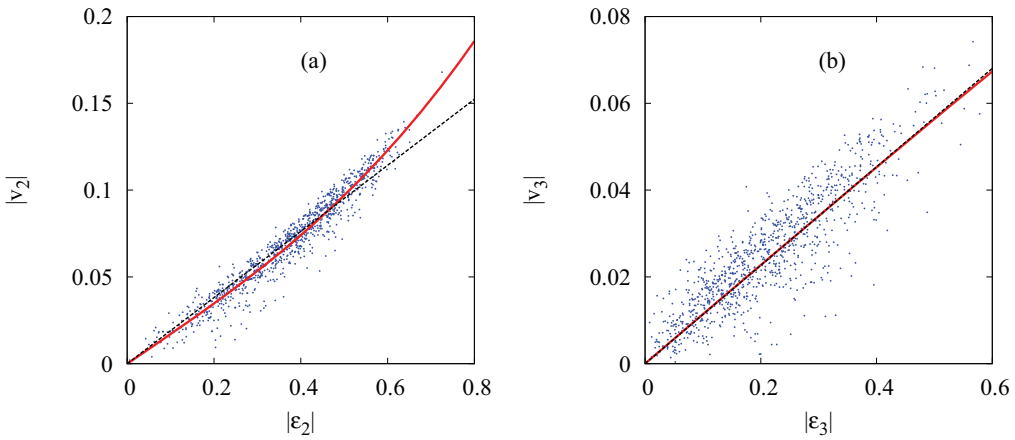

Fig. 7. (color online) Correlation between the magnitudes of anisotropic flow v_n and initial eccentricity ε_n for Pb+Pb collisions at 2.76 TeV in the 45%–50% centrality range. Each point corresponds to a different initial geometry. Dotted line: linear estimator. Full line: cubic estimator. (a) Elliptic flow. (b) Triangular flow. Reprinted figure with permission from J. Noronha-Hostler et al, Phys. Rev. C 93, 014909, 2016 (DOI: https://doi.org/10.1103/PhysRevC.93.014909) (Ref. [21]). Copyright 2016 by the American Physical Society.

solid lines are results containing a cubic order response, with the response coefficients determined as in Eq. (40) and Eq. (41) below.

To include nonlinear effects in the response function, for V_2 and V_3 the allowed terms by symmetry are of cubic order. Following the rule that $\mathcal{E}_2$ is dominant in the expansion, one arrives at the terms $\propto\varepsilon_2^2\mathcal{E}_2$ for V_2 and $\propto\varepsilon_2^2\mathcal{E}_3$ for V_3, respectively. There are new response coefficients corresponding to the cubic order terms. Determination of the linear response coefficient κ and the cubic order response coefficient κ' can be approached by minimizing the effects of residual fluctuations $\langle\langle|\delta_n|^2\rangle\rangle$. Or equivalently, it is the maximization of the Pearson correlation coefficient with respect to the flow constructed with the cubic order response terms. For the elliptic flow V_2, it leads to

$$\kappa_2=\frac{\mathrm{Re}(\langle\langle\varepsilon_2^6\rangle\rangle\langle\langle V_2\mathcal{E}_2^*\rangle\rangle-\langle\langle\varepsilon_2^4\rangle\rangle\langle\langle\varepsilon_2^2V_2\mathcal{E}_2^*\rangle\rangle)}{\langle\langle\varepsilon_2^6\rangle\rangle\langle\langle\varepsilon_2^2\rangle\rangle-\langle\langle\varepsilon_2^4\rangle\rangle^2}, \tag{40a}$$

$$\kappa_2'=\frac{\mathrm{Re}(-\langle\langle\varepsilon_2^4\rangle\rangle\langle\langle V_2\mathcal{E}_2^*\rangle\rangle+\langle\langle\varepsilon_2^2\rangle\rangle\langle\langle V_2\mathcal{E}_2^*\varepsilon_2^2\rangle\rangle)}{\langle\langle\varepsilon_2^6\rangle\rangle\langle\langle\varepsilon_2^2\rangle\rangle-\langle\langle\varepsilon_2^4\rangle\rangle^2}. \tag{40b}$$

Similarly for the triangular flow V_3,

$$\kappa_3=\frac{\mathrm{Re}(\langle\langle V_3\mathcal{E}_3^*\rangle\rangle\langle\langle\varepsilon_2^4\varepsilon_3^2\rangle\rangle-\langle\langle V_3\mathcal{E}_3^*\varepsilon_2^2\rangle\rangle\langle\langle\varepsilon_2^2\varepsilon_3^2\rangle\rangle)}{\langle\langle\varepsilon_3^2\rangle\rangle\langle\langle\varepsilon_2^4\varepsilon_3^2\rangle\rangle-\langle\langle\varepsilon_2^2\varepsilon_3^2\rangle\rangle^2}, \tag{41a}$$

$$\kappa_{23}'=\frac{\mathrm{Re}(-\langle\langle V_3\mathcal{E}_3^*\rangle\rangle\langle\langle\varepsilon_2^2\varepsilon_3^2\rangle\rangle+\langle\langle V_3\mathcal{E}_3^*\varepsilon_2^2\rangle\rangle\langle\langle\varepsilon_3^2\rangle\rangle)}{\langle\langle\varepsilon_3^2\rangle\rangle\langle\langle\varepsilon_2^4\varepsilon_3^2\rangle\rangle-\langle\langle\varepsilon_2^2\varepsilon_3^2\rangle\rangle^2}. \tag{41b}$$

In comparison with Eq. (39), when the cubic order response terms contribute, the resulting linear response coefficients κ_2 and κ_3 get extra *negative* corrections which scale as ε_2^2. The corrections are potentially significant at very peripheral collision bins. With the cubic order response, one may also plug in the estimated flow out of initial eccentricities in the evaluations of Pearson correlation coefficients. The resulting correlation is improved for both V_2 and V_3, but the improvements are not sizable.

The calculated result of these coefficients from viscous hydrodynamic simulations can be found in Fig. 8, as a function of centrality percentile [21]. The symbols are obtained with respect to Eq. (40) and Eq. (41) through event-by-event simulations of viscous hydrodynamics. Solid blue lines are the linear response coefficients from the single-shot hydrodynamic calculations. In the single-shot hydrodynamic calculations, hydrodynamic equations of motion are solved using a smooth initial condition, which is normally a deformed two-dimensional Gaussian distribution. The deformations can be introduced properly so that there is only one type of initial eccentricity involved in the initial state. Hence it involves single mode evolution.

In either type of calculation, the obtained linear response coefficients decrease as centrality percentile grows, in line with an increasing effect of viscous corrections in the medium system. The viscous effect is stronger in the event-by-event simulations using MC-Glauber initial conditions, although both calculations took the same value of η/s=0.08[1)]. It is consistent with the expectation in the linear response theory, that the response behavior diffuses with the diffusion proporntional to η/s. It is interesting to note that the viscous effect on cubic order response coefficient κ_2' is opposite, as κ_2' has a slight increase against the centrality percentile. Again, the increase is more evident in the results obtained from

1) An intuitive explanation can be given as follows: in event-by-event simulations with respect to random initial distributions, the calculated response contain all higher modes. Hense if response of higher modes are more sensitive to η/s, the viscous effects are expected stronger in the event-by-event calculations, comparing to the single-shot hydrodynamics where only the lowest order mode is calculated.

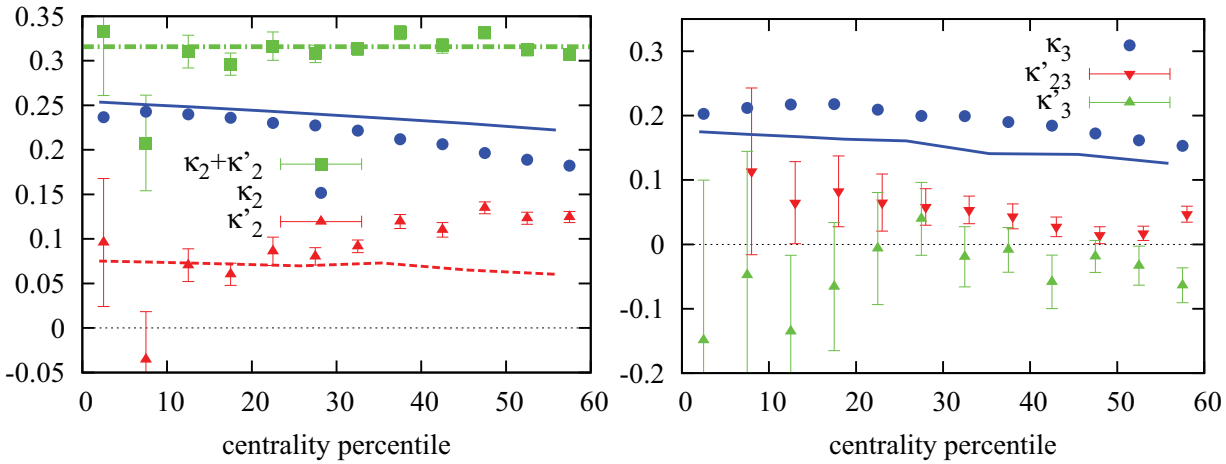

Fig. 8. (color online) Linear and cubic order response coefficients calculated from event-by-event hydro simulations for the Pb+Pb collisions of $\sqrt{s_{\rm NN}}=2.76$ TeV. Upper panel: elliptic flow. Lower panel: triangular flow. Reprinted figure with permission from J. Noronha-Hostler et al, Phys. Rev. C 93, 014909, 2016 (DOI: https://doi.org/10.1103/PhysRevC.93.014909) (Ref. [21]). Copyright 2016 by the American Physical Society.

event-by-event simulations. It is interesting to note that, for v_2, the sum of the linear and the cubic order response coefficients remains constant, regardless the change of centrality. Although nonlinear deviations in the scatter plot in Fig. 7 of V_3 are not obvious, a finite cubic order response coefficient κ'_{23} is found for Eq. (41). For comparison, the contribution from a cubic coupling of $\varepsilon_3^2\mathcal{E}_3$ to V_3 is examined in the calculations,

$$V_3=\kappa_3+\kappa'_3\varepsilon_3^2\mathcal{E}_3+\delta_3, \tag{42}$$

with the corresponding cubic order response coefficient κ'_3 found compatible with zero from the event-by-event hydrodynamic simulations.

2.3.3 Medium response in higher harmonic orders

When analyzing higher order flow harmonics in the flow paradigm, it is very useful to rewrite the $\mathcal{E}_2$ and $\mathcal{E}_3$ in terms of V_2 and V_3 in Eqs. (33), respectively,

$$V_4=V_4^L+\chi_{422}V_2^2+\delta_4 \tag{43a}$$
$$V_5=V_5^L+\chi_{523}V_2V_3+\delta_5 \tag{43b}$$
$$V_6=V_6^L+\chi_{633}V_3^2+\chi_{624}V_2V_4^L+\chi_{6222}V_2^3+\delta_6, \tag{43c}$$

where in a similar manner, the linear response part of higher order flow is left implicitly as V_n^L. By doing so, it becomes possible to analyze directly the quantitative relations among high order flow harmonics, and V_2 and V_3, so that ambiguities resulting from the definition of higher order eccentricities are avoided. Accordingly, uncertainties from the effective characterizations of initial state are reduced.

The re-expressions in terms of V_2 and V_3 are allowed in the expansion due to the fact that the linear response relation in the lower order flow harmonics is well approximated and has been tested in hydrodynamic simulations. Accordingly, there are new nonlinear flow response coefficients introduced. For the nonlinear contribution to V_4, χ_{422} quantifies how much the contribution comes from the mixing of V_2^2. For V_5, χ_{523} quantifies how much the contribution to V_5 is from the mixing of V_2V_3, etc. These new nonlinear response coefficients are related to those κ's written in Eqs. (33), e.g., $\chi_{422}=\kappa_{422}/\kappa_2^2$ and $\chi_{523}=\kappa_{523}/(\kappa_2\kappa_3)$.

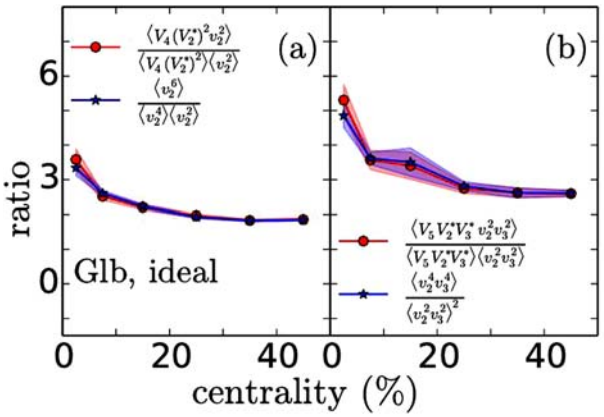

Fig. 9. (color online) A test of the uncorrelation between the linear and nonlinear parts of V_4 (left panel) and V_5 (right panel), based on event-by-event hydrodynamic simulations. Reprinted figure with permission from J. Qian, U. Heinz, and J. Liu, Phys. Rev. C 93, 064901, 2016 (DOI: https://doi.org/10.1103/PhysRevC.93.064901) (Ref. [20]). Copyright 2016 by the American Physical Society.

Let us emphasize again that, unlike the lower order flow, there is subtlety in interpreting the linear response of higher order flow harmonics as $V_n^L\propto\mathcal{E}_n$, due to the ambiguity in the $\mathcal{E}_n$ definitions. (Some recent hydrodynamic simulations suggest stronger correlations between

the linear part of V_4 and V_5 with the corresponding initial state eccentricities from cumulant definition [74].) Nevertheless, seen from Eqs. (43), one may recognize V_n^L as the part uncorrelated to the nonlinear response contributions in the higher order flow harmonics, on an event-by-event basis. Namely, one has the event averages $\langle\langle V_n^L V_n^{NL}\rangle\rangle=0$. As indicated in the expansion formulae, these event averaged correlators are assumed to vanish,

$$\langle\langle V_4^L (V_2^*)^2\rangle\rangle=0, \tag{44a}$$

$$\langle\langle V_5^L (V_2^* V_3^*)\rangle\rangle=0, \tag{44b}$$

$$\langle\langle V_6^L (\chi_{633} V_3^{*2}+\chi_{624} V_2^* V_4^{L*}+\chi_{6222} V_2^{*3})\rangle\rangle=0. \tag{44c}$$

Eqs. (44) are actually exact conditions on a general ground, as long as V_n^L is identified as the part of flow projected out of the plane composited from nonlinear mode mixings. Indeed, these relations in V_4 and V_5 have been found to hold approximately in hydrodynamics [20] and AMPT calculations [75]. Shown in Fig. 9 are some specified ratios from event-by-event hydrodynamic simulations, in which the implied identities are equivalent to the uncorrelation of the linear and nonlinear parts in v_4 and v_5 [65],

$$\frac{\langle\langle V_4 (V_2^*)^2 v_2^2\rangle\rangle}{\langle\langle V_4 (V_2^*)^2\rangle\rangle\langle\langle v_2^2\rangle\rangle}=\frac{\langle\langle v_2^6\rangle\rangle}{\langle\langle v_2^4\rangle\rangle\langle\langle v_2^2\rangle\rangle}, \tag{45a}$$

$$\frac{\langle\langle V_5 V_2^* V_3^* v_2^2 v_3^2\rangle\rangle}{\langle\langle V_5 V_2^* V_3^*\rangle\rangle\langle\langle v_2^2 v_3^2\rangle\rangle}=\frac{\langle\langle v_2^4 v_3^4\rangle\rangle}{\langle\langle v_2^2 v_3^3\rangle\rangle^2}. \tag{45b}$$

In experiments, measurements also support the conclusion that the linear and nonlinear parts in V_4 and V_5 are uncorrelated, as long as one consider V_n^L as the part of projection out of the plane composed from nonlinear mode mixings [76]. Given these results, further assumptions can be made for V_6, that all the nonlinear terms are not correlated with each other, i.e.,

$$\langle\langle V_6^L (V_2^*)^3\rangle\rangle=\langle\langle V_6^L (V_3^*)^2\rangle\rangle=\langle\langle V_6^L (V_2^* V_4^{L*})\rangle\rangle=0. \tag{46}$$

The analysis of higher order flow is simplified once the linear and nonlinear parts are uncorelated. In particular, the linear and nonlinear response of higher order flow for events in a centain centrality class are separable regarding the rms values. Taking V_4 as an example, the square of $v_4\{\text{rms}\}=v_4\{2\}$[1)] becomes the sum of the square of $v_4^L\{\text{rms}\}=v_4^L\{2\}$ and the square of $v_4^{NL}\{\text{rms}\}=v_4^{NL}\{2\}$,

$$v_4\{2\}^2=v_4^L\{2\}^2+v_4^{NL}\{2\}^2. \tag{47}$$

It is worth mentioning that the rms value of the nonlinear v_4 is identical to the projection of V_4 onto the plane determined by V_2^2, or more explicitly $2\Psi_2$. This is known as the $v_4\{\Psi_2\}$. Hence, by using the event-averaged quantities, $v_4^{NL}\{2\}$, or the projection $v_4\{\Psi_2\}$, is accessible in event-by-event hydrodynamic calculations and in experiments,

$$v_4^{NL}\{2\}=\frac{\text{Re}\langle\langle V_4 (V_2^*)^2\rangle\rangle}{\langle\langle |V_2|^4\rangle\rangle^{1/2}}\equiv v_4\{\Psi_2\}. \tag{48}$$

Note that the denominator is the fourth order moment of V_2, which in experiments should be measured with a rapdity-gap so that non-flow effects are not important. The linear part can be obtained accordingly,

$$v_4^L\{2\}=\sqrt{\langle\langle |V_4|^2\rangle\rangle-v_4\{\Psi_4\}^2}. \tag{49}$$

It is very similar for V_5, except that the plane from the nonlinear coupling of V_2V_3 is $\Psi_{23}=2\Psi_2+3\Psi_3$. The nonlinear part of v_5 is measured in the Ψ_{23} plane,

$$v_5^{NL}\{2\}=\frac{\text{Re}\langle\langle V_5 (V_2^* V_3^*)\rangle\rangle}{\langle\langle |V_2|^2 |V_3|^2\rangle\rangle^{1/2}}\equiv v_5\{\Psi_{23}\}, \tag{50}$$

which results in the linear part of v_5

$$v_5^L\{2\}=\sqrt{\langle\langle |V_5|^2\rangle\rangle-v_5\{\Psi_{23}\}^2}. \tag{51}$$

The sixth order harmonic flow has several types of nonlinear mode mixings. Except the one that involves linear response of the quadrangular flow V_4^L, there are planes well-defined in terms of V_3 of the quadratic order ($2\Psi_3$), and V_2 of cubic order ($3\Psi_2$). Measured in these specified planes respectively, one has v_6 projected onto Ψ_2 and Ψ_3 planes,

$$v_6\{\Psi_2\}\equiv\frac{\text{Re}\langle\langle V_6 (V_2^*)^3\rangle\rangle}{\langle\langle |V_2|^6\rangle\rangle^{1/2}}, \tag{52}$$

$$v_6\{\Psi_3\}\equiv\frac{\text{Re}\langle\langle V_6 (V_3^*)^2\rangle\rangle}{\langle\langle |V_3|^4\rangle\rangle^{1/2}}. \tag{53}$$

To extract the linear part of v_6, one would have to substract also the projected flow onto the $V_2V_4^L$ plane, which has not been done yet. Apart from that, the strategy has been applied in experiments to disentangle the linear and nonlinear parts in higher order flow [76, 77], leading to results consistent with those obtained by using the event-shape engineering method [78]. It is worth mentioning that the separated nonlinear part of the higher order harmonic flow is related to the measured event-plane correlations [65], which we discuss in Section 3.2.

The projection of higher order flow, and event-plane correlation, are understood in the flow paradigm as a combined effect of initial state geometry and medium dynamical expansion. Namely, they depends on the initial eccentricities and medium response coefficients in Eqs. (43), in a similar way to many other flow observables. However, a closer look at the formulae of the projections of higher flow harmonics reveals the possibility of extracting the nonlinear response coefficients χ's directly, by taking proper ratios with respect to the speci-

1) Taking into account the effect of event-by-event fluctuations, the quantity $v_4\{2\}$ is determined from two-particle correlations in experiments (or hydro simulations), whose definition and details will be given later.

fied moments

$$\begin{aligned}
\chi_{422} &= \frac{\langle\langle V_4(V_2^*)^2\rangle\rangle}{\langle\langle|V_2|^4\rangle\rangle} = \frac{v_4\{\Psi_2\}}{\sqrt{\langle\langle|V_2|^4\rangle\rangle}} \\
\chi_{523} &= \frac{\langle\langle V_5V_2^*V_3^*\rangle\rangle}{\langle\langle|V_2|^2|V_3^2|\rangle\rangle} = \frac{v_5\{\Psi_{23}\}}{\sqrt{\langle\langle|V_2|^2|V_3^2|\rangle\rangle}} \\
\chi_{6222} &= \frac{\langle\langle V_6(V_2^*)^3\rangle\rangle}{\langle\langle|V_2|^6\rangle\rangle} = \frac{v_6\{\Psi_2\}}{\sqrt{\langle\langle|V_2|^6\rangle\rangle}} \\
\chi_{633} &= \frac{\langle\langle V_6(V_3^*)^2\rangle\rangle}{\langle\langle|V_3|^4\rangle\rangle} = \frac{v_6\{\Psi_3\}}{\sqrt{\langle\langle|V_3|^4\rangle\rangle}}
\end{aligned} \tag{54}$$

These χ's are calculable in hydrodynamics, and measurable in experiments according to the expressions above. Note that these moments in the denominators are supposed to be entirely due to medium collectivity, thus in experiments non-flow contributions should be excluded carefully. By design, dependence on initial states eccentricities is cancelled in these ratios, hence χ's are not sensitive to the details of initial state. As a result, χ's are ideal probes reflecting directly the dynamical properties of the system evolution.

These nonlinear response coeffiicents have been measured in experiments at the LHC energies [76, 77]. Shown in Fig. 10 are the measured χ's as a function of centrality percentile, from the CMS collaboration. Compared to the direct measurements of higher order flow, the nonlinear response coefficients present weaker dependence on the collision centrality. Considering the major effect on flow observables from central to peripheral collisions due to the increase of medium viscous corrections, χ's are less affected by viscosity. This could be due to the cancellation of viscous effects in the ratios. Besides, there is also cancellation of statistical errors in the ratios, so that the measured nonlinear response coefficients are more accurate than their corresponding higher order flow.

In Fig. 10, the hydro calculations from VISH2+2 [20] and AMPT calculations [79] are shown as well, regarding different types of initial conditions and parameterizations of medium dissipative effects. The hydro results are compatible with experiments, in terms of overall magnitudes and centrality dependence, etc., although χ_{523} is apparently over-estimated. In contrast to the original proposal, the resulted nonlinear response coefficients do present dependence on initial conditions [20]. For instance, with the same $\eta/s = 0.08$, hydro gives larger χ_{422} with respect to the MC-Glauber initialization than MC-KLN. Similarly, MC-Glauber model leads to a larger value of χ_{6222}[1)]. Nonetheless, the dependence on initial conditions is quite weak in χ_{523} and χ_{633}.

Although viscous corrections to the χ's are expected to be minor, detailed hydro calculations have shown strong dependence of χ's on the freeze-out prescription. For instance, the χ's increase with respect to a lower freeze-out temperature in hydrodynamic simulations. Most of the viscous effects on χ's come from the viscous corrections to the phase space distribution function δf at freeze-out [20], which signifies the importance of χ as a probe for future studies on the physics of freeze-out and particle generation.

It is very likely that the nonlinear mode mixings in hydrodynamic modeling are dominantly generated during the freeze-out process, which can be explained in a quantitative way as follows. In ideal hydrodynamics, the nonlinear mode mixings at freeze-out lead the prediction that, at fixed and large transverse momentum $p_{\rm T}$, $\chi_{422} = \frac{1}{2}$, $\chi_{523} = 1$, $\chi_{6222} = \frac{1}{6}$, and $\chi_{633} = \frac{1}{2}$ [80]. The integrated value of χ's are further modified by a factor from an average over the $p_{\rm T}$ spectrum. For the nonlinear response coefficients associated with quadratic order couplings, the factor is roughly $\langle v^2\rangle/\langle v\rangle^2 > 1$, where single brackets indicate the integrated flow (v_2 or v_3) according to the $p_{\rm T}$ spectrum in a single hydro event. For those from the cubic order couplings, a larger factor is expected, $\langle v^3\rangle/\langle v\rangle^3 > \langle v^2\rangle/\langle v\rangle^2$. Since v_2 and v_3 have roughly similar $p_{\rm T}$ dependence, the ratios are comparable for χ_{422}, χ_{523} and χ_{633}, and comparable for χ_{6222} and χ_{7223}. As a consequence, in the flow paradigm captured by hydrodynamics, one expects the approximate relations $\chi_{422} \sim \chi_{633} \sim \frac{1}{2}\chi_{523}$ and $\chi_{6222} \sim \frac{1}{3}\chi_{7223}$. These approximate relations are confirmed in experimental observations. Accordingly, up to a semi-analytical level, these observed relations demonstrate the success of the flow paradigm, and especially, the proposed medium response relations.

2.3.4 Fluctuations in the medium response

Even though all the linear and nonlinear responses in the medium are well understood, or have been quantitatively characterized in a hydro simulation, the predicted flow observables are not deterministic, owing to random fluctuations. As well as fluctuations of initial state eccentricities, there are also fluctuations associated with the dynamics of medium response, which in the expansion formulae Eqs. (33) are captured by the residual δ_n's.

In writing residuals in the expansion form, there are two assumptions: 1) It is assumed that δ_n has the same rotational symmetry in the azimuth as V_n; 2) The residual δ_n should be statistically uncorrelated with the rest of the terms in the expansion in Eqs. (33), i.e., one ex-

1) One possible explanation for the discrepancy is that the KLN model has a more elliptic averaged background, which results in a larger prediction of v_2. Accordingly, higher order mode mixings involving V_2 are required in the expansion form Eqs. (43), to give a good description of higher order flow. However, these new terms are not considered in the definitions of nonlinear response coefficients. On the other hand, these calculations indeed show that χ_{523} and χ_{633} have weak sensitivity to initial conditions, where the role of V_2 is less significant.

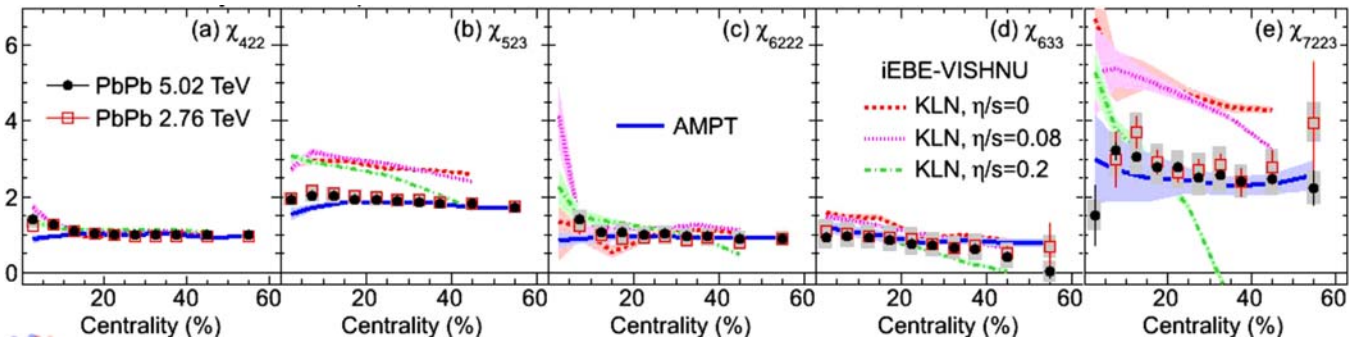

Fig. 10. (color online) Non-linear response coefficients measured by the ALICE collaboration with respect to Pb+Pb collisions at $\sqrt{s_{\rm NN}}$=2.76 TeV, as a function of centrality percentile. Hydro calculations are shown for comparisons. Figure reproduced from Ref. [77] (DOI: https://doi.org/10.1016/j.nuclphysa.2017.05.064), under the CC-BY 4.0 license (http://creativecommons.org/licenses/by/4.0/).

pects vanishing correlations of δ_n and initial eccentricities, $\langle\langle\delta_n\mathcal{E}_m^*\rangle\rangle=0$. There are two possible origins of the residual δ_n in heavy-ion collisions. It can be understood as an inadequate characterization of the flow generation on an event-by-event basis, so that additional effects related to initial state fluctuations contribute, δ^{ini}. On the other hand, it can be a consequence of thermal fluctuations, δ^{th}. The former can be studied in the present framework of event-by-event hydro simulations, without considering thermal fluctuation effects.

As has been shown in Fig. 5 and Fig. 7, the response of v_2 and v_3 disperse around the prediction of linear and/or linear+cubic response, indicating the effects of δ_2 and δ_3 on an event-by-event basis. One would expect these residuals to be generated from the hydro response to short-scale structures in the initial state density profile. Indeed, the dispersion, or the rms value of δ_n, is suppressed as viscosity applied in these calculations is increased. It is also consistent with the observation that dispersion in triangular flow is stronger, where the role of short-scale structures is relatively more important than that in the elliptic flow. Therefore, one may associate the effect of δ_n with initial state fluctuations, which scale as $1/\sqrt{N_p}$, with N_p being the number of participants. Shown in Fig. 11 are the corresponding results from event-by-event hydro simulations, with respect to Pb+Pb collisions at $\sqrt{s_{\rm NN}}=2.76$ TeV. The rescaled rms values of the residual vary within a factor of two when centrality increases, considering the fact that $\sqrt{N_p}$ changes by a factor 10.

The presence of thermal fluctuations can be decomposed into similar mode structures. That is to say, for each of the harmonic orders, in the medium evolution there is a fluctuating mode correspondingly originated from thermal fluctuations [26], in addition to the averaged response coefficients. Although the effects of thermal fluctuations can be absorbed formally in the residuals of the response relations Eqs. (33) as δ_n^{th}'s, the origins of thermal fluctuations are distinct from those related to the initial state, δ_n^{ini}'s.

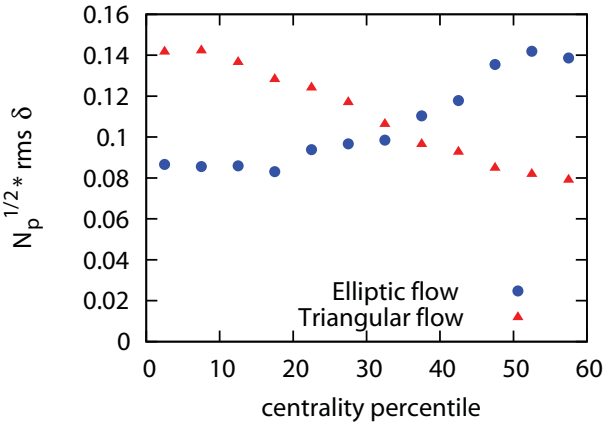

Fig. 11. (color online) Rms values of the residual δ_n scaled by $\sqrt{N_p}$, from event-by-event hydro simulations with respect to Pb+Pb collisions at $\sqrt{s_{\rm NN}}$ = 2.76 TeV, as a function of centrality. Reprinted figure with permission from J. Noronha-Hostler et al, Phys. Rev. C 93, 014909, 2016 (DOI: https://doi.org/10.1103/PhysRevC.93.014909) (Ref. [21]). Copyright 2016 by the American Physical Society.

Several remarks are in order with respect to the effects of thermal fluctuations in the generation of harmonic flow. First, a thermodynamical origin guarantees the condition $\langle\langle\delta_n^{th}\mathcal{E}_m\rangle\rangle=0$ and $\langle\langle\delta_n^{th}\delta^{ini}\rangle\rangle=0$. Therefore, in the two-particle (or multi-particle) correlations, contributions from a thermal origin and a quantum origin are separable. Second, the effects of fluctuations are controlled in principle by the fluctuation strength, in terms of the two-point auto-correlations. For the effects associated with initial state fluctuations, one has parameterically

$$\langle\langle\delta^{ini}\delta^{ini}\rangle\rangle\sim 1/N_p \quad \text{or} \quad \langle\langle\varepsilon_n^2\rangle\rangle\sim 1/N_p. \tag{55}$$

On the other hand, two-point auto-correlations of thermal fluctuations are determined by the dissipative cor-

rections of the medium system through the flutucation-dissipation relation [26],

$$\langle\langle\delta^{th}\delta^{th}\rangle\rangle\sim\frac{\eta}{s}\Big/\Big\langle\Big\langle\frac{\mathrm{d}S}{\mathrm{d}y}\Big\rangle\Big\rangle. \tag{56}$$

with an extra factor quantified by the inverse of the total entropy per rapidity. From Eq. (55) and Eq. (56), one realizes that the contributions from thermal fluctuations to the two-particle correlation are suppressed parametrically by a factor of $(\eta/sK_s)^{1/2}$, where the constant $K_s\gg1$ is associated with the entropy production from nucleon-nucleon collisions. Therefore, even though in higher order flow harmonics thermal fluctuations are expected stronger [24, 26], the overall effects of thermal fluctuations in the observed flow are *not* significant compared to those from the initial state, unless on the occasions that the system is sufficiently close to the QCD critical point. Third, the previous estimates of the thermal fluctuations are obtained with an inclusion of the thermal fluctuations *linearly* in hydrodynamics in a canonical way, corresponding to the gradient expansion. Recently, however, it was found that the nonlinear feature of hydrodynamics results in non-linear couplings of thermal fluctuations, and a distinct behavior is achieved with the appearance of a fractional order term in the gradient expansion $O(\nabla^{3/2})$. This is the generic property of long-time tails in hydrodynamics [81, 82], which has conceptual influences in the theoretical framework. In particular, nonlinear couplings of the thermal fluctuations effectively modify transport coefficients, such as η [83, 84] and ζ [85, 86].

3 Experimental observables in nucleus-nucleus collisions

In this section, we summarize some of the observables in heavy-ion experiments that are compatible with the flow paradigm. We shall start with an overview of the measured harmonic flow from multi-particle correlations. For comparison, corresponding predictions from hydrodynamics are shown with properly parameterized transport coefficients, such as η/s, ζ/s. These are concrete examples showing how these coefficients are estimated in the analyses in the flow paradigm.

The concept of the flow paradigm depends essentially on the system collective expansion. The most convincing evidence of the system collective expansion in heavy-ion collisions comes from the observed structures in long-range multi-particle correlations. This is because, once a medium system expands collectively, the short-scale structures at initial times are amplified in space as time evolves, leading to long-range correlations. Normally, these long-range correlations are beyond the prediction of first principle calculations based on particle scatterings or classical fields at early evolution stages, if late-time medium evolution is ignored. In heavy-ion collisions, this long-range correlation is particularly recognized in the long-range correlations in rapidity, or pseudo-rapidity η (it should be distinguished from the notation of shear viscosity)[1)].

One typical example can be found in Fig. 12, which depicts the measured two-particle correlation functions in relative azimuthal angle $\Delta\phi$ and relative pseudo-rapidity $\Delta\eta$, from the CMS collaboration with respect to the Pb+Pb collisions at $\sqrt{s_{\rm NN}}$=2.76 TeV, and p+Pb collisions at $\sqrt{s_{\rm NN}}=5.02$ TeV. The collision events are purposely selected for illustration, in a way that the multiplicity productions in Pb+Pb and p+Pb are comparable and sufficiently large. Despite some fine details, one notices the very similar long-range correlation structures at large $\Delta\eta$. Especially, at $\Delta\phi=0$ (near-side), a bump appears in the Pb+Pb system, which is sometimes referred to as the "ridge". The "ridge" indicates a long-range correlation pattern which is expected from the medium collective expansion scenario. Note that these Pb+Pb events correspond to peripheral collisions. In more central collisions of larger multiplicity productions, the ridge, and thus the system collective expansion, is more obvious. On the contrary, as one might expect, the "ridge" is absent in the two-particle correlation functions when the corresponding multiplicity production of the collision event is small (see for instance Ref. [87] for p+p collisions), or the trigger or associated particles are not soft.

Given the single-particle spectrum written in terms of harmonic flow V_n in Eq. (12), the two-particle correlation function can be described accordingly,

$$\Big\langle\Big\langle\frac{\mathrm{d}N^{pair}}{\mathrm{d}\Delta\phi}\Big\rangle\Big\rangle=\Big\langle\Big\langle\frac{\mathrm{d}N_a}{d\phi_a}\frac{\mathrm{d}N_b}{d\phi_b}\Big\rangle\Big\rangle\sim1+\sum_{n=1}^{\infty}\langle\langle V_nV_n^*\rangle\rangle\mathrm{e}^{\mathrm{i}n\Delta\phi}, \tag{57}$$

which explains the bump in Fig. 12 at $\Delta\phi$=0 as a consequence of the non-zero correlation structure, $\langle\langle V_n^aV_n^{b*}\rangle\rangle\equiv V_{n\Delta}$. Normally, a fit using Eq. (57) for the two-particle correlation function allows one to estimate the magnitude of harmonic flow v_n in experiments. More precisely, it defines the the measured flow using the scalar-product method, or the two-particle cumulant $v_n\{2\}$,

$$v_n\{2\}^2=\langle\langle v_n^2\rangle\rangle\equiv\langle\langle\mathrm{e}^{\mathrm{i}n(\phi_p^a-\phi_p^b)}\rangle\rangle=\langle\langle V_n^aV_n^{b*}\rangle\rangle. \tag{58}$$

The quantities $v_n\{2\}$ are the most generally measured harmonic flow signatures that contain the information of

1) For the convenience of later discussions, we assume the configuration of a colliding system as being to align the beam-axis with the z-axis, while the plane perpendicular to the beam-axis is recognized as the transverse plane. When the nucleus-nucleus collisions are not head-on collisions, there is a non-zero impact which defines the x-axis. The direction of the impact, together with the beam-axis, determine the reaction-plane Ψ_R.

the magnitude of V_n. They must be measured in experiments in the correlated particle spectra as a consequence of event-by-event fluctuations of V_n.

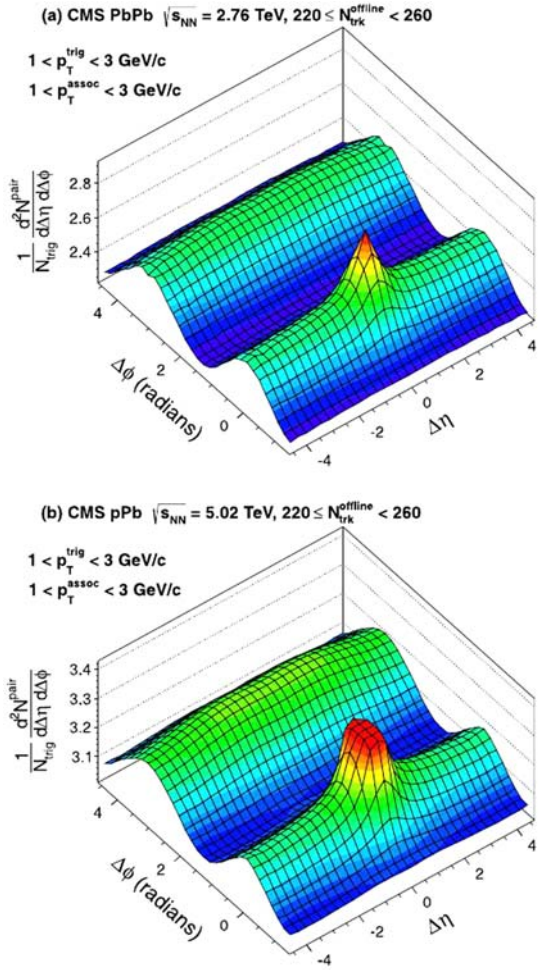

Fig. 12. (color online) Two-particle correlation functions measured by the CMS collaboration, for the Pb+Pb collisions at $\sqrt{s_{\rm NN}}$ = 2.76 TeV (up) and p+Pb collisions at $\sqrt{s_{\rm NN}}$ = 5.02 TeV (down). Collision events in p+Pb and Pb+Pb are selected with comparable and sufficiently large multiplicity productions. In these events, long-range correlation patterns can be identified as the "ridge" structure: the bump span along relative pesudo-rapidity at $\Delta\phi = 0$. Trigger and associated particles are chosen in the low $p_{\rm T}$ range. Figure reproduced from Ref. [88] (DOI: https://doi.org/10.1016/j.physletb.2013.06.028, under the CC-BY-NC-ND license).

As an example, Fig. 13 presents the recently measured flow harmonics, using the scalar-product method for the correlated two-particle spectra, as a function of collision centrality. The symbols correspond to elliptic flow $v_2\{2\}$ (black), the triangular flow $v_3\{2\}$ (red) and the quadrangular flow $v_4\{2\}$ (green), in the Pb+Pb system of $\sqrt{s_{\rm NN}} = 5.02$ TeV, by the ALICE collaboration. Hydro calculations from IP-Glasma+MUSICS with an input $\eta/s = 0.095$ and a parameterized temperature dependent bulk viscosity over entropy density ratio ζ/s are shown in solid lines. One notices an increasing trend of the flow harmonics along with the increase of collision centrality percentile[1]. The increasing trend of the flow harmonics and the magnitude of each flow harmonics, are both captured quantitatively by hydro calculations.

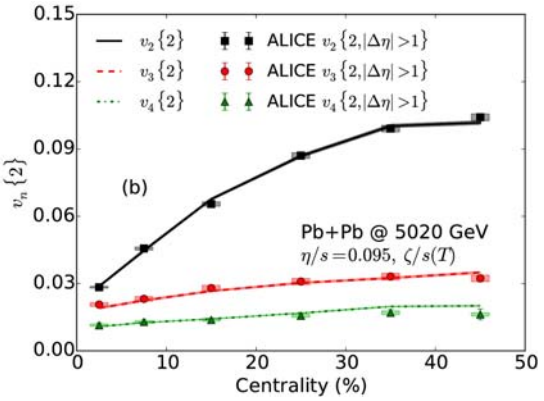

Fig. 13. (color online) Harmonic flow measured from two-particle correlations from the ALICE collaboration for the Pb+Pb at $\sqrt{s_{\rm NN}}$ = 5.02 TeV. Lines are corresponding results from hydrodynamic simulations, with a constant value of $\eta/s = 0.095$ and a temperature dependent parameterization of ζ/s. Reprinted figure with permission from S. McDonald et al, Phys. Rev. C 95, 064913, 2017 (DOI: https://doi.org/10.1103/PhysRevC.95.064913) (Ref. [19]). Copyright 2017 by the American Physical Society.

As we mentioned before, harmonic flow $v_n\{2\}$ can be also measured differentially in experiments as a function of the transverse momentum $p_{\rm T}$. These differential spectra of harmonic flow are obtained from two-particle correlations, assuming a factorization of the correlation [89]

$$\langle\langle V^n(p_{\rm T}^a)V_n^*(p_{\rm T}^b)\rangle\rangle \Rightarrow v_n\{2\}(p_{\rm T}^a)\times v_n\{2\}(p_{\rm T}^b). \quad (59)$$

However, the above factorization can be broken. In the flow paradigm where a single-particle spectrum is well-established from hydrodynamic calculations, one has generally [90]

$$\langle\langle V^n(p_{\rm T}^a)V_n^*(p_{\rm T}^b)\rangle\rangle \leqslant v_n\{2\}(p_{\rm T}^a)\times v_n\{2\}(p_{\rm T}^b), \quad (60)$$

1) Centrality percentile is used to identify collision events with respect to multiplicity production. A centrality percentile approaching to zero implies the collision with the largest multiplicity production of the whole events, namely, approximately head-on collisions in nucleus-nucleus collisions. On the other hand, centrality percentile close to 100% corresponds to very peripheral collisions with very small particle yields.

with the equality satisfied only when the complex variables $V_n(p_{\rm T}^a)$ and $V_n(p_{\rm T}^b)$ are linearly dependent. That is to say, there exists a $p_{\rm T}$-dependent function that does not fluctuate from event to event in one centrality class. When the effects of initial state fluctuations are sizable, the linear dependent relation is broken, which in turn result in the breaking of the factorization in Eq. (59). In particular, the breaking of factorization is expected to be stronger when the difference $p_{\rm T}^a - p_{\rm T}^b$ increases, owing to the effect of initial state fluctuations. Breaking of the factorization also implies a $p_{\rm T}$-dependent flow angle $\Psi_n(p_{\rm T})$ [91]. Eq. (60) is a Cauchy-Schwarz inequality derived by correlating single-particle spectra. Therefore, violation of Eq. (60) can be seen as an indication of non-flow contribution. A quantity r_n is introduced accordingly [90],

$$r_n \equiv \frac{V_{n\Delta}(p_{\rm T}^a, p_{\rm T}^b)}{\sqrt{V_{n\Delta}(p_{\rm T}^a, p_{\rm T}^a)}\sqrt{V_{n\Delta}(p_{\rm T}^b, p_{\rm T}^b)}} \tag{61}$$

to quantify these effects. Indeed, experiments have found violation of the inequality Eq. (60) with respect to large transverse momentum, that $r_n > 1$. Besides, a decreasing trend of r_n is confirmed regarding the growth of the relative difference transverse momentum $p_{\rm T}^a - p_{\rm T}^b$ [89, 92], which are compatible with hydrodynamics [91, 93]

In addition to the two-particle correlation function, in realistic analyses in experiments, the measurements of flow harmonics also generalize to multi-particle correlations. Systematic generalization to four-, six- and eight-particle spectra leads to the measured cumulants of harmonic flow $v_n\{4\}$, $v_n\{6\}$ and $v_n\{8\}$ [56, 95]

$$v_n\{4\}^4 = 2\langle\langle v_n^2\rangle\rangle^2 - \langle\langle v_n^4\rangle\rangle \tag{62a}$$

$$v_n\{6\}^6 = \frac{1}{4}[\langle\langle v_n^6\rangle\rangle - 9\langle\langle v_n^4\rangle\rangle\langle\langle v_n^2\rangle\rangle + 12\langle\langle v_n^2\rangle\rangle^3] \tag{62b}$$

$$\begin{aligned} v_n\{8\}^8 = \frac{1}{33}\Big[&-\langle\langle v_n^8\rangle\rangle + 16\langle\langle v_n^6\rangle\rangle\langle\langle v_n^2\rangle\rangle + 18\langle\langle v_n^4\rangle\rangle^2 \\ &-144\langle\langle v_n^4\rangle\rangle\langle\langle v_n^2\rangle\rangle^2 + 144\langle\langle v_n^2\rangle\rangle^4\Big], \end{aligned} \tag{62c}$$

where self-correlations are subtracted by definition. With respect to correlations of all particle yields in the collision events, there exists the Lee-Yang zero method and correspondingly harmonic flow $v_n\{\rm LY\}$ [96].

In heavy-ion experiments at RHIC and the LHC, flow cumulants have been measured up to $v_2\{8\}$ in nucleus-nucleus collisions for the elliptic flow, as summarized in Table 1. Fig. 14 displays the recent results of the cumulants of elliptic flow from multi-particle correlations from the ALICE collaboration [94], in the Pb+Pb collisions at $\sqrt{s_{\rm NN}}$=2.76 TeV and $\sqrt{s_{\rm NN}}$=5.02 TeV. Higher order cumulants of v_2 tend to collapse, although they present similar centrality dependence as $v_2\{2\}$. Note that there is a gap between $v_2\{2\}$ and these higher order cumulants, which grows as centrality increases. As will be discussed later, the gap and the tiny splitting among higher order flow cumulants signify the non-Gaussian behavior of v_2 flucutations.

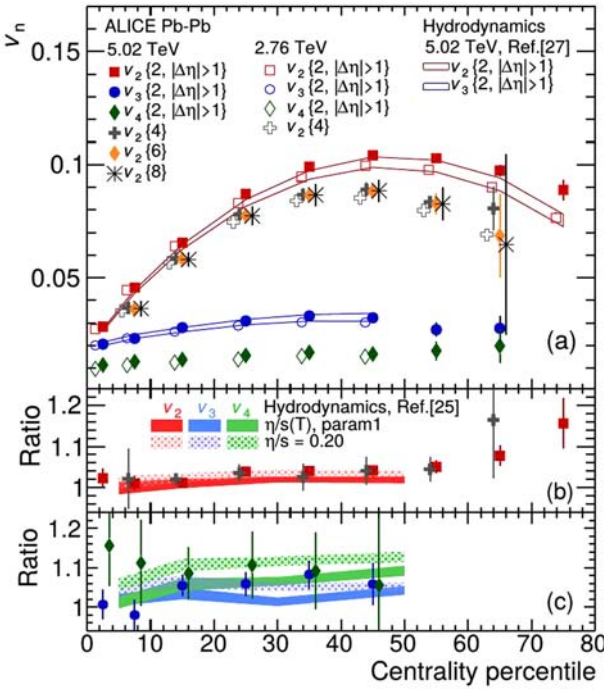

Fig. 14. (color online) Harmonic flow measured from multi-particle correlations from the ALICE collaboration for the Pb+Pb at $\sqrt{s_{\rm NN}}$ = 5.02 TeV, in comparison to that from the Pb+Pb at $\sqrt{s_{\rm NN}}$ = 2.76 TeV. Lines are corresponding results from hydrodynamic simulations. Figure reproduced from Ref. [94] (DOI: https://doi.org/10.1103/PhysRevLett.116.132302, "Anisotropic flow of charged particles in Pb-Pb collisions at $\sqrt{s_{\rm NN}}$ = 5.02 TeV"), under the CC-BY-3.0 license.

These cumulants of V_n are of particular significance with respect to the fluctuating nature of heavy-ion collisions, since they provide a quantitative characterization of the flow event-by-event fluctuations. For instance, $v_n\{2\}$ captures the variance of flow distribution on an event-by-event basis [97], while $v_n\{4\}$ and $v_n\{6\}$ can be used to measure the skewness [98]. Additionally, flow measurements from multi-particle correlations have the advantage of suppressing non-flow contributions [99]. Note that in Fig. 13 and Fig. 14, a rapidity gap of $|\Delta\eta|>1$ has been applied to the measured two-particle spectra to suppress non-flow contributions, assuming that non-flow effects are dominantly short-ranged.

Besides the measurements involving the same harmonic orders, one is allowed to extract the correlations among mixed harmonic orders. In this way, the informaiton of the phase Ψ_n becomes detectable. Unlike the cumulants of harmonic flow which reflect the fluctuation

porperties of the colliding systems, to a large extent, flow correlations measure the correlation properties of flow angles on an event-by-event basis. There are several types of correlators of the mixed harmonics that have been investigated in experiments, including event-plane correlations first measured by the ATLAS collaboration ρ_{mn} [100], the symmetric cumulants $SC(m,n)$ proposed by the ALICE collaborations [101], and the three plane event-plane correlators recently measured by the STAR collaboration at the RHIC energy [102, 103].

Figure 15 displays a set of event-plane correlations measured by the ATLAS collaboration with respect to the Pb+Pb collisions at $\sqrt{s_{\rm NN}}=2.76$ TeV. Hydro simulations with the EKRT initial condition using different types of parameterization of η/s are shown as lines. Hydro predictions generally capture the right trend and sign of correlations, while the correlation strength is found to be further affected by the dissipative properties of the medium [10]. Note that an overall agreement is best achieved when a constant $\eta/s=0.2$ ($\zeta/s=0$) is taken in the simulations. Since all other parameterizations involves a temperature dependent η/s, which on average introduce effectively smaller dissipations to hydro simulaitons, one realizes that the event-plane correlations are stronger in a more dissipative fluid, which property we shall detail later in the context of the flow paradigm.

Figure 15 is again a typical example demonstrating the extraction of η/s from the hydro modeling of heavy-ion collisions. These flow observables are by far the best probes for the extraction of η/s of the QGP system in heavy-ion collisions. It has been found from hydro simulations that a quite small value of $\eta/s\approx0.08$ is realized in the system created from Au+Au at RHIC [104], while at the LHC energies one would expect a larger value.

In addition to these aforementioned flow observables, there are many other types of measurements associated with the obvserved long-range multi-particle correlations, and flow harmonics, supporting the concept of system collective expansion in nucleus-nucleus collisions. Similar measurements have also been generalized recently to small colliding systems, e.g., p+Pb at the LHC energies, where medium collectivity is observed in collision events of sufficiently high multiplicity. We summarize them in Table 1. Similar to the results shown in Fig. 13 and Fig. 15, all of these observables agree with hydrodynamic simulations, to a quantitative level, upon specified parameterization of initial state, equation of state, and transport coefficients. Thereby, a flow paradigm based on hydro modelings of heavy-ion experiments is very well established.

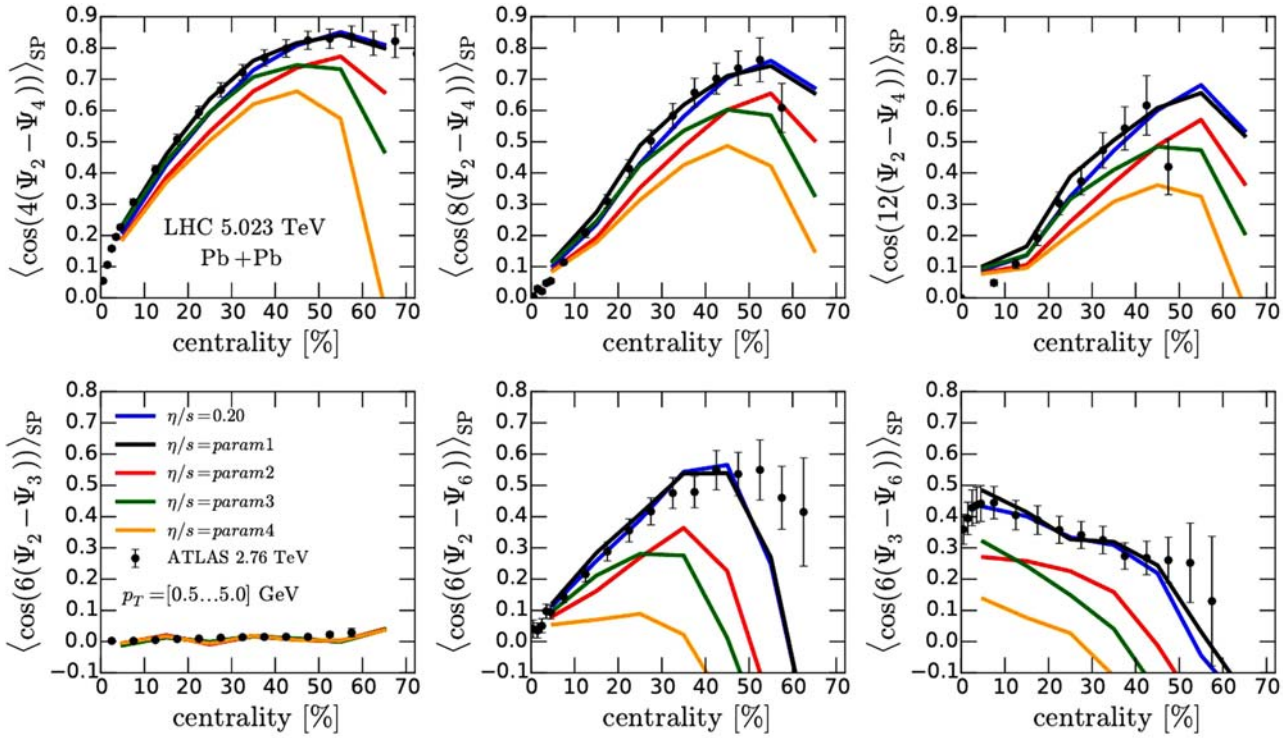

Fig. 15. (color online) Event-plane correlations measured with respect to the Pb+Pb collisions at $\sqrt{s_{\rm NN}}=2.76$ TeV by the ATLAS collaboration [100], using the scalar-product method. Lines of different colors correspond to hydro simulations with respect to the Pb+Pb collisions at $\sqrt{s_{\rm NN}}=5.02$ TeV, with various parameterizations of η/s, and with EKRT initial condition. Reprinted figure with permission from H. Niemi et al, Phys. Rev. C 93, 014912, 2016 (DOI: https://doi.org/10.1103/PhysRevC.93.014912) (Ref. [10]). Copyright 2016 by the American Physical Society.

Table 1. A summary of flow observables measured in experiments

flow observables	harmonic order involved	colliding systems	dependence
$v_n\{2\}$	n= 1,2,3,4,5,6	PbPb, pPb, dAu, He^3Au AuAu	centrality, p_T, particle species, pseudo-rapidity
$v_n\{4\}$	n= 2,3	PbPb	centrality
$v_n\{6\}$	n=2	PbPb	centrality
$v_n\{8\}$	n=2	PbPb	centrality
r_n	n=2,3	PbPb, pPb	centrality,p_T,pseudo-rapidity
event-by-event flow distribution $\mathbb{P}(v_n)$	n= 2,3,4	PbPb	centrality
event-plane correlation	$n\leqslant 6$	PbPb, AuAu	centrality, pseudo-rapidity
projection of V_n onto lower haromincs	$v_4\{\Psi_2\}$, $v_6\{\Psi_3\}$, $v_7\{\Psi_{23}\}$	PbPb, AuAu	centrality, p_T
nonlinear medium response coefficients	n= 4,5,6,7	PbPb	centrality
symmetric cumulants	$n\leqslant 5$	PbPb, pPb	centrality

In the following discussions of the section, we select several flow observables in experiments. These observables are categorized into two sets. One is related to the fluctuations of harmonic flow, and the other contains information about flow correlations. It is our purpose to demonstrate, in the framework of flow paradigm, in particular, in terms of the analytic response relations we have shown in the previous sections, that these observables can be understood to a quantitative level. Various constraints from these observables, and also schemes developed correspondingly to reduce uncertainties from inital state modelings, help to improve the precision in the extraction of the medium transport coefficients.

3.1 Event-by-Event fluctuations of v_n

As discussed, event-by-event fluctuations in the observed flow signatures are mostly from initial state eccentricities. Although there is no direct measurement of initial stages in heavy-ion collisions available, fluctuating behavior of the flow harmonics provides the best probes of the fluctuations among the initial state of nucleon-nucleon collisions. Fluctuations of flow harmonics can be studied in terms of the probability distribution $\mathbb{P}(v_n)$ of the flow magnitude v_n, or in a more quantitatively manner, the cumulants of harmonic flow. The quantitative analysis in this section depends on the linear response relation, $v_n=\kappa_n\varepsilon_n$, which is approximately valid for the lower order flow harmonics, v_2 and v_3, although effects due to nonlinear mode couplings are strong in some particular observables.

3.1.1 Fitting event-by-event flow fluctuations

The ATLAS collaboration managed to measure the event-by-event distribution of harmonic flow in Pb+Pb collisions at $\sqrt{s_{\rm NN}}=2.76$ TeV [101], using an unfolding procedure to subtract non-flow effects [97, 105]. The strategy has been applied recently by the CMS collaboration, with respect to the updated Pb+Pb collisions at $\sqrt{s_{\rm NN}}=5.02$ TeV [106]. Shown in Fig. 16 are the measured results of event-by-event distribution of v_2 (left panel), v_3 (middle panel) and v_4 (right panel), by the ATLAS collaboration, for different centrality classes.

The first attempt of fitting (and also interpreting) the probability distribution involves a pure Gaussian parameterization, which has been applied in Fig. 16 to fit the event-by-event flow distribution (indicated as the solid curves),

$$\mathbb{P}(v_n)=\frac{v_n}{\sigma_n^2}{\rm e}^{-v_n^2/2\sigma_n^2}. \tag{63}$$

A pure Gaussian corresponds to the Bessel-Gaussian function with a vanishing mean anisotropy v_0=0, which gives rise to better description of v_3 than v_2, as expected. Note that in Fig. 16 the Gaussia fit is only available for v_2 of the ultra-central collisions. However, even for v_3, non-Gaussian behavior is observed in collisions of larger centralities. It should be noted that the fitting procedure using a Gaussian function reveals very little information about the initial state fluctuations, nor about the dissipative properties of the medium evolution. It should also be noted that the probability distribution of v_4 is more complicated in its physical origin, accounting for nonlinear medium response, which we shall address later.

With the help of the formulae Eqs. (33) to relate magnitudes v_n and ε_n, for the elliptic flow and triangular flow, one finds a change of variable

$$\mathbb{P}(v_n)=\frac{d\varepsilon_n}{dv_n}P(\varepsilon_n^{-1}(v_n)), \tag{64}$$

can be applied to rewrite the distribution function of flow harmonics in terms of the probability distribution of initial state eccentricities. For the linear response dominated scenario, in v_2 and v_3, the above relation is simply a rescaling of the initial state eccentricity distribution,

$$\mathbb{P}(v_2)=\frac{1}{\kappa_2}P(v_2/\kappa_2),\qquad \mathbb{P}(v_3)=\frac{1}{\kappa_3}P(v_3/\kappa_3). \tag{65}$$

For the initial state eccentricity distribution characterized by the elliptic-power Eq. (25) or power distribution Eq. (26), the rescaling introduces one extra parameter, the linear response coefficient κ_n. Therefore, it becomes possible to extract directly the linear response coefficient from the probability distribution of flow. In addition to

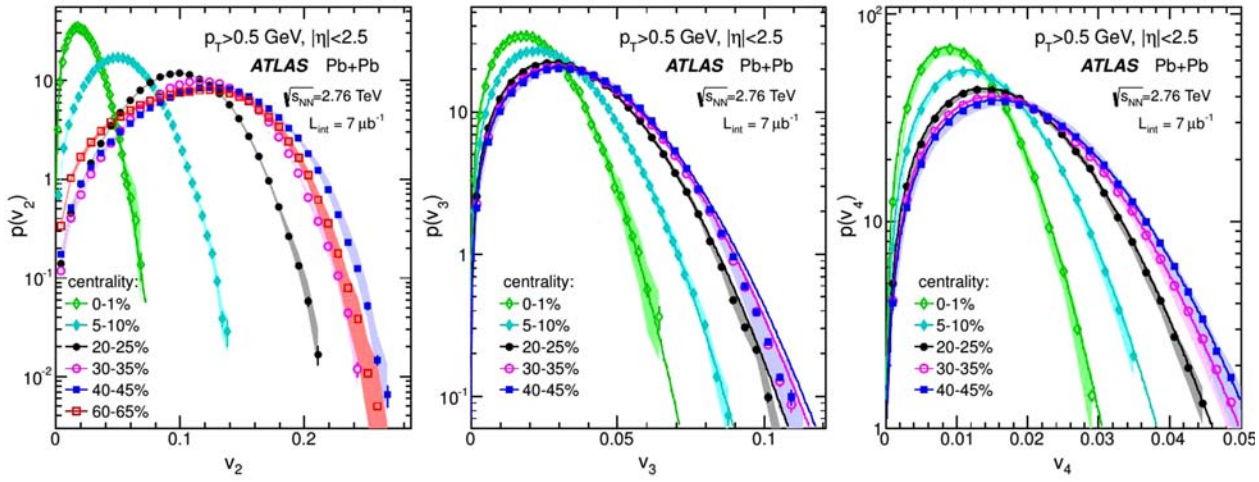

Fig. 16. (color online) Probability distribution of flow magnitude $\mathbb{P}(v_n)$, measured by the ATLAS collaboration for the Pb+Pb collisions at $\sqrt{s_{\rm NN}}=2.76$ TeV. Left panel: elliptic flow v_2. Middle panel: triangular flow v_3. Right panel: quadrangular flow v_4. Figure reproduced from Ref. [97] (DOI: https://doi.org/10.1007/JHEP11(2013)183), under the CC-BY-NC-ND license.

κ_n, fitting to flow fluctuations also identifies the parameters α and/or ε_0, which captures in the initial state the fluctuation strength and mean eccentricity.

In a similar manner, one may consider applying the rescaled Bessel-Gaussian function for the parameterization of initial state eccentricity fluctuations, so that the linear response coefficient κ_n can be determined simultaneously with σ and ε_0, the parameters in the original Bessel-Gaussian distribution function. However, because the Bessel-Gausian function (or Gaussian) is scale invariant, for which a rescaling the distribution is equivalent to $\sigma\to\kappa_n\sigma$ and $\varepsilon_0\to\kappa_n\varepsilon_0$, the fitting procedure cannot constrain the value of κ_n, nor σ or ε_0 individually. Actually, the ability to disentangle initial state parameters and the linear response coefficients, relies on the non-Gaussianity of the flow fluctuations.

The left-hand panel of Fig. 17 presents the extracted values of κ_n, from the fit of ATLAS measured v_2 and v_3 distributions, with Elliptic-Power and Power parameterizations. The linear response coefficients κ_2 and κ_3 decrease monotonically as centrality percentile increases. This is expected, since viscous effects get stronger in smaller collision systems, leading to a suppressed medium response. In comparison with hydro predictions, the centrality dependence of linear response coefficients allows one to estimate the value of η/s. In the left-hand panel of Fig. 17, hydro calculations with $\eta/s\simeq0.19$ (green lines) are found to give rise to the best description. It should be emphasized that uncertainties normally induced from initial state effective modelings are reduced in the present procedure of estimating η/s.

Simultaneously, the fit of flow event-by-event distribution results in the extracted values of α and ε_0, which are shown in the middle panel and the right-hand panel of Fig. 17, respectively. Recalling that the parameter α characterizes the fluctuation strength in the initial state, the decrease of α from central to peripheral collisions, indicates an increasing strength of fluctuations. On the other hand, the background shape of the system gets more elliptic in non-central Pb+Pb collisions, which is reflected in the observed growth of ε_0. Both trends are expected. For comparisons, the fluctuation strength and background shape in MC-Glauber and IP-Glasma are shown in Fig. 17 as shaded bands. Note that the extracted values of α and ε_0 from the experiementally measured v_2 distributions are not quite compatible with these effective models, upon the linear medium response.

The cubic order corrections to the linear response relations are normally tiny, but their effects are not negligible in the flow event-by-event fluctuations. Apparently, it changes the expected probability distribution of flow in Eq. (65), which introduces the cubic order response coefficient accordingly as an extra parameter. It is particularly important in the elliptic flow, for which during analysis we shall assume a constant ratio between cubic order response coefficient and the linear response coefficient, $\kappa'=\kappa_2'/\kappa_2\simeq0.1$, for all centralities. This constant ratio is an empirical assumption, but it is compatible with event-by-event hydro simulations, where κ' is roughly a constant around 0.2. We shall ignore effects from the cubic corrections in v_3. As expected, shown in Fig. 17, a cubic order correction reduces the value of the linear response coefficient. However, it does not significantly alter the centrality dependence of κ_2, nor the estimated value of η/s. A reduced linear response coefficient requires the system to have a larger eccentricity, and eccentricity fluctuations, to maintain the generated flow, which explains the observed decrease of α and

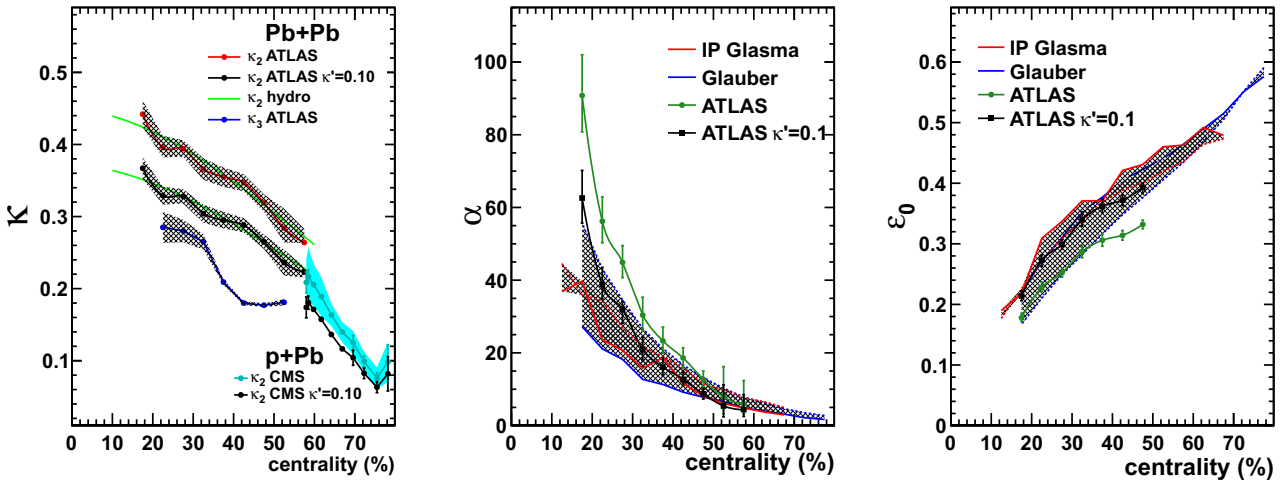

Fig. 17. (color online) Left panel: Extracted linear response coefficient κ_n from the fit of flow event-by-event distributions, with respect to the Pb+Pb collisions at $\sqrt{s_{\rm NN}}=2.76$ TeV, and p+Pb at $\sqrt{s_{\rm NN}}=5.02$ TeV. A corrected estimate of κ_2 is obtained accounting for an extra cubic order response in the relations (black points). Solid green lines are viscous hydro calculations of the linear response coefficient for Pb+Pb collisions, corresponding to $\eta/s=0.19$. Middle panel and the right panel: Extracted values of α and ε_0 from the fit of flow event-by-event distributions (green points). Corrected estimates accounting for a cubit order response are shown as well as black points. The extracted values are compared with initial state effective models, MC-Glauber (blue bands) and IP-Glasma (red bands). Figures adapted from Ref. [107] (DOI: https://doi.org/10.1016/j.physletb.2015.01.039), under the CC-BY-4.0 license (http://creativecommons.org/licenses/by/4.0/).

increase of ε_0. With the additional cubic order corrections, extracted values of α and ε_0 from experiments are compatible with MC-Glauber and IP-Glasma.

The ATLAS collaboration has also measured event-by-event distributions of the quadrangular flow magnitude v_4. One would expect the linear part of the flow, v_4^L, to be captured by a power law distribution, as it originates from pure initial state fluctuations, similar to v_3. However, since quadrangular flow contains strong nonlinear couplings of V_2, the probability distribution function of the whole magnitude, v_4, is supposed to be a particular convolution of the power and elliptic-power distributions.

Alternatively, the probability distribution $\mathbb{P}(v_n)$ can be quantitatively characterized by moments, or cumulants, of the corresponding harmonic flow v_n. Given the probability distribution function measured in experiments, the moment of harmonic flow $\langle\langle v_n^m\rangle\rangle$ can be calculated through the following integral

$$\langle\langle v_n^m\rangle\rangle=\int {\rm d}v_n\mathbb{P}(v_n)v_n^m. \tag{66}$$

Note that in realistic experiments, $\langle\langle v_n^m\rangle\rangle$ is often measured through an event average with a rapidity-gap to suppress non-flow contributions. Similarly, the cumulants of harmonic flow can be obtained in both methods in experiments, from the probability distribution function, or an average over collision events.

In either way, the obtained moments (or cumulants) of the harmonic flow can be used to analyze the underlying probability distribution function, according to Eq. (66). For instance, the mean $\langle\langle v_n\rangle\rangle$ and the second order moment, $\langle\langle v_n^2\rangle\rangle$ (or the second order cumulant $v_n\{2\}$), determine the variance of the distribution function. The third order and fourth order moments, $\langle\langle v_n^3\rangle\rangle$ and $\langle\langle v_n^4\rangle\rangle$, are related to the skewness and kurtosis of the distribution function, respectively. It should be emphasized that moments, or cumulants, of the flow, are very sensitive probes of the detailed structure of the distribution function. As a result, moments of flow harmonics lead to more accurate characterization than a direct fit of the event-by-event flow distribution.

3.1.2 Cumulants of harmonic flow

There are certain patterns of the flow cumulants observed in experiments, corresponding to the underlying properties of the probability distribution. These patterns quantitatively constrain the flow fluctuation behavior. For the convenience of discussion, we limit ourselves to the case of linear medium response, $v_n=\kappa_n\varepsilon_n$ (as in v_2 and v_3), so that the patterns in cumulants of flow harmonics are associated with those in the fluctuations of initial state eccentricities, through the scaled relation $\mathbb{P}(v_n)=\mathbb{P}(\kappa_n\varepsilon_n)/\kappa_n$. With respect to a specified probability distribution function, a cumulant of order m is

identified in the expansion of the cumulant generating function,

$$G(k_x,k_y)\equiv\ln\langle\langle\exp(\mathrm{i}k_xv_x+\mathrm{i}k_yv_y)\rangle\rangle$$
$$=\ln\int\mathrm{d}v_x\mathrm{d}v_y\mathbb{P}(v_x,v_y)\exp(\mathrm{i}k_xv_x+\mathrm{i}k_yv_y), \tag{67}$$

with respect to the k^m term.

A simple example is a Gaussian distribution, from which, except for the $v_n\{2\}$ being equal to a hydro linear response to the variance $v_n\{2\}=\kappa_n\sigma$, all higher order cumulants vanish,

$$v_n\{4\}=v_n\{6\}=v_n\{8\}=\ldots=0. \tag{68}$$

This is understandable, since the generating function of the cumulant contains only the second order term,

$$G(k_x,k_y)=G(k)=-\frac{1}{2}k^2(\kappa_n\sigma)^2. \tag{69}$$

In a similar way, for a Bessel-Gaussian distribution, the cumulant generating function is (after an integral over the relative angle in $\boldsymbol{k}$),

$$G(k)=-\frac{1}{2}k^2(\kappa_n\sigma)^2+\ln J_0(k\kappa_n\varepsilon_0) \tag{70}$$

The expected second order cumulant is $v_n\{2\}=\kappa_n\sqrt{\sigma^2+\varepsilon_0^2}$, while all higher order cumulants become degenerate,

$$v_n\{4\}=v_n\{6\}=v_n\{8\}=\ldots=\kappa_n\varepsilon_0. \tag{71}$$

The Bessel-Gaussian distribution is a good demonstration that the second order cumulant is separated from higher order ones, as long as fluctuations (described in terms of σ) play a significant role. The experimentally measured cumulants of elliptic flow from the CMS collaboration [108] are shown in Fig. 18, for the Pb+Pb collisions at $\sqrt{s_{\rm NN}}=2.76$ TeV (the left-hand panel), where one indeed observes the feature that $v_2\{2\}$ is separable from higher order ones, while higher order cumulants collapse. However, the pattern is not uniquely associated with a Bessel-Gausian distribution. In particular, the pattern can be expected in the power distribution and elliptic-power distribution. Moreover, one notices that the experimental measurements suggest an ordering in higher cumulants, although the differences in higher order cumulants are tiny,

$$v_2\{2\}>v_2\{4\}\gtrsim v_2\{6\}\gtrsim v_2\{8\}. \tag{72}$$

For the power distribution, all the values of cumulants are determined analytically via the single parameter α. With the help of the cumulant generating function, the second order cumulant is found to be

$$v_n\{2\}=\kappa_n/\sqrt{1+\alpha}, \tag{73}$$

while higher order ones are [54]

$$v_n\{4\}=\kappa_n\left[\frac{2}{(1+\alpha)^2(2+\alpha)}\right]^{1/4},$$
$$v_n\{6\}=\kappa_n\left[\frac{6}{(1+\alpha)^3(2+\alpha)(3+\alpha)}\right]^{1/6},$$
$$v_n\{8\}=\kappa_n\left[\frac{48(1+5\alpha/11)}{(1+\alpha)^4(2+\alpha)^2(3+\alpha)(4+\alpha)}\right]^{1/8}. \tag{74}$$

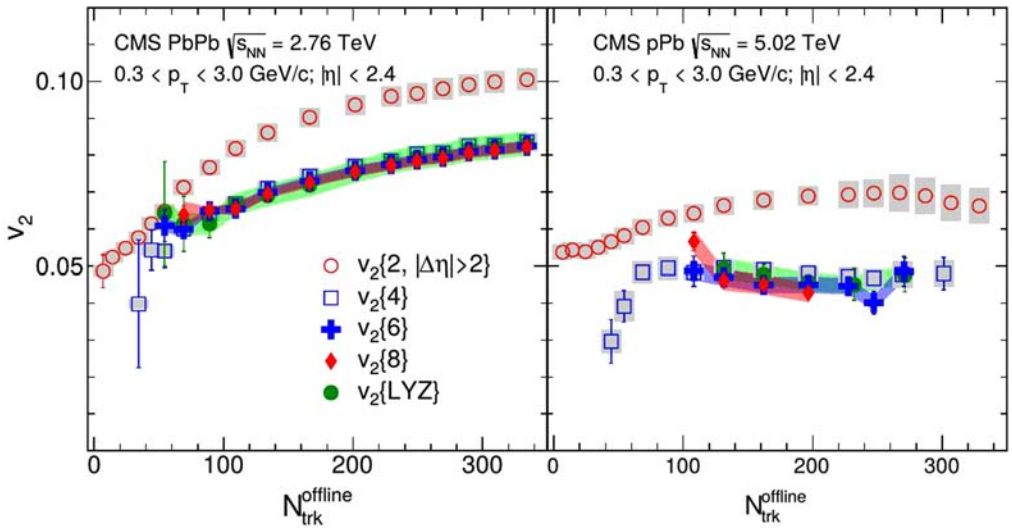

Fig. 18. (color online) Cumulants of elliptic flow v_2 are measured up to the 8th order in Pb+Pb collisions at $\sqrt{s_{\rm NN}}$ = 2.76 TeV and p+Pb collisions at $\sqrt{s_{\rm NN}}$ = 5.02 TeV in the same multiplicity range (in terms of number of offline tracks), from the CMS collaboration. Figure reproduced from Ref. [108] (DOI: https://doi.org/10.1103/PhysRevLett.115.012301, "Evidence for Collective Multiparticle Correlations in p-Pb Collisions"), under the CC-BY-3.0 license.

Note that the power distribution is derived assuming N independent sources on top of a two-dimensional Gaussian desnity profile with $\alpha=(N-1)/2$. Although in the large N limit, $N\gg 1$, one expects a strong ordering $v_n\{8\}\ll v_n\{6\}\ll v_n\{4\}\ll v_n\{2\}$. In the opposite limit of $N\to 1$, (limit that corresponds to the case of strong flow fluctuations), these cumulants converge: $v_n\{8\}\approx v_n\{6\}\approx v_n\{4\}\approx v_n\{2\}$. However, for practical N values corresponding to p+Pb collisions at the LHC energies, the gap between second order cumulant and higher order ones becomes sizable, and one finds similar relations $v_n\{8\}\lesssim v_n\{6\}\lesssim v_n\{4\}<v_n\{2\}$, in agreement with what was found in the p+Pb collisions (right-hand panel in Fig. 18). It is worth mentioning that, given these flow cumulants up to $v_2\{8\}$, the linear flow response coefficients κ_2 and the parameter α, can be solved according to Eq. (73) and Eq. (74). The corresponding results are shown in Fig. 17.

In the elliptic-power distribution, the additional parameter ε_0 that describes a mean eccentricity in the reaction-plane breaks azimuthal symmetry, and the derivation of cumulant generating function is complicated. Nevertheless, following the calculation of moments, the elliptic-power distribution leads to the analytical expression [55]

$$f_m\equiv\langle(1-v_n^2)^m\rangle=\frac{\alpha}{\alpha+m}(1-v_0^2)^m \times{}_2F_1\left(m+\frac{1}{2},m;\alpha+m+1;v_0^2\right), \quad (75)$$

where we assume $v_0=\kappa_n\varepsilon_0$ as the linear response to the mean eccentricity. Using this equation, one obtains from the standard definition of cumulants from moments,

$$\begin{aligned} v_n\{2\}&=(1-f_1)^{1/2}\\ v_n\{4\}&=(1-2f_1+2f_1^2-f_2)^{1/4}\\ v_n\{6\}&=\left(1+\frac{9}{2}f_1^2-3f_1^3+3f_1(\frac{3}{4}f_2-1)-\frac{3}{2}f_2-\frac{1}{4}f_3\right)^{1/6}. \end{aligned} \quad (76)$$

These are analytical expressions of cumulants obtained with respect to the elliptic-power distribution, as a function of parameters (ε_0,α). To demonstrate the ordering of cumulants, let us consider the limit of large α, $\alpha\gg 1$, but keeping $\alpha\varepsilon_0^2$ a constant (so that $\varepsilon_0^2\ll 1$ is a small variable). This is a plausible assumption regarding nucleus-nucleus collision events with small centrality percentile, because larger α corresponds to systems of a large number of independent sources, thus there are more central collisions. Similarly, treating ε_0 as a small quantity from the constant constraint of $\alpha\varepsilon_0^2$, implies a background of the collision system with a small ellipticity. Given these conditions, one is allowed to expand the expressions in Eqs. (76) in series of $1/\alpha$ and/or ε_0^2. Note that the expansion must be carried out simultaneously regarding $O(1/\alpha)\sim O(\varepsilon_0^2)$. To the leading order, one finds the ratios between cumulants,

$$\begin{aligned} \frac{v\{4\}}{v\{2\}}&=\sqrt{\frac{\alpha\varepsilon_0^2}{1+\alpha\varepsilon_0^2}}+\mathcal{O}\left(\frac{1}{\alpha}\right)\\ \frac{v\{6\}}{v\{4\}}&=1-\frac{1+\alpha\varepsilon_0^2}{2(\alpha\varepsilon_0^2)^2\alpha}+\mathcal{O}\left(\frac{1}{\alpha^2}\right)\\ \frac{v\{8\}}{v\{6\}}&=1-\frac{1}{22(\alpha\varepsilon_0^2)\alpha}+\mathcal{O}\left(\frac{1}{\alpha^2}\right), \end{aligned} \quad (77)$$

which reflect a similar ordering pattern as in Eq. (72) in this limit.

Actually, the tiny splitting in higher order cumulants predicted in the power and the elliptic-power distribution functions, and observed in experiments, is a generic feature of non-Gaussianity. It can be realized in effective models, such as MC-Glauber [109], where non-Gaussianity is introduced from the background shape, extra correlations among sources, etc.

Shown in Fig. 19 are the results of cumulant ratios of initial ellipticity from event-by-event simulations of MC-Glauber model (symbols), which, upon a linear hydro response, is identical to the cumulant ratios of elliptic flow v_2, e.g.,

$$\frac{v_2\{4\}}{v_2\{2\}}=\frac{\varepsilon_2\{4\}}{\varepsilon_2\{2\}},\quad \frac{v_2\{6\}}{v_2\{4\}}=\frac{\varepsilon_2\{6\}}{\varepsilon_2\{4\}} \quad (78)$$

The curves in Fig. 19 are parameterizations with an elliptic-power distribution. While the elliptic-power distribution gives a consistent estimate of the splitting between $v_2\{2\}$ and $v_2\{4\}$, it overestimates the gaps among $v_2\{4\}$, $v_2\{6\}$ and $v_2\{8\}$.

The success of the elliptic-power distribution in describing the cumulant ratios (at least up to the fourth order cumulant), comparing to the Bessel-Gaussian, is to large extent due to the fact that the initial state eccentricity is bounded by unity. The upper bound on the initial eccentricity induces a major source of the non-Gaussianity in the initial eccentricity fluctuations, and also in the event-by-event flow fluctuations. In particular, the upper bound on the ellipticity induces skewness of the v_2 fluctuations.

Using event-by-event hydro simulations of the Pb+Pb collisions in centrality class 50%-55%, the distribution of elliptic flow in- (v_x) and out-of- (v_y) the reaction-plane are shown as the histogram in Fig. 20. The magnitude of the flow is $v_2=\sqrt{v_x^2+v_y^2}$. Correspondingly, initial state event-by-event distributions of ε_x and ε_y scaled by a linear hydro response coefficient $\kappa=0.21$ are shown for comparisons. Note this linear response coefficient is a real quantity, which applies for both v_x and v_y. There are two characteristic properties of the non-Gaussian fluctuations associated with the v_2 distri-

bution, as one finds in Fig. 20. The first is reflected in the skewness. The two-dimensional distribution of $\mathcal{E}_2$ is symmetric under $v_y \leftrightarrow -v_y$, as required by parity. Thus one observes in Fig. 20 (a) the symmetric distribution of ε_y, leading to a symmetric distribution of v_y via linear hydro response. On the other hand, the distribution of ε_x is mostly found as positive, reflecting a non-zero mean $\langle\langle\varepsilon_x\rangle\rangle = \varepsilon_0$, and $\langle\langle v_x\rangle\rangle = v_0$. Together with the upper bound condition $\varepsilon_2 \leqslant 1$, the corresponding x-component of initial eccentricity ε_x is negatively skewed[1)] Upon a linear hydro response, negative skewness is achieved in the event-by-event distribution of v_x, seen as the comparison of histograms in Fig. 20 (b).

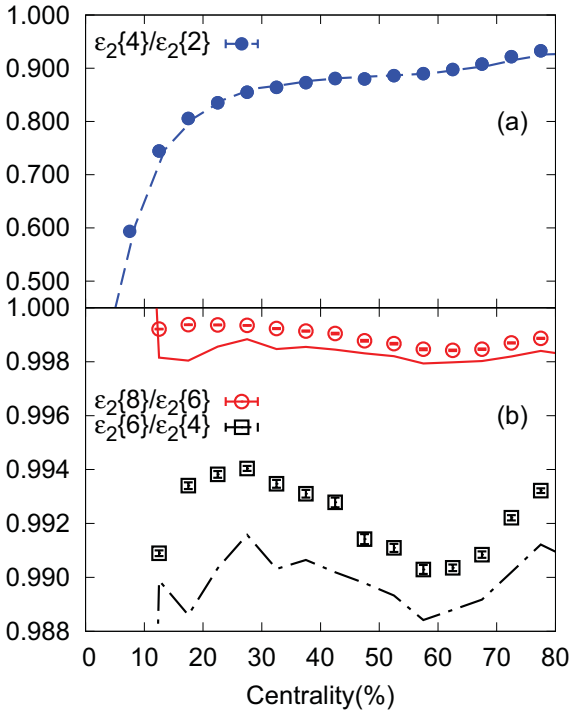

Fig. 19. (color online) Cumulant ratios of the elliptic anisotropy obtained from event-by-event simulations with MC-Glauber model, for the Pb+Pb collisions at $\sqrt{s_{\rm NN}}$ = 2.76 TeV. Lines of the same order correspond to paramterizations with elliptic-power distribution function. Reprinted figure with permission from L. Yan, J.-Y. Ollitrault, and A. M. Poskanzer, Phys. Rev. C 90, 024903, 2014 (DOI: https://doi.org/10.1103/PhysRevC.90.024903) (Ref. [55]). Copyright 2014 by the American Physical Society.

In addition to the skewness, one also observes from the simulations that the variance in the v_y distribution and the variance in the v_x distribution,

$$\sigma_y^2 \equiv \langle\langle v_y^2\rangle\rangle, \qquad \sigma_x^2 \equiv \langle\langle (v_x - v_0)^2\rangle\rangle \tag{79}$$

are not equal: $\sigma_y > \sigma_x$, another signature of non-Gaussian fluctuations.

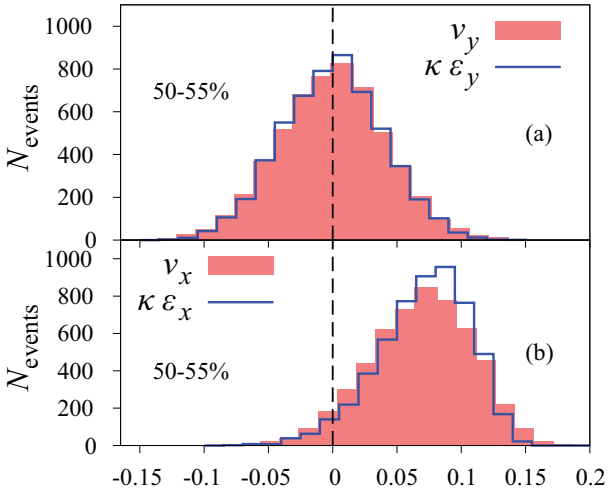

Fig. 20. (color online) Shaded area: Histograms of v_x (b) and v_y (a) event-by-event distributions from hydro simulations. Lines: Histograms of ε_x and ε_y distributions scaled by linear repsonse coefficient $\kappa = 0.21$. Reprinted figure with permission from G. Giacalone et al, Phys. Rev. C 95, 014913, 2017 (DOI: https://doi.org/10.1103/PhysRevC.95.014913) (Ref. [98]). Copyright 2017 by the American Physical Society.

To quantify skewness of the distribution via the non-zero third order moments, one needs the following non-zero third order moments

$$s_1 = \langle\langle (v_x - v_0)^3\rangle\rangle, \qquad s_2 = \langle\langle (v_x - v_0) v_y^2\rangle\rangle. \tag{80}$$

where $s_1 < 0$ describes the negatively skewed distribution of v_x. The skewness s_1 defines the standardized skewness

$$\gamma_1 \equiv \frac{s_1}{\sigma_x^3}. \tag{81}$$

Therefore, in terms of the non-Gaussian fluctuations characterized by $\sigma_y^2 - \sigma_x^2$, s_1 and s_2, the cumulants of flow are

$$\begin{aligned} v_2\{2\} &= \sqrt{v_0^2 + \sigma_x^2 + \sigma_y^2}, \\ v_2\{4\} &\simeq v_0 + \frac{\sigma_y^2 - \sigma_x^2}{2v_0} - \frac{s_1 + s_2}{v_0^2}, \\ v_2\{6\} &\simeq v_0 + \frac{\sigma_y^2 - \sigma_x^2}{2v_0} - \frac{\frac{2}{3}s_1 + s_2}{v_0^2}, \\ v_2\{8\} &\simeq v_0 + \frac{\sigma_y^2 - \sigma_x^2}{2v_0} - \frac{\frac{7}{11}s_1 + s_2}{v_0^2}, \end{aligned} \tag{82}$$

1) The convention of negative skewness of a distribution is reflected as the distribution being concentrated on the right side, while positive skewness corresponds to a left-side concentrated distribution.

where higher order cumulants are expanded in powers of fluctuations. The present analysis focuses on the dominant source of non-Gaussian fluctuations in the elliptic anistotropy, assuming a linear hydro response. Accounting for these fundamental concepts in the flow paradigm, the derived results in Eqs. (82) provide a very simple interpretation of the fine splitting structures in higher order cumulants of v_2: the splitting in higher order cumulants is solely generated by skewness s_1. It then allows one to get some interesting findings. Especially, with respect to the fact that the splittings in cumulants are analytically related to the skewness up to the leading order in the expansion of fluctuations, one expects the differences

$$\begin{aligned} v_2\{4\}-v_2\{6\}&=-\frac{s_1}{3v_0^2},\\ v_2\{6\}-v_2\{8\}&=-\frac{s_1}{33v_0^2}, \end{aligned} \tag{83}$$

or equivalently [98, 110],

$$v_2\{6\}-v_2\{8\}=\frac{1}{11}(v_2\{4\}-v_2\{6\}). \tag{84}$$

The skewness of v_2 is present only in the distribution of v_x, which is not approachable in experiment on an event-by-event basis. However, since s_1 is related to the splitting of higher order cumulants of v_2, under the assumption that fluctuations are sub-dominant, one finds the standardized skewness Eq. (81) approximates to the following quantity $\gamma_1^{\rm exp}$,

$$\gamma_1\approx\gamma_1^{\rm exp}\equiv-6\sqrt{2}v_2\{4\}^2\frac{v_2\{4\}-v_2\{6\}}{(v_2\{2\}^2-v_2\{4\}^2)^{3/2}}. \tag{85}$$

Eq. (85) can be verified in event-by-event hydro simulations. Shown in the left-hand panel of Fig. 20 are the skewness results calculated from hydrodynamics with respect to Pb+Pb collisions at $\sqrt{s_{\rm NN}}=2.76$ TeV, given a constant $\eta/s=0.08$, as a function of centrality. The simulations are initialized via the MC-Glauber model, from which the standardized skewness of initial eccenticity ε_x, γ_1^{ε} is obtained (blue points), according to Eq. (81) but with a replacement of v_x by ε_x in calculating s_1 and σ_x. The open symbols in the left-hand panel of Fig. 21 correspond to the exact predictions of the standardized skewness from hydrodynamics following Eq. (81), while the shaded band is obtained with respect to the approximated estimate from Eq. (85), in terms of flow cumulants. The agreement between γ_1 and $\gamma_1^{\rm exp}$ is remarkable, up to 60% of centrality, where flow fluctuations are significant that the assumption applied in Eq. (85) breaks down. Hydro predicted $\gamma_1^{\rm exp}$ of v_2 is compatible with the experimental results from the ATLAS collaboration, as can be seen in the comparison in the right-hand panel of Fig. 21. Recently the CMS collaboration has extended the measurements of the standard skewness to $\sqrt{s_{\rm NN}}=5.02$ TeV [106].

In the case of the absolute linear medium response, the effects of medium dynamics drop out of the definition of the standardized skewness, hence one may identify γ_1 with γ_1^{ε}. However, Fig. 20 displays sizable deviation between γ_1 and γ_1^{ε} in collisions of centrality greater than 30%, indicating the role of the nonlinear medium response. Actually, one observes $|\gamma_1|<|\gamma_1^{\varepsilon}|$, which means that medium dynamics from hydro washes out the skewness of initial eccentricity fluctuations, so that the generated v_2 distribution is less skewed. This effect is mostly due to the cubic order response in v_2, which gets stronger as centrality grows, in line with the trend observed in Fig. 20.

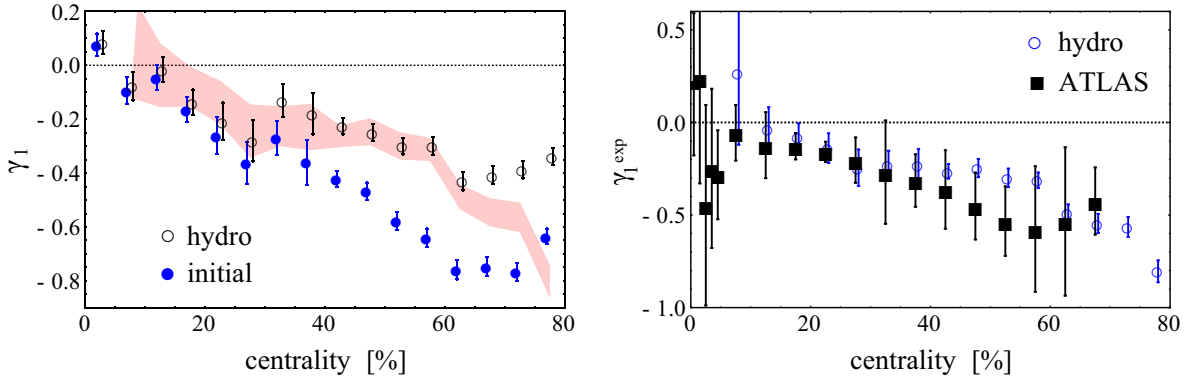

Fig. 21. (color online) Left: The standardized skewness of elliptic anisotropy from event-by-event hydro simulations with respect to Pb+Pb collisions of $\sqrt{s_{\rm NN}}=2.76$ TeV. Symbols correspond to the results calculated according to Eq. (81) for the initial ellipticity (blue points) and v_2 (open symbols). The shaded band corresponds to $\gamma_1^{\rm exp}$, obtained following Eq. (85). Right: Comparison of hydro predictions on $\gamma_1^{\rm exp}$ to experimental results from the ATLAS collaboration. Reprinted figure with permission from J. Noronha-Hostler et al, Phys. Rev. C 93, 014909, 2016 (DOI: https://doi.org/10.1103/PhysRevC.93.014909) (Ref. [21]). Copyright 2016 by the American Physical Society.

In addition to the corrections from cubic order response to the fluctuations of v_2, the effects beyond the linear medium response are more pronounced in the higher flow harmonics. For instance, the quadrangular flow v_4 has a negative value of $v_4\{4\}^4$ found in non-central collisions in experiments [111], which has a natural origin from the nonlinear couplings of v_2^2, as $2\langle\langle v_2^4\rangle\rangle^2-\langle\langle v_2^8\rangle\rangle$ [112].

3.2 Correlations among harmonic flow

In experiments, the flow fluctuations measure the fluctuating properties of flow magnitude v_n, by correlating flow of the same harmonic orders. Correlations of harmonic flow involving mixed harmonic orders, on the other hand, reflect the correlation nature of flow magnitude v_n and phase Ψ_n. In experiments, there have been several types of correlators investigated so far, which we discuss within the context of the flow paradigm.

The event-plane correlators. At first, the event-plane correlators, measured by the ATLAS collaboration, were designed to detect the correlations among phases of different flow harmonics, on an event-by-event basis. It was later realized that event plane correlators also involve contributions through the correlated flow magnitudes. In practice, there exists subtle difference in the definitions of event-plane correlators owing to the issues of detector resolution [113]. In the present discussion, we take the definition of event-plane correlators using the Pearson correlation coefficient, although the original results obtained by the ATLAS collaboration using the scalar-product method are slightly different, under some circumstances. For instance, for the correlation V_4 and V_2 one defines,

$$\rho_{24}=\frac{\mathrm{Re}\langle\langle V_4^*V_2^2\rangle\rangle}{\sqrt{\langle\langle v_4^2\rangle\rangle\langle\langle v_2^4\rangle\rangle}}=\langle\langle\cos4(\Psi_2-\Psi_4)\rangle\rangle_w, \tag{86}$$

which is identical to the ATLAS measured event-plane correlator between Ψ_2 and Ψ_4. The notation $\langle\langle\rangle\rangle_w$, following Ref. [100], denotes the measured event-plane correlations with the scalar-product method. The Pearson correlation coefficient has a clear physical interpretation, quantifying the correlation strength between the *complex* quantities V_2^2 and V_4. It is thus clear that correlation between magnitudes also contributes to ρ_{24}.

For mixings among more than two harmonic orders, the Pearson correlation coefficient definition differs slightly from event-plane correlations measured by the scalar product method. For instance, the correlation among V_2, V_3 and V_5 is

$$\rho_{235}=\frac{\mathrm{Re}\langle\langle V_5^*V_2V_3\rangle\rangle}{\sqrt{\langle\langle v_5^2\rangle\rangle\langle\langle v_2^2v_3^2\rangle\rangle}}, \tag{87a}$$

$$\langle\langle\cos(2\Psi_2+3\Psi_3-5\Psi_5)\rangle\rangle_w=\frac{\mathrm{Re}\langle\langle V_5^*V_2V_3\rangle\rangle}{\sqrt{\langle\langle v_5^2\rangle\rangle\langle\langle v_2^2\rangle\rangle\langle\langle v_3^2\rangle\rangle}}. \tag{87b}$$

Note that the deviation comes from correlation between v_2 and v_3, $\langle\langle v_2^2v_3^2\rangle\rangle\neq\langle\langle v_2^2\rangle\rangle\langle\langle v_3^2\rangle\rangle$. The absolute value of the Pearson correlation coefficient is strictly constrained between 0 and 1, with 1 corresponding to absolute (anti)-correlation, while 0 indicates the case with no correlation at all. Event-plane correlators among flow harmonics have been measured at the LHC energy involving V_2, V_3, V_4, V_5 and V_6 (see Fig. 15).

With the characterization of flow harmonics in terms of the medium response to initial geometrical properties, one can understand the event-plane correlations in the flow paradigm. For the convenience of discussion, we take the correlation between V_2 and V_4 as an example. Recalling that $V_4=\kappa_4\mathcal{E}_4+\chi_{422}V_2^2+\delta_4$, it is not difficult to recognize that the Pearson coefficient reaches unity (absolute correlation) once the linear medium response $\kappa_4\mathcal{E}_4$ and residual δ_4 in V_4 are neglected, namely, V_4 is linearly dependent on V_2^2. On the other hand, if one considers only the generation of V_4 from linear flow response to an initial eccentricity $\mathcal{E}_4$, the resulting correlation is

$$\rho_{24}=\frac{\mathrm{Re}\langle\langle\mathcal{E}_4^*\mathcal{E}_2^2\rangle\rangle}{\sqrt{\langle\langle\varepsilon_4^2\rangle\rangle\langle\langle\varepsilon_2^4\rangle\rangle}}=\langle\langle\cos4(\Phi_2-\Phi_4)\rangle\rangle_w. \tag{88}$$

Namely, the event-plane correlation is identical to the participant-plane correlation. Since the realistic flow generation interpolates between linear response and nonlinear mode couplings, the expected event-plane correlation would be between these two extreme scenarios.

Figure 22 illustrates the expected event-plane correlation ρ_{24}, between the linear and nonlinear dominated extreme scenarios. There are two lines corresponding to the case generated by linear flow response, considering initial state fourth order eccentricity characterized in terms of moments or cumulants. Since the relative contribution of linear flow response to V_4 decreases as centrality grows, the correlation ρ_{24} gets stronger towards peripheral collisions. Similarly, it is understandable that when there are larger dissipations in the medium, the linear medium response gets more damped than the nonlinear mode couplings, and the induced correlation ρ_{24} should be stronger. A similar strategy has been generalized to all the observed event-plane correlators from the ATLAS collaboration, which leads to successful estimates, except $\langle\langle\cos(2\Psi_2+4\Psi_4-6\Psi_6)\rangle\rangle$ [114].

It should be noted that the correlation Eq. (86) measured in experiments involves three-particle correlations (in the numerator), and the rms value of v_4 and fourth order moment of elliptic flow (in the denominator). The correlation feature of the mixed harmonics is entirely captured in the three-particle correlations in the numerator, while the denominator in Eq. (86) plays a role of normalization. Direct measurements of the numerator can be carried out in three-particle correlations, which

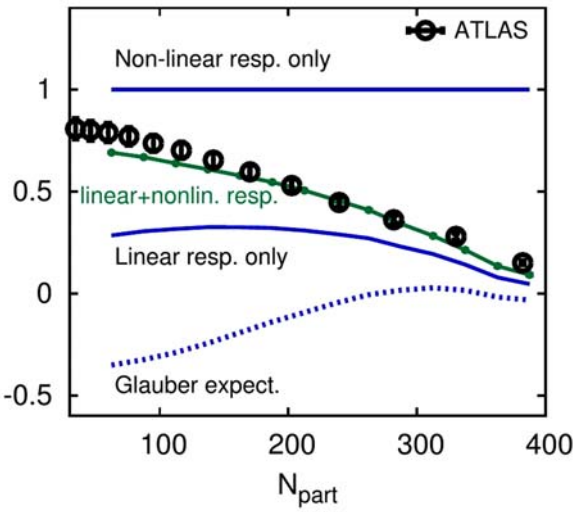

Fig. 22. (color online) The event-plane correlator ρ_{24} measured by the ATLAS collaboration, with respect to Pb+Pb at $\sqrt{s_{\rm NN}}$ = 2.76 TeV. The blue lines are those expected from the medium response scenarios, when linear or nonlinear part of the quadrangular flow dominates, respectively. Hydro prediction with $\eta/s = 1/4\pi$ interpolating the two scenarios is shown as the green solid line. Reprinted figure with permission from D. Teaney and L. Yan, Phys. Rev. C 90, 024902, 2014 (DOI: https://doi.org/10.1103/PhysRevC.90.024902) (Ref. [114]). Copyright 2014 by the American Physical Society.

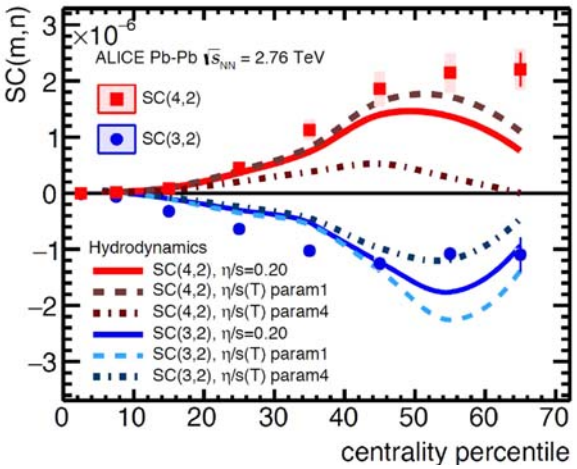

Fig. 23. (color online) Symbols correspond to the symmetric cumulants $SC(4,2)$ (red) and $SC(3,2)$ (blue) measured by the ALICE collaboration. Lines of different types are hydrodynamic predictions with various parameterizations of η/s. Figure reproduced from Ref. [115] (DOI: http://dx.doi.org/10.1016/j.nuclphysa.2017.04.016), under the CC-BY-4.0 license (http:// creativecommons.org/licenses/by/4.0/).

was done recently by the STAR collaboration [102, 103],

$$C_{m,n,m+n} \equiv {\rm Re}\langle\langle {\rm e}^{{\rm i}m\phi_p^1+{\rm i}n\phi_p^2-{\rm i}(m+n)\phi_p^3}\rangle\rangle \sim {\rm Re}\langle\langle V_m V_n V_{m+n}^*\rangle\rangle. \tag{89}$$

Despite the difference in magnitudes obtained in the three-particle correlations comparing to the event-plane correlators (for obvious reasons), the signs of the correlations agree in these measurements, as expected. It is worth mentioning that some particular correlations involving dipolar flow V_1 get extra contributions from the condition of moment conservation, such as C_{112}. It is interesting to notice from the STAR measurements that a positive C_{123} is observed, which implies that in V_3 there is a nonlinear coupling of modes between V_1 and V_2.

Symmetric cumulants $SC(m,n)$ One difficulty in the measurement of flow is the subtraction of non-flow contributions. Non-flow effects also present in the event-plane correlators, as expected since there are moments involved in the definition of event-plane correlators, e.g. in Eq. (86) and Eq. (87). To subtract non-flow effects, analogous to the cumulants of flow which suppress non-flow by construction, the correlations among mixed flow harmonics can be studied in the so-called symmetric cumulants [101, 116].

$$SC(m,n) = \langle\langle v_n^2 v_m^2\rangle\rangle - \langle\langle v_n^2\rangle\rangle\langle\langle v_m^2\rangle\rangle \tag{90}$$

where $m \neq n$ refers to different harmonic orders. As expected in a cumulant, self-correlations are subtracted in the definition, and so are non-flow contributions. Apparently, the symmetric cumulant vanishes once there is no correlation between v_n and v_m. Although the definition of symmetric cumulant relies only on correlations of flow magnitudes, symmetric cumulant gets contributions from the correlation of flow phases. In Fig. 23, symmetric cumulants are measured and shown with mixings between V_2 and V_3, and V_2 and V_4. Both of the observed symmetric cumulants present a trend of increasing correlation strength towards large centrality percentiles. The correlation between V_2 and V_3 is negative, while it is positive between V_2 and V_4, consistent with what was observed in the event-plane correlators. The correlation magnitude and trend are captured by the corresponding hydrodynamic simulations with specified values of η/s.

Following the same strategy, the observed correlation patterns in the symmetric cumulants can be understood in terms of flow response. Before proceeding, we define the normalized symmetric cumulant [101],

$$sc(m,n) = \frac{SC(m,n)}{\langle\langle v_m^2\rangle\rangle\langle\langle v_n^2\rangle\rangle}. \tag{91}$$

Eq. (91) captures the same correlation behavior as in Eq. (90), but it is normalized by taking a ratio with respect to $\langle\langle v_m^2\rangle\rangle\langle\langle v_n^2\rangle\rangle$. One advantage of the normalized symmetric cumulant is, statistical errors of the measured

event-averaged quantities cancel out in the ratio to some extent. Again, let us take the correlation between V_2 and V_4 as an example. Substituting the response relation of V_4 in $sc(2,4)$, one realizes the relation

$$sc(2,4)=\left(\frac{\langle\langle v_2^6\rangle\rangle}{\langle\langle v_2^2\rangle\rangle\langle\langle v_2^4\rangle\rangle}-1\right)\rho_{24}^2. \tag{92}$$

According to Eq. (92), the normalized symmetric cumulant is factorized into a factor that records the fluctuation property of v_2 (in terms of ratios of moments) and the event-plane correlator ρ_{24}, both of which are measurables in experiments. Since the underlying assumption behind Eq. (92) is the flow response relation in the flow paradigm, the validity of Eq. (92) provides an ideal test of the flow paradigm we have been discussing so far.

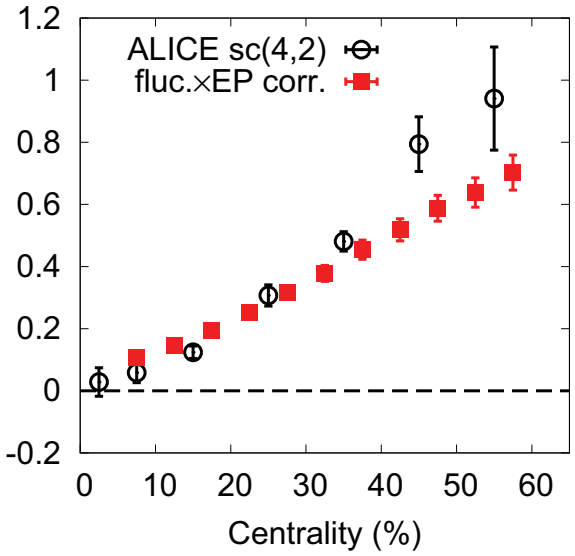

Fig. 24. (color online) A comparison between the normalized symmetric cumulant $sc(4,2)$ (open symbols) and the factorization relation Eq. (92) (red points). Reprinted figure with permission from G. Giacalone et al, Phys. Rev. C 94, 014906, 2016 (DOI: https://doi.org/10.1103/PhysRevC.94.014906) (Ref. [117]). Copyright 2016 by the American Physical Society.

By taking both the fluctuations of v_2 and event-plane correlators from experimental results, Fig. 24 depicts the comparison of the normalized symmetric cumulant $sc(2,4)$ and the factorization relation in Eq. (92). Although the v_2 fluctuations and event-plane correlator results are adopted from the ATLAS collaboration, which has different acceptances in transverse momentum $p_{\rm T}$ and pseudo-rapidity η compared to ALICE, quantitative agreement is achieved in Fig. 24. Let us emphasize again that the comparison made in Fig. 24 does not involve any hydro simulations with respect to particular parameterizations, but it manifests the success of the flow paradigm.

4 Flow paradigm in small colliding systems

In general, small colliding systems, such as p+Pb, are considered in heavy-ion experiments as a baseline of the nucleus-nucleus collisions, where the generated system is *not* recognized as thermalized. Therefore, techniques of perturbative calculations based on QCD dynamics can be applied for theoretical predictions. The observed correlation patterns in small colliding systems are accordingly expected to be distinguished from those induced by the medium collective expansion in nucleus-nucleus collisions. However, long-range multi-particle correlations were observed in the recent experiments at RHIC and the LHC energies, in the very high multiplicity events of the small colliding systems: p+Pb [88, 99, 99, 108, 118–122], d+Au [123], He^3+Au [124] and even p+p [87, 125]. These long-range correlation patterns lead to similar measurements of flow harmonics, and fluctuations and correlations of these flow. These flow observables are comparable to the results found in nucleus-nucleus collisions on a general ground. Besides, long-range correlations in small colliding systems can be quantitatively measured. The measured harmonic flow in small colliding systems can be captured by hydrodynamic simulations [30, 126–132], provided the geometrical information of the initial states is incorporated properly.

Based on the observed long-range multi-particle correlation patterns and successful applications of hydrodynamics, it appears tempting to generalize the flow paradigm in the small colliding systems, so that the observed flow harmonics can be similarly understood as fluid response to the initial state geometrical properties of these systems. However, there are issues that makes a straightforward generalization questionable. In this section, after summarizing some of the experimental observations related to the phenomenon of medium collective expansion in small colliding systems, in comparison with the results from hydrodynamic simulations and qualitative (or quantitative) estimate from the idea of the flow paradigm, we discuss some challenges in the theoretical aspect of applying hydrodynamics in small colliding systems.

4.1 Collectivity in small colliding systems

Application of the flow paradigm to small colliding systems requires medium collective expansion. There has been evidence collected from various measurements of the flow harmonics in experiments at RHIC and the LHC energies that supports a medium collective expansion scenario in the small colliding systems. Apart from experiments, theoretical calculations with viscous hydrodynamics with a proper initialization, or AMPT model [133], also reproduce to a quantitative level the

flow observables, emphasizing the role of late stage evolution in the formation of the observed long-range correlations. With the help of the medium response relations established in the flow paradigm based on previous studies of nucleus-nucleus collisions, these observed correlation signatures in small colliding systems can be understood consistently.

4.1.1 Experimental evidence

As we have learned from analyses in nucleus-nucleus collisions, the medium collective expansion of a colliding system results in long-range correlation in rapidity, which is recognized as the "ridge" at $\Delta\phi$=0 and at large relative rapidity in the two-particle correlation function. The non-zero "ridge" leads to the measured harmonic flow in the Fourier decomposition of the two-particle correlation function. Fig. 25 displays the two-particle correlation function measured in p+Pb collisions, at $\sqrt{s_{\rm NN}}$=5.02 TeV, by the CMS collaboration [118]. In collision events with low multiplicity productions, as shown in Fig. 25 (a), there is no such long-range structure observed, consistent with the traditional understanding of p+Pb collisions. Quite differently, the "ridge" becomes obvious in the two-particle correlation function in high multiplicity events, shown in Fig. 25 (b).

Actually, Fig. 25 reveals an interesting trend that the observed long-range correlation patterns exhibit only in events with sufficiently high multiplicity productions, in the small colliding systems. Indeed, similar behavior of the long-range azimuthal correlations is confirmed in measurements with respect to d+Au [123], He^3+Au [124] at RHIC, and also p+p collisions at the LHC energies [119, 125]. It is also realized that the fourth power of the four-particle cumulant of elliptic flow $v_2\{4\}^4$ from p+Pb collisions changes sign as multiplicity decreases [88, 119, 125]. The role of high multiplicity productions in the flow paradigm implies high energy/entropy density of the created medium, which is necessary for the collective evolution according to fluid dynamics. Observing the long-range correlation patterns in high multiplicity events is already an indication that the system evolution in small colliding systems is compatible to what one would expect in a flow paradigm.

Along the same line of analysis, two-particle correlation functions can be decomposed into Fourier harmonics to extract harmonic flow, which gives the flow of two-particle cumulant $v_n\{2\}$. To further investigate and identify the effect of medium collective expansion, flow harmonics are expected as well from multi-particle correlations. The measured cumulant of elliptic flow in the p+Pb system can be found in the right-hand panel of Fig. 18, by the CMS collaboration [108]. It is evident from the flow cumulants that the measured elliptic anisotropy presents, in up to eight-particle correlations, which strongly supports the idea of medium collectivity.

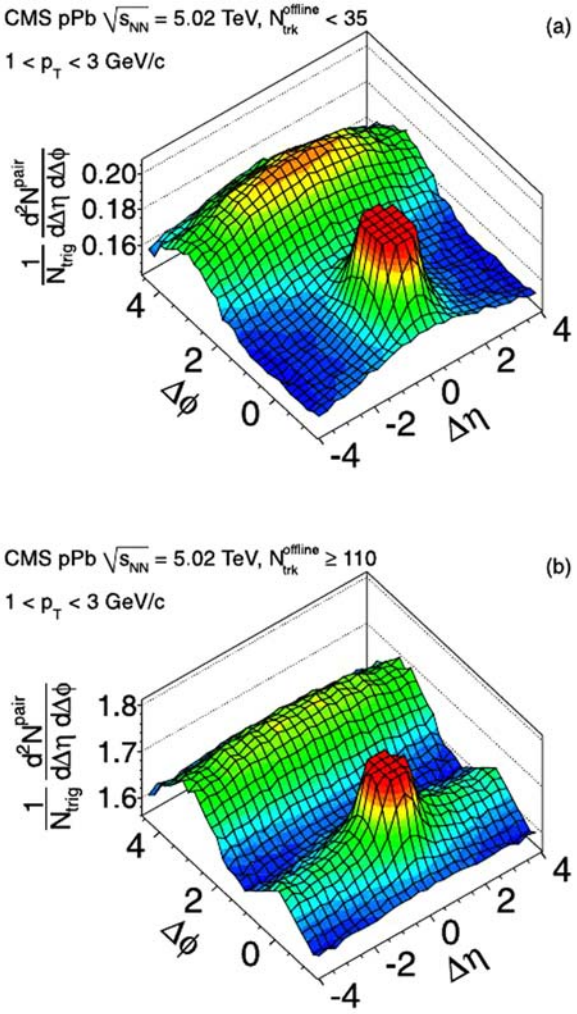

Fig. 25. (color online) Two-particle correlation function of the p+Pb colliding system at $\sqrt{s_{\rm NN}}$= 5.02 TeV, for the (a) low and (b) high multiplicity production events, measured by the CMS collaboration. Figure reproduced from Ref. [118] (DOI: https://doi.org/ 10.1016/j.physletb.2012.11.025), under the CC-BY-NC-ND license.

In addition to these *qualitative* agreements with the medium collective expansion, there is also evidence that is *quantitatively* consistent with the flow paradigm estimate. Compared to the flow multi-particle cumulants in Pb+Pb collisions, one observes similar hierarchy ordering from $v_2\{2\}$ to higher order cumulants as in Eq. (72), $v_2\{2\} > v_2\{4\} \gtrsim v_2\{6\} \gtrsim v_2\{8\}$, which implies similar non-Gaussian properties of flow fluctuations. Following the analysis in the flow paradigm, we understand the ordering in flow cumulants as an indication of non-Gaussianity, especially, the non-Gaussianity in the initial state ellipticity fluctuations, upon a linear fluid response. In a p+Pb colliding system, the background of the initial state geometry is dominated by the shape of the

proton, which is approximately spherical. The elliptic eccentricity in p+Pb is purely fluctuation-driven, and its event-by-event fluctuations can be described by a power distribution function, Eq. (24).

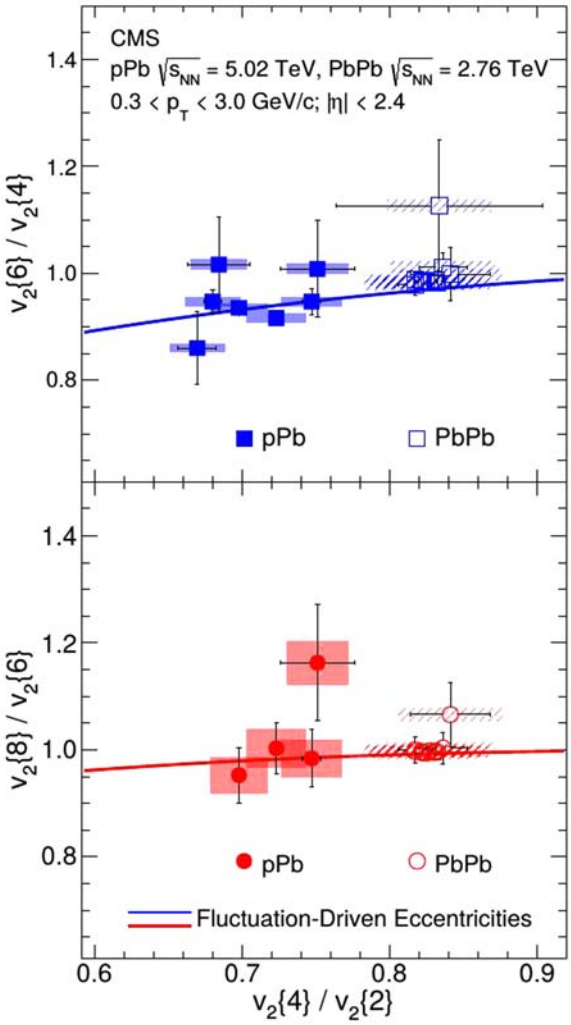

Fig. 26. (color online) Relations betweeen cumulant ratios measured by the CMS collaboration, for the p+Pb collisions at $\sqrt{s_{\rm NN}}$ = 5.02 TeV and Pb+Pb collisions at $\sqrt{s_{\rm NN}}$ = 2.76 TeV. Solid lines are expected analytical relations in the flow paradigm, in terms of the power distribution. Figure reproduced from Ref. [108] (DOI: https://doi.org/10.1103/PhysRevLett.115.012301, "Evidence for Collective Multiparticle Correlations in p-Pb Collisions"), under the CC-BY 3.0 license.

The power distribution allows one to relate the ratio between flow cumulants analytically. Fig. 26 shows the measured ratios of the cumulants of the elliptic flow in p+Pb collisions and Pb+Pb collisions by the CMS collaboration [108]. Solid lines correspond to the expectations from the power distribution, which are compatible with the measured data of p+Pb collisions within systematic and statistical uncertainties. This comparison provides quantitative evidence for the collectivity expansion in the high multiplicity events of p+Pb collisions.

Recently, similar analyses with respect to the flow cumulant were carried out by the ATLAS collaboration [121, 122], and extended to the high multiplicity events in p+p collisions. Given the observed hierarchy of the flow cumulants, the analytical description using the power distribution function determines an effective number of independent sources. It is interesting to notice that the extracted number of independent sources by the ATLAS collaboration are compatible for p+p and p+Pb collisions, provided the multiplicity productions in these systems are comparable. It is worth mentioning that this observation is consistent with some theoretical analyses based on hydrodynamics, which suggest that the system multiplicity plays a dominant role in collective evolution, rather than the system size [26, 134, 135].

In addition to the flow cumulants of v_2, there are other signatures related to flow harmonics that are captured in the flow paradigm. For instance, the differential spectrum of elliptic flow of identified particles in the small colliding systems present mass ordering [120, 123], i.e., the anisotropic momentum spectra of heavier particles get pushed towards larger transverse momentum owing to the radial flow [136], an interesting feature anticipated due to the conversion to particles from fluid excitations, although it should be noted that mass ordering is *not* an ad hoc feature characterized in hydro modelings [137]. Besides, the measured flow observables in small systems also include triangular flow v_3 [122, 124], quadrangular flow v_4 [122], and correlations of these flow observables in terms of symmetric cumulants [119]. These observables are compatible with the flow paradigm expectations as well. For instance, it is noticeable that in the small systems, that the hierarchy of anisotropic flow exists from lower to higher order harmonic orders. The sign of the measured symmetric cumulant, e.g., $SC(2,3) < 0$, agrees with the expected correlation pattern induced by initial state geometry [61].

4.1.2 Results from hydrodynamic simulations

When solving viscous hydrodynamics with respect to small colliding systems, the essential adjustments are in the effective descriptions of initial state, compared to the hydro simulations with respect to nucleus-nucleus collisions. Especially, one should be cautious about potential contributions from effects of small scales, e.g., subnucleon structures. For high multiplicity events in the light-heavy colliding systems, the background geometry of the created system is to a large extent determined by the configuration of the light nucleus, such as a proton, deuteron, or He^3. Additionally, the resulting initial state density profile after nucleon-nucleon collisions

is affected by details of energy deposition. Taking these factors into account on various grounds makes hydro predictions strongly model-dependent. For instance, it was realized that the IP-Glasma realization without intrinsic proton shape deformation under-predicts the observed elliptic flow in p+Pb collisions [132].

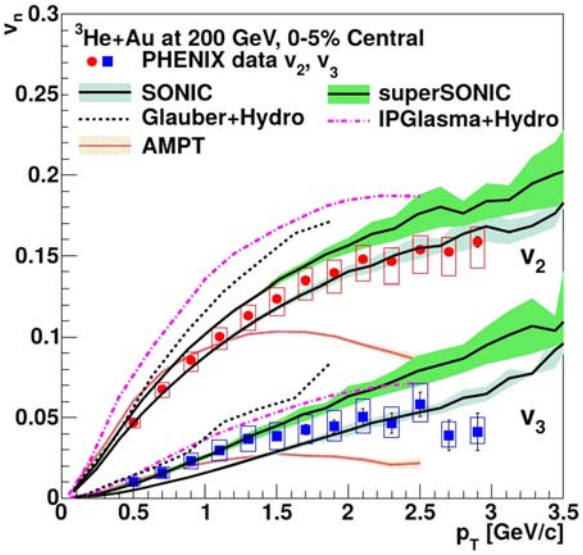

Fig. 27. (color online) Symbols: Elliptic flow v_2 and triangular flow v_3 measured in He^3+Au collisions at $\sqrt{s_{\rm NN}}$=200 MeV, by the PHENIX collaboration. Lines: Results from hydrodynamic simulations and AMPT. Reprinted figure with permission from A. Adare et al (PHENIX Collaboration), Phys. Rev. Lett. 115, 142301, 2015 (DOI: https://doi.org/10.1103/PhysRevLett.115.142301) (Ref. [124]). Copyright 2015 by the American Physical Society.

Nevertheless, an overall agreement of predictions from hydro modelings of small colliding systems and experimentally measured flow harmonics is achieved.

As an example, Fig. 27 presents the measured elliptic flow and triangular flow in the He^3+Au collisions, at the RHIC energy $\sqrt{s_{\rm NN}} = 200$ MeV [124]. Note that there is an intrinsic triangular asymmetry of the colliding system, determined by the configuration of He^3. Model calculations based on viscous hydrodynamics, or transport model [133], are shown as lines of different types. For the He^3 system, intrinsic geometry is dominated by the the three nucleons, not the detailed geometrical configuration of the proton. Thereby, with the effective modelings of initial state by the MC-Glauber model [128] or IP-Glasma [138], hydrodynamic simulations with η/s equal or close to $1/4\pi$ lead to compatible results of v_2 and v_3, although the results over-predict in comparison with experiment. The over-predictions can be remedied in the hydro calculations with larger dissipative corrections. In an alternative approach [130], hydro results from Glauber+SONIC coupled to hadron transport calculations, which effectively introduces extra sources of medium dissipations, do lead to reasonable predictions, in spite of the fact that the initial state is modeled with a similar MC Glauber. When fluid velocity in the initial state is assumed, the flow harmonics from hydro predictions are enhanced, as seen in the results from superSONIC simulations [139] in Fig. 27.

To further examine the response relations in a flow paradigm, we look at the simulated results from Glauber+SONIC simulations [130] for different colliding systems. Shown in Fig. 28 is a scatter plot of the ratio of elliptic flow magnitude at $p_{\rm T}$=1 GeV to the initial eccentricity, v_2/ε_2, as a function of ε_2, from p+Au (black), d+Au (red) and He^3+Au (blue) collision events. Freeze-out temperatures are used to control the life-time of hydro evolution during system expansion. The left-hand figure in Fig. 28 has a T_{fo} = 170 MeV, while the right-hand one is obtained with T_{fo}=150 MeV. Each point in the figure corresponds to one single event. A constant value in the plots indicates a linear flow response relation between v_2 and ε_2, which is observed in the three colliding systems, except in d+Au with a sufficiently large ε_2. The breaking of linear response relation in d+Au is understood as follows: at very large ε_2, the initial density profile is composited by two separated hotspots, which hardly merge during expansion at later stages of the medium evolution, leading to a very small value of v_2. Apart from the discrepancy in d+Au of large ε_2, the linear response relations of elliptic flow are valid in the hydro simulations of small colliding systems.

4.2 Challenges of the flow paradigm

This section is devoted to a discussion on challenges in the flow paradigm, from the *theoretical* aspect. The discussion is on a more general ground with respect to all the colliding systems in heavy-ion experiments, albeit the situation is obviously more serious in small colliding systems. It should be emphasized that, so far, there have not been strong violations of the expected features from the flow paradigm observed in *experiments*, from large colliding systems of Au+Au, Pb+Pb, to the recent measurements in small systems, p+Pb, d+Au and He^3+Au. The discussion will not be conclusive, but give a somewhat brief description of the recent developments in the theory of hydrodynamics beyond local thermal equilibrium.

The flow paradigm is quite well-established in large colliding systems, where the observed long-range multi-particle correlation patterns are understandable as a consequence of medium response to initial state geometry. In small colliding systems, although the system size decreases dramatically (roughly by a factor of 10), hydro modelings provide reasonable characterizations of the

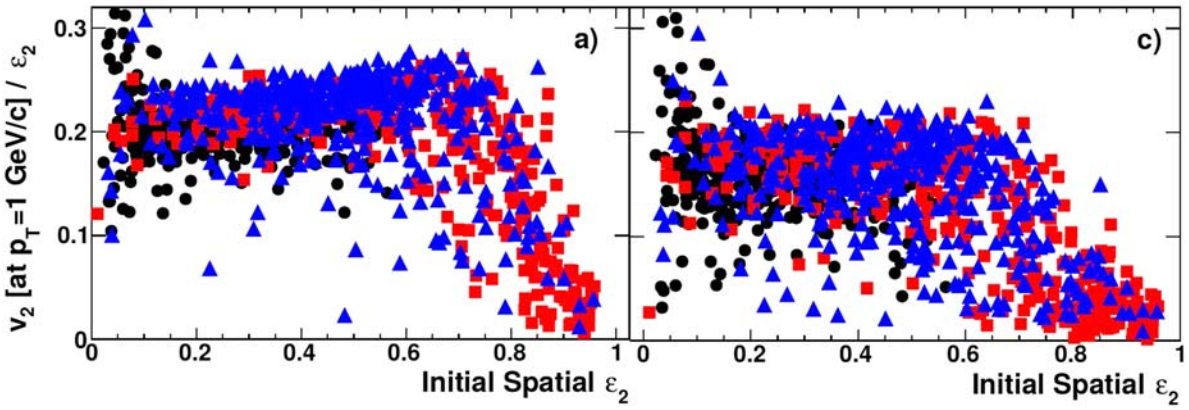

Fig. 28. (color online) Scatter plot of v_2/ε_2 at $p_{\rm T}=1$ GeV from Glauber+SONIC hydro simulations with respect to p+Au (black symbols), d+Au (red symbols) and He^3+Au (blue symbols) collisions. Different freeze-out temperatures, $T_{fo}=150$ MeV (left panel) and $T_{fo}=170$ MeV (right panel), are applied to control the life-time of hydro evolution of the medium collective expansion. Reprinted figure with permission from J. L. Nagle et al, Phys. Rev. Lett. 113, 112301, 2014 (DOI: https://doi.org/10.1103/PhysRevLett.113.112301) (Ref. [130]). Copyright 2014 by the American Physical Society.

system collective expansion, with predictions capturing a wide spectrum of the observed flow harmonics. The success of the flow paradigm based on hydrodynamics raises a question : what is the limit of applying fluid dynamics in heavy-ion collisions? Or alternatively, what is the smallest droplet of fluid system generated in heavy-ion collisions?

Although it is natural to implement viscous hydrodynamics for the description of medium collective expansion in the flow paradigm, the picture of medium response relies on the dominance of hydrodynamic modes, over non-hydro modes from many origins. The applicability condition of hydrodynamics must be satisfied to ensure hydro mode evolution. There are two crucial issues one needs to take into account regarding the applicability of viscous hydrodynamics in heavy-ion collisions: 1) the thermalization of the created quark-gluon system; and 2) the validity of truncation of the gradient expansion in viscous hydrodynamics.

4.2.1 Thermalization of QGP

Thermalization is a necessary condition for viscous hydrodynamics, so that hydro variables are well-defined in theory. However, to realize a thermalized medium in heavy-ion collisions in a short time scale is challenging for the weakly-coupled QCD dynamics, even in large colliding systems (cf Ref. [28] for a recent review). In particular, considering the required starting time for hydro modelings determined by phenomenological analyses, namely, the required thermalization time, being around $O(1)$ fm/c, perturbative QCD gives a much longer estimate of time scale $\tau\gtrsim 1.5\alpha_s^{-13/5}Q_s^{-1}$ [140][1)].

Using the condition of the onset of hydrodynamics rather than local thermal equilibrium, the discrepancy in the time scale of thermalization can be partly remedied. The onset of hydrodynamics, sometime known as *hydrodynamization*, refers to a state of the medium at which a system starts to evolve hydrodynamically. By solving kinetic theory for a weakly-coupled medium, for the pre-equilibrium evolution in heavy-ion experiments, it is indeed confirmed that *hydrodynamization* does not require local thermal equilibrium [141], with deviations from thermal equilibrium correspond to viscous corrections [142]. Actually, in the result of the Boltzmann equation, *hydrodynamization* is achieved earlier than isotropization [143], at which the longitudinal pressure $\mathcal{P}_L$ and transverse pressure $\mathcal{P}_{\rm T}$,

$$\mathcal{P}_L=\int\frac{{\rm d}^3p}{(2\pi)^3p^0}p_z^2f(t,\vec{x},\vec{p}),$$
$$\mathcal{P}_{\rm T}=\int\frac{{\rm d}^3p}{2(2\pi)^3p^0}(p_x^2+p_y^2)f(t,\vec{x},\vec{p}), \quad (93)$$

become comparable. The condition of $\mathcal{P}_L\approx\mathcal{P}_{\rm T}$ is known as *isotropization*. In Eq. (93), $f(t,\vec{x},\vec{p})$ is the phase space distribution of the out-of-equilibrium system. One may check that, for the Bjorken flow, the pressure difference is related to viscous corrections in hydrodynamics,

$$\mathcal{P}_L-\mathcal{P}_{\rm T}=-2\eta/\tau+O(1/\tau^2), \quad (94)$$

which gives an explicit example showing the relation between viscous corrections in hydrodynamics and effects of out-of-equilibrium dynamics. For strongly coupled systems, numerical simulations have been developed to mimic colliding systems of different system sizes, based

1) Even with the strong coupling constant taken at a relatively large value, $\alpha_s\sim 0.3$, the saturation scale Q_s expected in nucleus-nucleus collisions cannot result in a thermalization time scale comparable to $O(1)$ fm/c. The expected time scale from perturbative QCD is even longer in small systems, as Q_s is smaller.

on gauge/gravity duality techniques (cf. Ref. [144, 145]). A short time scale of *hydrodynamization* that is comparable to the estimate in the flow paradigm is realized.

Despite the progress made in the analyses of thermalization or the onset of hydrodynamics, by solving out-of-equilibrium dynamical evolutions, an alternative is to amend the hydrodynamic framework to include out-of-equilibrium effects. Such a strategy leads to the development of anisotropic hydrodynamics (ahydro) [147, 148].

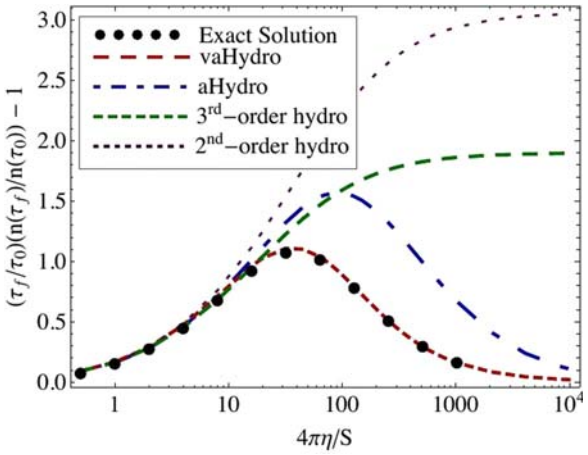

Fig. 29. (color online) Convergence of ahydro and vahydro in comparison with the exact solution of Boltzmann equation with relaxation time approximation. The parameter η/s can be understood as a quantity controlling deviations of the system from local thermal equilibrium. Reprinted figure with permission from D. Bazow, U. Heinz, and M. Strickland, Phys. Rev. C 90, 054910, 2014 (DOI: https://doi.org/10.1103/PhysRevC.90.054910) (Ref. [146]). Copyright 2014 by the American Physical Society.

In anisotropic hydrodynamics, following the standard derivation of hydrodynamics from kinetic theory, the gradient expansion is made on top of an anisotropic background. For instance, for a system with Bjorken boost invariance, the Romatschke-Strickland distribution function [149] can be used to effectively describe an anisotropic background,

$$f(t,\vec{x},\vec{p})=f_{\rm iso}\left(\sqrt{\vec{p}^2+\xi(\tau)p_z^2}/\Lambda(\tau)\right), \tag{95}$$

with ξ characterizing momentum anisotropy, and $\Lambda(\tau)$ the energy scale. By doing so, out-of-equilibrium effects of the system are to some extent absorbed into the anisotropic background. Similar gradient expansion including higher viscous corrections can be applied iteratively, leading to the viscous version of anisotropic hydrodynamics (vahydro) [146]. Therefore, one expects improvements in the solution of out-of-equilibrium evolution, compared to the traditionally derived viscous hydrodynamics. This is demonstrated in Fig. 29, where the produced entropy density of a Bjorken boost invariant system is calculated in viscous hydrodynamics, ahydro, vahydro and the corresponding Boltzmann equation with relaxation time approximation. The relaxation time, which characterizes how fast the system relaxes towards equilibrium, is taken inversely proportional to the local temperature, $\tau_{rel}\propto\eta/sT$. As a result, η/s effectively controls the deviations of the system from local equilibrium. Ahydro and vahydro do have a better convergence behavior towards the exact solution from the Boltzmann equation, even though the system is sufficiently far from local thermal equilibrium, with $\eta/s\sim10^4$. One may refer to Ref. [150] for a detailed review of ahydro.

4.2.2 Gradient expansion in viscous hydrodynamics

Although ahydro (or vahydro) extends the framework of hydrodynamics to out-of-equilibrium systems, which accordingly helps to relieve the tension between out-of-equilibrium system evolution and the flow paradigm, it does not conceptually provide an answer to the question raised in this section. Especially, the present success of the flow paradigm relies on the application of second order viscous hydrodynamics, as a truncated gradient expansion at the second order with respect to an isotropic background.

In the canonical formulation of viscous hydrodynamics, the gradient expansion corresponds to viscous corrections to the system evolution order-by-order. It requires a convergence condition of the gradient expansion, so that viscous hydrodynamics can be applied to a system in when higher order viscous corrections are subdominant. For the practical formulation of hydrodynamics, truncation of the gradient expansion is commonly taken at second order to avoid acausal mode evolution. For a relativistic fluid, the convergence condition of the gradient expansion is reflected by the smallness of the Knudsen number Kn, (recall the definition of the Knudsen number as a ratio between a microscopic scale, e.g., mean-free path $l_{\rm mft}$, and a macroscopic scale, e.g., system size L, Kn$\sim l_{\rm mft}/L$). As a result, when the system size gets smaller and smaller, as in the cases of small colliding systems in heavy-ion collisions, the convergence of gradient expansion is more likely to be violated. It is indeed found in realistic hydro simulations, that the Knudsen number in small colliding systems is larger than that in nucleus-nucleus collisions [18].

A large Knudsen number in small colliding systems implies the significance of higher order terms in the gradient expansion or higher order viscous corrections, in the application of hydrodynamics. Besides, one also notices that the inclusion of higher order viscous corrections extends the applicability of hydrodynamics in an out-of-equilibrium system, owing to the correspondence between effects of out-of-equilibrium dynamics and viscous corrections. However, to include higher order viscous

corrections in a theoretical framework of hydrodynamics is complicated, due to fact that the gradient expansion leading to viscous hydrodynamics is asymptotic (zero radius of convergence) rather than convergent [151].

The divergence of the gradient expansion was recently explored in the context of Bjorken flow [152, 153], where analysis is simplified as a consequence of symmetry conditions. For instance, the expansion rate of the Bjorken flow is solely determined by the proper time, $\nabla\cdot u=1/\tau$. Accordingly the measure of out-of-equilibrium can be chosen to be the dimensionless quantity,

$$w=\tau T. \tag{96}$$

so that the gradient expansion of hydrodynamic variables in hydrodynamics is written in terms of $1/w$. One may check that in the Bjorken flow, the Knudsen number $\mathrm{Kn}\sim 1/w$. In particular, the function $f(w)\equiv\tau\partial_\tau \ln w = 1+\frac{\tau}{4}\partial_\tau \ln\epsilon$, that characterizes the decay rate of the local energy density in a system experiencing Bjorken expansion, is expanded as [154]

$$f(w)=\sum_n f_n w^{-n}. \tag{97}$$

For the function $f(w)$, it is clear that the gradient expansion is divergent, since the constant coefficients f_n exhibits a facotrial growth at large n. Nevertheless, the expansion is Borel resummable. To do so, the first step is to take a Borel transformation, leading to the Borel transform of $f(w)$,

$$f_B(\xi)=\sum_n \frac{f_n}{n!}\xi^n. \tag{98}$$

An analytical continuation should be applied to $f_B(\xi)\to \tilde{f}_B(\xi)$ to help locate the singularities of the function, before the inverse Borel transformation giving rise to the resum of a generalized gradient expansion,

$$f_R(w)=w\int_C \mathrm{d}\xi \mathrm{e}^{-w\xi}\tilde{f}_B(\xi). \tag{99}$$

The integration follows a contour C between the origin and infinity on the complex plane of ξ. Corresponding to the fluid dynamics derived using gauge-fluid duality, a set of singular poles can be identified [155]. In addition to the part that is analytic, the singular poles result in exponential decay modes in the inverse transform f_R. The lowest order one is

$$\delta f_R\sim w^{-\gamma}\mathrm{e}^{-w\xi_0}, \tag{100}$$

where γ and ξ_0 are constant obtained with respect to the singularities of $\tilde{f}_B(\xi)$.

In total, the resummation procedure for $f(w)$ leads to a trans-series consisting of polynomials of $1/w$ and the exponential decay parts, instead of the normal gradient expansion. The physical interpretation of the trans-series is to identify the polynomial of $1/w$ as the corresponding resummation of hydro modes, while non-hydro modes are recognized as short-lived decay modes [155]. With respect to the fluid dynamics derived from gauge-gravity duality, non-hydro modes are found to coincide with quasi-normal modes in gravitational fluctuations [155, 156]. The appearance of the exponential decay parts in the Borel resummation is contour dependent, but there exists an unambiguous and physically sensible result in the trans-series. It is a resumed result where the exponential decay parts cancel consistently, which, as will become clear later, corresponds to the hydrodynamic attractor solution, a property related to the theory of *resurgence* in quantum theories (cf. Ref. [157–160]).

The above analysis employs only the formal behavior of the gradient expansion of the hydro function $f(w)$. The obtained structure can be validated in practical hydro calculations. For instance, the Muller-Israel-Stewart (MIS) hydrodynamics has the following equations of motion regarding Bjorken flow,

$$\begin{aligned}\tau\partial\epsilon&=-\frac{4}{3}\epsilon+\Phi,\\ \tau_\pi\partial\Phi&=\frac{4\eta}{3\tau}-\frac{4\tau_\pi\Phi}{3\tau}-\frac{\lambda_1\Phi^2}{2\eta}-\Phi,\end{aligned} \tag{101}$$

where $\Phi=-\pi^\xi_\xi$, and τ_π, λ are second order transport coefficients. The MIS hydro equations can be written as a nonlinear differential equation in terms of $f(w)$, with solutions obtained accordingly.

In Fig. 30, the numerical solutions to MIS hydro, with respect to various initial conditions, are displayed in thin blue lines. As time evolves (w increases), the hydro solutions tend to collapse towards an attractor solution. The attractor solution associated with the nonlinear differential equation can be identified numerically, or analytically through the slow-roll approximation. The attractor solution is numerically solved and shown as the magenta line in Fig. 30. Starting from different initial conditions, one indeed observe a trend of exponential decay from the random hydro solutions towards the hydro attractor. Actually, one can even determine that to the linearized order, the decay mode of the MIS hydrodynamics is consistent with that expected in the generalized Borel resummation, Eq. (100). Note that a large w indicates the system is close to local thermal equilibrium, which explains the agreements of the numerical solution with the analytical expectations from first and second order viscous hydro, in Fig. 30.

Figure 30 is a good demonstration of the existence of the hydro attractor, and the non-hydro mode decay. The hydro attractor effectively extends the description of hydrodynamics for out-of-equilibrium systems, regarding the small w region in Fig. 30. Note that at the initial state $\tau_0 = 0.5$ fm/c in the Au+Au collisions at RHIC, w can be as small as 0.5. For a system evolution even

out-of-equilibrium, the hydro attractor captures contributions from the summed hydro modes, while non-hydro modes are short-lived, and decay exponentially towards the hydro attractor. The existence of attractor solutions can be used to explain why (second order viscous) hydrodynamics provides such a remarkable description in heavy-ion collisions, from large to small colliding systems, despite the apparent challenges from thermalization and out-of-equilibrium influences.

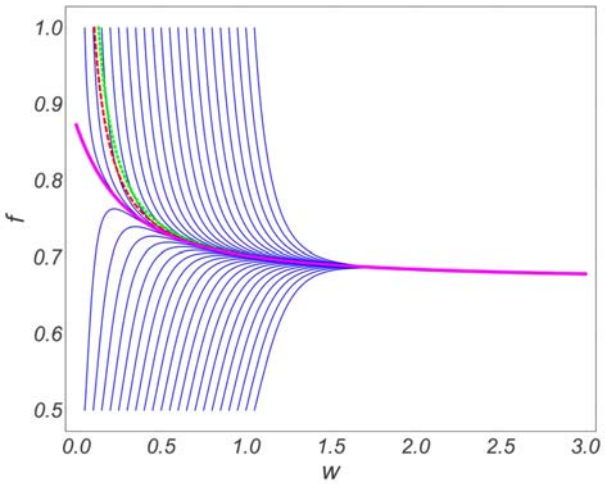

Fig. 30. (color online) Solutions of MIS hydro in the Bjorken expansion, with respect to various initial conditions (blue lines). The thick magenta line is the numerically determined hydro attractor. Hydro expectations from first and second viscous hydro are shown as the red dashed and green dotted lines. Reprinted figure with permission from M. P. Heller and M. Spaliński, Phys. Rev. Lett. 115, 072501, 2015 (DOI: https://doi.org/10.1103/PhysRevLett.115.072501) (Ref. [154]). Copyright 2015 by the American Physical Society.

The existence of hydro attractors appears promising regarding the extension of hydro modeling in heavy-ion collisions, and hence for a generalized application of the flow paradigm, to an out-of-equilibrium system. It offers a possible answer to the questions raised at the beginning of this section, that the application of hydrodynamics is extended to cases when hydrodynamic attractor solution dominates. Nonetheless, so far, the analyses of out-of-equilibrium system evolution, and the incorporation of hydrodynamics in the out-of-equilibrium system with an attractor solution are carried out in the context of Bjorken expansion with respect to conformal symmetry [161, 162]. Realistic systems in heavy-ion collisions are more complicated with much weaker symmetry constraints [163], especially in the case of QCD dynamics, in which the role of hydrodynamic attractors has not yet been clarified.

5 Summary

Based on the success of hydro modelings of heavy-ion collisions, the flow paradigm is established to analyze the observed of harmonic flow V_n. In the flow paradigm, various properties of the harmonic flow can be interpreted as a consequence of the medium collective expansion regarding the initial state geometrical information.

Although the flow paradigm relies heavily on a hydro description of the medium collective expansion, it captures the conceptual ideas of medium collective evolution. Especially, the physics picture constructed in the flow paradigm helps to reduce the influence of effective parameterizations in model simulations. In the flow paradigm, fluid dynamics is often employed to take into account the effect of medium collective expansion, and particularly fluid dynamics captures the hydro mode mode evolution associated with the decomposed modes according to the azimuthal symmetry. The decomposed modes in harmonics, with respect to the initial state geometrical fluctuations, are characterized as the initial state eccentricities $\mathcal{E}_n$'s. These eccentricities $\mathcal{E}_n$'s are responsible for the observed anisotropic momentum spectrum in experiments, and hence the harmonic flow, upon medium response relations. These response relations (Eqs. (31)) proposed in the flow paradigm, have been examined to a quantitative level, in event-by-event hydrodynamic simulations. Some of the experimentally measured signatures, such as the factorization relations among different types of symmetric cumulants, and the relative scales of the measured nonlinear medium response coefficients χ's, are found to be consistent within the medium response framework to a quantitative level.

In the flow paradigm, given these medium response relations, one is allowed to disentangle the physics information of initial state fluctuations, from the dynamics of medium evolution, from the measured flow harmonics. This is of great significance because it provides potentially model-independent analyses in heavy-ion collisions, with emphases laid directly on the properties of the initial state and medium transport. We have presented in this review, as an example, that the event-by-event fluctuations of elliptic flow v_2 reveal the fluctuation behavior of initial ellipticity ε_2. Through the fit of the probability distribution function via an elliptic-power function, the linear medium response coefficient κ_2 is approachable, together with the parameters associatd with initial state. In addition to the flow fluctuations, another way of extracting the medium dynamical properties comes from the analyses of flow correlations. This is again, a model-independent procedure. In the flow correlations involving higher order harmonics, proper cancellations in the ratio of different types of the harmonic flow lead to the measurements of medium response coefficients, χ's.

Although the flow paradigm is mostly established in high energy nucleus-nucleus collisions, its generalization to small colliding systems appears straightforward. In the recent experiments involving small colliding systems, the scenario of medium collective expansion gets support from the similar results of long-range multi-particle correlations. Quantitatively, these correlations are compatible with hydrodynamics in terms of the predicted harmonic flow, of various types. For instance, the elliptic and triangular flow from two-particle correlations in He^3Au, dAu and even proton+proton, can be well reproduced by viscous hydrodynamics. In particular, the fluctuations of v_2 in proton-lead collisions, which exhibit a consistent pattern with the power distribution function, have not only been used as the most convincing evidence of the medium collective expansion, but also provide information of the fluctuating initial state.

The success of the flow paradigm depends on the applications of viscous hydrodynamics in the quark-gluon systems created in heavy-ion collisions. However, the application hydrodynamics in small colliding systems, where one requires the thermalization of quarks and gluons to be approached in an extremely short time scale, is questionable. It then motivates the extension of the flow paradigm, or to say, the extension of the theoretical framework of viscous hydrodynamics, to systems which are out of local thermal equilibrium. In addition to the theoretical studies of the thermalization process in weakly-coupled or strongly-coupled systems, one promising progress is the discovery of hydrodynamic attractors, although the present investigations of hydrodynamic attractors are mostly limited to cases with stong symmetry conditions.

The author is grateful to Jean-Yves Ollitrault for carefully reading the manuscript and very valuable comments.

References

1 Edward Shuryak, Prog. Part. Nucl. Phys., **62**: 48–101 (2009)
2 Edward Shuryak, Rev. Mod. Phys., **89**: 035001 (2017)
3 Misha A. Stephanov, K. Rajagopal, and Edward V. Shuryak, Phys. Rev. Lett., **81**: 4816–4819 (1998)
4 P. Kovtun, Dan T. Son, and Andrei O. Starinets, Phys. Rev. Lett., **94**: 111601 (2005)
5 Miklos Gyulassy, Ivan Vitev, Xin-Nian Wang, and Ben-Wei Zhang, *Jet quenching and radiative energy loss in dense nuclear matter*, 2003
6 R. Rapp, D. Blaschke, and P. Crochet, Prog. Part. Nucl. Phys., **65**: 209–266 (2010)
7 Thomas Peitzmann and Markus H. Thoma, Phys. Rept., **364**: 175–246 (2002)
8 Jean-Franois Paquet, Chun Shen, Gabriel S. Denicol, Matthew Luzum, Bjrn Schenke, Sangyong Jeon, and Charles Gale, Phys. Rev. C, **93**(4): 044906 (2016)
9 Dmitri E. Kharzeev, Larry D. McLerran, and Harmen J. Warringa, Nucl. Phys. A, **803**: 227–253 (2008)
10 H. Niemi, K. J. Eskola, R. Paatelainen, and K. Tuominen, Phys. Rev. C, **93**(1): 014912 (2016)
11 Ekaterina Retinskaya, Matthew Luzum, and Jean-Yves Ollitrault, Phys. Rev. C, **89**(1): 014902 (2014)
12 J. Scott Moreland and Ron A. Soltz, Phys. Rev. C, **93**(4): 044913 (2016)
13 Akihiko Monnai and Jean-Yves Ollitrault, Phys. Rev. C, **96**(4): 044902 (2017)
14 Pasi Huovinen and Pter Petreczky, Nucl. Phys. A, **837**: 26–53 (2010)
15 Paul Romatschke, Int. J. Mod. Phys. E, **19**: 1–53 (2010)
16 Rudolf Baier, Paul Romatschke, Dam Thanh Son, Andrei O. Starinets, and Mikhail A. Stephanov, JHEP, **04**: 100 (2008)
17 G. S. Denicol, H. Niemi, E. Molnar, and D. H. Rischke, Phys. Rev. D, **85**: 114047 (2012); Phys. Rev. D, **91**(3): 039902 (2015)
18 H. Niemi and G. S. Denicol, *How large is the Knudsen number reached in fluid dynamical simulations of ultrarelativistic heavy ion collisions?*, 2014
19 Scott McDonald, Chun Shen, Francois Fillion-Gourdeau, Sangyong Jeon, and Charles Gale, Phys. Rev. C, **95**(6): 064913 (2017)
20 Jing Qian, Ulrich W. Heinz, and Jia Liu, Phys. Rev. C, **93**(6): 064901 (2016)
21 Jacquelyn Noronha-Hostler, Li Yan, Fernando G. Gardim, and Jean-Yves Ollitrault, Phys. Rev. C, **93**(1): 014909 (2016)
22 Chandrodoy Chattopadhyay, Rajeev S. Bhalerao, Jean-Yves Ollitrault, and Subrata Pal, *Effects of initial-state dynamics on collective flow within a coupled transport and viscous hydrodynamic approach*, 2017
23 D. Landau and E. Lifshitz, Statistical Physics Part 2, volume 6 of Course of Theoretical Physics, Pergamon Press, 2 edition, 1987
24 Azumi Sakai, Koichi Murase, and Tetsufumi Hirano, Nucl. Phys. A, **967**: 445–448 (2017)
25 C. Young, J. I. Kapusta, C. Gale, S. Jeon, and B. Schenke, Phys. Rev. C, **91**(4): 044901 (2015)
26 Li Yan and Hanna Grnqvist, JHEP, **03**: 121 (2016)
27 J. I. Kapusta, B. Muller, and M. Stephanov, Phys. Rev. C, **85**: 054906 (2012)
28 Kenji Fukushima, Rept. Prog. Phys., **80**(2): 022301 (2017)
29 Wojciech Florkowski, Michal P. Heller, and Michal Spalinski, *New theories of relativistic hydrodynamics in the LHC era*, 2017
30 M. Habich, G. A. Miller, P. Romatschke, and W. Xiang, Eur. Phys. J. C, **76**(7): 408 (2016)
31 Bjoern Schenke, Prithwish Tribedy, and Raju Venugopalan, Phys. Rev. Lett., **108**: 252301 (2012)
32 B. Alver, M. Baker, C. Loizides, and P. Steinberg, The PHOBOS Glauber Monte Carlo, 2008
33 Dmitri Kharzeev, Eugene Levin, and Marzia Nardi, Nucl. Phys. A, **747**: 609–629 (2005)
34 J. Scott Moreland, Jonah E. Bernhard, and Steffen A. Bass, Phys. Rev. C, **92**(1): 011901 (2015)
35 H. Niemi, K. J. Eskola, and R. Paatelainen, Phys. Rev. C, **93**(2): 024907 (2016)
36 Fred Cooper and Graham Frye, Phys. Rev. D, **10**: 186 (1974)
37 Derek Teaney, Phys. Rev. C, **68**: 034913 (2003)
38 Akihiko Monnai and Tetsufumi Hirano, Phys. Rev. C, **80**: 054906 (2009)
39 Piotr Bozek, Phys. Rev. C, **81**: 034909 (2010)
40 Derek Teaney and Li Yan, Phys. Rev. C, **89**(1): 014901 (2014)
41 S. A. Bass et al, Prog. Part. Nucl. Phys., **41**: 255–369 (1998)

42 Jean-Yves Ollitrault, Phys. Rev. D, **46**: 229–245 (1992)
43 Derek Teaney and Li Yan, Phys. Rev. C, **83**: 064904 (2011)
44 Ekaterina Retinskaya, Matthew Luzum, and Jean-Yves Ollitrault, Phys. Rev. Lett., **108**: 252302 (2012)
45 Nicolas Borghini, Phys. Rev. C, **75**: 021904 (2007)
46 B. Alver and G. Roland, Phys. Rev. C, **81**: 054905 (2010); Phys. Rev. C, **82**: 039903 (2010)
47 Steven S. Gubser and Amos Yarom, Nucl. Phys. B, **846**: 469–511 (2011)
48 K. M. O'Hara, S. L. Hemmer, M. E. Gehm, S. R. Granade, and J. E. Thomas, Science, **298**: 2179–2182 (2002)
49 Huichao Song and Ulrich W. Heinz, Phys. Rev. C, **78**: 024902 (2008)
50 Stefan Floerchinger and Urs Achim Wiedemann, JHEP, **08**: 005 (2014)
51 Stefan Floerchinger and Urs Achim Wiedemann, Phys. Lett. B, **728**: 407–411 (2014)
52 Rajeev S. Bhalerao, Jean-Yves Ollitrault, Subrata Pal, and Derek Teaney, Phys. Rev. Lett., **114**(15): 152301 (2015)
53 Aleksas Mazeliauskas and Derek Teaney, Phys. Rev. C, **91**(4): 044902 (2015)
54 Li Yan and Jean-Yves Ollitrault, Phys. Rev. Lett., **112**: 082301 (2014)
55 Li Yan, Jean-Yves Ollitrault, and Arthur M. Poskanzer, Phys. Rev. C, **90**(2): 024903 (2014)
56 Sergei A. Voloshin, Arthur M. Poskanzer, Aihong Tang, and Gang Wang, Phys. Lett. B, **659**: 537–541 (2008)
57 Jean-Paul Blaizot, Wojciech Broniowski, and Jean-Yves Ollitrault. Continuous description of fluctuating eccentricities. Phys. Lett. B, **738**: 166–171 (2014)
58 Jean-Paul Blaizot, Wojciech Broniowski, and Jean-Yves Ollitrault, Phys. Rev. C, **90**(3): 034906 (2014)
59 Hanna Grnqvist, Jean-Paul Blaizot, and Jean-Yves Ollitrault, Phys. Rev. C, **94**(3): 034905 (2016)
60 Jiangyong Jia and Derek Teaney, Eur. Phys. J. C, **73**: 2558 (2013)
61 Li Yan, Phys. Rev. C, **91**(6): 064909 (2015)
62 Rajeev S. Bhalerao, Matthew Luzum, and Jean-Yves Ollitrault, Phys. Rev. C, **84**: 054901 (2011)
63 B. Alver et al, Phys. Rev. C, **77**: 014906 (2008)
64 Rajeev S. Bhalerao, Jean-Yves Ollitrault, and Subrata Pal, Phys. Rev. C, **88**: 024909 (2013)
65 Li Yan and Jean-Yves Ollitrault, Phys. Lett. B, **744**: 82–87 (2015)
66 L. P. Kadanoff and P. C. Martin, Annals of Physics, **24**(10): 419–469 (1963)
67 H. Niemi, G. S. Denicol, H. Holopainen, and P. Huovinen, Phys. Rev. C, **87**(5): 054901 (2013)
68 J. D. Bjorken, Phys. Rev. D, **27**: 140–151 (1983)
69 Pilar Staig and Edward Shuryak, Phys. Rev. C, **84**: 044912 (2011)
70 Roy A. Lacey, D. Reynolds, A. Taranenko, N. N. Ajitanand, J. M. Alexander, Fu-Hu Liu, Yi Gu, and A. Mwai, J. Phys. G, **43**(10): 10LT01 (2016)
71 Derek Teaney and Li Yan, Phys. Rev. C, **86**: 044908 (2012)
72 Fernando G. Gardim, Frederique Grassi, Matthew Luzum, and Jean-Yves Ollitrault, Phys. Rev. C, **85**: 024908 (2012)
73 Zhi Qiu and Ulrich W. Heinz, Phys. Rev. C, **84**: 024911 (2011)
74 Jing Qian, Ulrich Heinz, Ronghua He, and Lei Huo, Phys. Rev. C, **95**(5): 054908 (2017)
75 Rajeev S. Bhalerao, Jean-Yves Ollitrault, and Subrata Pal, Phys. Lett. B, **742**: 94–98 (2015)
76 Shreyasi Acharya et al, Phys. Lett. B, **773**: 68–80 (2017)
77 Shengquan Tuo, Nucl. Phys. A, **967**: 381–384 (2017)
78 Georges Aad et al, Phys. Rev. C, **92**(3): 034903 (2015)
79 Li Yan, Subrata Pal, and Jean-Yves Ollitrault, Nucl. Phys. A, **956**: 340–343 (2016)
80 Nicolas Borghini and Jean-Yves Ollitrault, Phys. Lett. B, **642**: 227–231 (2006)
81 Dieter Forster, David R. Nelson, and Michael J. Stephen, Phys. Rev. A, **16**(8): 732–749 (1977)
82 Pavel Kovtun and Laurence G. Yaffe, Phys. Rev. D, **68**: 025007 (2003)
83 Pavel Kovtun, Guy D. Moore, and Paul Romatschke, Phys. Rev. D, **84**: 025006 (2011)
84 Yukinao Akamatsu, Aleksas Mazeliauskas, and Derek Teaney, Phys. Rev. C, **95**(1): 014909 (2017)
85 Yukinao Akamatsu, Aleksas Mazeliauskas, and Derek Teaney, *Bulk viscosity from hydrodynamic fluctuations with relativistic hydro-kinetic theory*, 2017
86 Mauricio Martinez and Thomas Schfer, *Hydrodynamic tails and a fluctuation bound on the bulk viscosity*, 2017
87 Vardan Khachatryan et al, Phys. Rev. Lett., **116**(17): 172302 (2016)
88 Serguei Chatrchyan et al, Phys. Lett. B, **724**: 213–240 (2013)
89 K. Aamodt et al, Phys. Lett. B, **708**: 249–264 (2012)
90 Fernando G. Gardim, Frederique Grassi, Matthew Luzum, and Jean-Yves Ollitrault, Phys. Rev. C, **87**(3): 031901 (2013)
91 Ulrich Heinz, Zhi Qiu, and Chun Shen, Phys. Rev. C, **87**(3): 034913 (2013)
92 Vardan Khachatryan et al, Phys. Rev. C, **92**(3): 034911 (2015)
93 Igor Kozlov, Matthew Luzum, Gabriel Denicol, Sangyong Jeon, and Charles Gale, *Transverse momentum structure of pair correlations as a signature of collective behavior in small collision systems*, 2014
94 Jaroslav Adam et al, Phys. Rev. Lett., **116**(13): 132302 (2016)
95 Nicolas Borghini, Phuong Mai Dinh, and Jean-Yves Ollitrault, Phys. Rev. C, **64**: 054901 (2001)
96 Nicolas Borghini, Phuong Mai Dinh, and Jean-Yves Ollitrault, Phys. Rev. C, **63**: 054906 (2001)
97 Georges Aad et al, JHEP, **11**: 183 (2013)
98 Giuliano Giacalone, Li Yan, Jacquelyn Noronha-Hostler, and Jean-Yves Ollitrault, Phys. Rev. C, **95**(1): 014913 (2017)
99 Betty Bezverkhny Abelev et al, Phys. Rev. C, **90**(5): 054901 (2014)
100 Georges Aad et al, Phys. Rev. C, **90**(2): 024905 (2014)
101 Jaroslav Adam et al, Phys. Rev. Lett., **117**: 182301 (2016)
102 L. Adamczyk et al, *Harmonic decomposition of three-particle azimuthal correlations at RHIC*, 2017
103 L. Adamczyk et al, *Constraining the initial conditions and temperature dependent transport with three-particle correlations in Au+Au collisions*, 2017
104 Paul Romatschke and Ulrike Romatschke, Phys. Rev. Lett., **99**: 172301 (2007)
105 Jiangyong Jia and Soumya Mohapatra, Phys. Rev. C, **88**(1): 014907 (2013)
106 James R. Castle, Nucl. Phys. A, **967**: 401–404 (2017)
107 Li Yan, Jean-Yves Ollitrault, and Arthur M. Poskanzer, Phys. Lett. B, **742**: 290–295 (2015)
108 Vardan Khachatryan et al, Phys. Rev. Lett., **115**(1): 012301 (2015)
109 Adam Bzdak, Piotr Bozek, and Larry McLerran, Nucl. Phys. A, **927**: 15–23 (2014)
110 Jiangyong Jia and Sooraj Radhakrishnan, Phys. Rev. C, **92**(2): 024911 (2015)
111 Georges Aad et al, Eur. Phys. J. C, **74**(11): 3157 (2014)
112 Giuliano Giacalone, Li Yan, Jacquelyn Noronha-Hostler, and Jean-Yves Ollitrault, J. Phys. Conf. Ser., **779**(1): 012064 (2017)
113 Matthew Luzum and Jean-Yves Ollitrault, Phys. Rev. C, **87**(4): 044907 (2013)
114 D. Teaney and L. Yan, Phys. Rev. C, **90**(2): 024902 (2014)
115 You Zhou, Nucl. Phys. A, **967**: 377–380 (2017)
116 Ante Bilandzic, Christian Holm Christensen, Kristjan Gulbrandsen, Alexander Hansen, and You Zhou, Phys. Rev. C,

89(6): 064904 (2014)
117 Giuliano Giacalone, Li Yan, Jacquelyn Noronha-Hostler, and Jean-Yves Ollitrault, Phys. Rev. C, **94**(1): 014906 (2016)
118 Serguei Chatrchyan et al, Phys. Lett. B, **718**: 795–814 (2013)
119 Albert M Sirunyan et al, *Observation of correlated azimuthal anisotropy Fourier harmonics in pp and pPb collisions at the LHC*, 2017
120 Betty Bezverkhny Abelev et al, Phys. Lett. B, **726**: 164–177 (2013)
121 Morad Aaboud et al, *Measurement of multi-particle azimuthal correlations with the subevent cumulant method in pp and p+Pb collisions with the ATLAS detector at the LHC*, 2017
122 Morad Aaboud et al, Eur. Phys. J. C, **77**(6): 428 (2017)
123 A. Adare et al, Phys. Rev. Lett., **114**(19): 192301 (2015)
124 A. Adare et al, Phys. Rev. Lett., **115**(14): 142301 (2015)
125 Vardan Khachatryan et al, Phys. Lett. B, **765**: 193–220 (2017)
126 Piotr Bozek, Phys. Rev. C, **85**: 014911 (2012)
127 Piotr Bozek and Wojciech Broniowski, Phys. Lett. B, **718**: 1557–1561 (2013)
128 Piotr Bozek and Wojciech Broniowski, Phys. Lett. B, **747**: 135–138 (2015)
129 Piotr Bozek and Wojciech Broniowski, Phys. Rev. C, **88**(1): 014903 (2013)
130 J. L. Nagle, A. Adare, S. Beckman, T. Koblesky, J. Orjuela Koop, D. McGlinchey, P. Romatschke, J. Carlson, J. E. Lynn, and M. McCumber, Phys. Rev. Lett., **113**(11): 112301 (2014)
131 Adam Bzdak, Bjoern Schenke, Prithwish Tribedy, and Raju Venugopalan, Phys. Rev. C, **87**(6): 064906 (2013)
132 Bjoern Schenke and Raju Venugopalan, Phys. Rev. Lett., **113**: 102301 (2014)
133 Adam Bzdak and Guo-Liang Ma, Phys. Rev. Lett., **113**(25): 252301 (2014)
134 Paul M. Chesler, JHEP, **03**: 146 (2016)
135 Gökçe Başar and Derek Teaney, Phys. Rev. C, **90**(5): 054903 (2014)
136 Chun Shen, Ulrich Heinz, Pasi Huovinen, and Huichao Song, Phys. Rev. C, **84**: 044903 (2011)
137 Bjoern Schenke, Soeren Schlichting, Prithwish Tribedy, and Raju Venugopalan, Phys. Rev. Lett., **117**(16): 162301 (2016)
138 Björn Schenke and Raju Venugopalan, Nucl. Phys. A, **931**: 1039–1044 (2014)
139 Paul Romatschke, Eur. Phys. J. C, **75**(7): 305 (2015)
140 R. Baier, Alfred H. Mueller, D. Schiff, and D. T. Son, Phys. Lett. B, **502**: 51–58 (2001)
141 Aleksi Kurkela and Yan Zhu, Phys. Rev. Lett., **115**(18): 182301 (2015)
142 Jean-Paul Blaizot and Li Yan, JHEP, **11**: 161 (2017)
143 Peter Brockway Arnold, Jonathan Lenaghan, Guy D. Moore, and Laurence G. Yaffe, Phys. Rev. Lett., **94**: 072302 (2005)
144 Paul M. Chesler and Laurence G. Yaffe, Phys. Rev. Lett., **102**: 211601 (2009)
145 Paul M. Chesler and Laurence G. Yaffe, JHEP, **10**: 070 (2015)
146 Dennis Bazow, Ulrich W. Heinz, and Michael Strickland, Phys. Rev. C, **90**(5): 054910 (2014)
147 Mauricio Martinez and Michael Strickland, Nucl. Phys. A, **848**: 183–197 (2010)
148 Wojciech Florkowski and Radoslaw Ryblewski, Phys. Rev. C, **83**: 034907 (2011)
149 Paul Romatschke and Michael Strickland, Phys. Rev. D, **68**: 036004 (2003)
150 Michael Strickland, Acta Phys. Polon. B, **45**(12): 2355–2394 (2014)
151 S.R. Groot, W.A. Leeuwen, and C.G. van Weert, *Relativistic kinetic theory: principles and applications*, (North-Holland Pub. Co., 1980)
152 Michal P. Heller, Aleksi Kurkela, and Michal Spalinski, *Hydrodynamization and transient modes of expanding plasma in kinetic theory*, 2016
153 Gabriel S. Denicol and Jorge Noronha, *Divergence of the Chapman-Enskog expansion in relativistic kinetic theory*, 2016
154 Michal P. Heller and Michal Spalinski, Phys. Rev. Lett., **115**(7): 072501 (2015)
155 Michal P. Heller, Romuald A. Janik, and Przemyslaw Witaszczyk, Phys. Rev. Lett., **110**(21): 211602 (2013)
156 Pavel K. Kovtun and Andrei O. Starinets, Phys. Rev. D, **72**: 086009 (2005)
157 Gerald V. Dunne and Mithat Unsal, JHEP, **11**: 170 (2012)
158 Gerald V. Dunne and Mithat Ünsal, PoS, **LATTICE2015**: 010 (2016)
159 Daniele Dorigoni, *An Introduction to Resurgence, Trans-Series and Alien Calculus*, 2014
160 Alex Buchel, Michal P. Heller, and Jorge Noronha, Phys. Rev. D, **94**(10): 106011 (2016)
161 Michael Strickland, Jorge Noronha, and Gabriel Denicol, *The anisotropic non-equilibrium hydrodynamic attractor*, 2017
162 Gabriel S. Denicol and Jorge Noronha, *Analytical attractor and the divergence of the slow-roll expansion in relativistic hydrodynamics*, 2017
163 Paul Romatschke, *Relativistic Hydrodynamic Attractors with Broken Symmetries: Non-Conformal and Non-Homogeneous*, 2017